UNIVERSIDAD TÉCNICA FEDERICO SANTA MARÍA
DEPARTMENT OF PHYSICS
VALPARAÍSO - CHILE

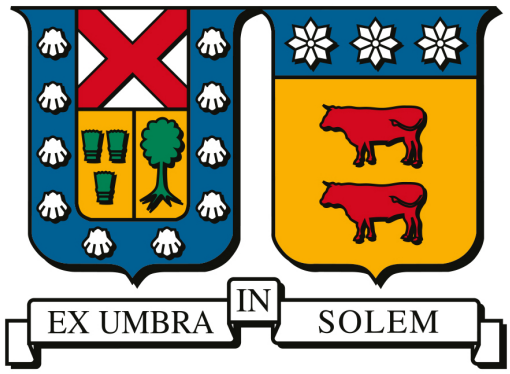

A Search for Vector-Like Lepton with Long-Lived Particles in the CMS Detector

Valentina Nicole Vega Sepúlveda

Submitted in partial satisfaction of the requirements for the Degree of
Master in Physics

Supervisor	:	Dr. William Brooks
Second Supervisor	:	Dr. Cristián Peña
Internal Evaluator	:	Dr. Sebastián Tapia
External Evaluator	:	Dr. Francisca Garay

July 2025

CONSTANCIA DE VALIDACIÓN Y CONFIDENCIALIDAD DE MONOGRAFÍA A REPOSITORIO ACADÉMICO

1.- IDENTIFICACIÓN DEL TRABAJO ACADÉMICO

Tipo de monografía (marcar una opción): ☐ Memoria o trabajo de título; ☒ Tesis de Postgrado;

Título del trabajo: A Search for Vector-Like Lepton with Long-Lived

Particles in the CMS Detector

Nombre del candidato(a): Valentina Nicole Vega Sepúlveda

Carrera / Grado: Magister en Ciencias, mención Física

Campus: Casa Central Valparaiso**;** **Departamento**: Física

2.- VALIDACIÓN DEL PROFESOR GUÍA/DIRECTOR DE TESIS

Yo, William K. Brooks, en mi calidad de profesor(a) guía/director(a) del trabajo académico mencionado anteriormente **DEJO CONSTANCIA** que:

- He revisado esta versión del documento y corresponde a la versión final aprobada del trabajo.
- El trabajo cumple con los requisitos académicos y de formato establecidos por la institución

3.- EVALUACIÓN DE CONFIDENCIALIDAD POR PROPIEDAD INDUSTRIAL

☒ El trabajo **NO contiene información que amerite confidencialidad** y puede ser publicado de inmediato en repositorio con acceso abierto.

☐ El trabajo **CONTIENE** información con potenciales implicancias de propiedad industrial o intelectual y requiere un periodo de confidencialidad (embargo) por:

☐ 6 meses; ☐ 12 meses; ☐ 2 años; ☐ 3 años; ☐ 5 años; ☐ 10 años

Fundamentación de la necesidad de confidencialidad (obligatorio si se solicita embargo):

4.- FIRMAS

Profesor(a) guía o director(a) de memoria o tesis:

Fecha: 11/08/2025 ; **Firma:** William King Brooks

Estudiante o Candidato(a):

Fecha: 11/08/2025 ; **Firma:** Valentina

Este formulario debe ser insertado como página 2 de la memoria o tesis, completado y firmado por estudiante y profesor(a) antes de la entrega en portal PRISMA de Biblioteca USM.

A mi honorable Esposo y mi conejito Brownie . . .

Por ser mi cable a tierra y creer en mí aun cuando yo lo dudaba.

Acknowledgements

Es imposible llegar al final de este camino sin detenerme a agradecer profundamente a todas las personas que han marcado mi vida con su presencia, su generosidad y su amor. Esta tesis no solo representa un logro académico, sino también un viaje emocional, humano, lleno de aprendizajes que van mucho más allá de la ciencia. A todos los que me tendieron la mano, que creyeron en mí cuando más lo necesitaba, les debo cada página escrita y cada sueño que hoy comienza a tomar forma.

A mi esposo, mi compañero de vida, mi refugio y mi fuerza. Has estado conmigo en cada paso, en cada desvelo, en cada logro y cada caída. Tu amor ha sido el pilar que sostuvo mi mente cuando flaqueaba, y tu fe en mí ha sido la voz que me impulsó a seguir aun cuando dudaba. Gracias por caminar a mi lado sin soltarme nunca.

A William Brooks, por ser mucho más que un profesor guía. Gracias por enseñarme con paciencia, por escucharme con atención, y por confiar en mis capacidades incluso cuando yo misma no lo hacía. Su apoyo ha sido como el de un padre sabio y presente, y sé que sus palabras siempre me acompañarán en el camino que queda por recorrer.

Al equipo de investigación de Fermilab, especialmente a Cristian y Christina, por abrirme las puertas de un mundo que antes parecía lejano. Me enseñaron con generosidad, me guiaron con rigor y humanidad, y me dieron la oportunidad de crecer profesional y personalmente. Gracias por confiar en mí, por retarme, por incluirme, y por darme el espacio para descubrir la científica que puedo llegar a ser.

A todas las personas del CCTVal, y en especial a Daniela, por su apoyo incondicional. Tu llegada a Fermilab no fue solo una coincidencia feliz, fue una luz que iluminó un camino lleno de incertidumbres. Gracias por tus gestiones, tu cercanía, y por ser parte fundamental de la posibilidad que me cambió la vida: realizar mi pasantía en uno de los centros más importantes del mundo. Sin ti, nada de esto habría sido posible.

Finalmente, a mis pequeños hermanos, mis adorados primos, mis amigas y amigos, a quienes desde la distancia me acompañaron con mensajes, abrazos, y silencios que dijeron más que mil palabras. Gracias por creer en mí, por sostenerme, y por hacerme sentir que nunca estuve sola.

Esta tesis es también de ustedes. Con todo mi corazón, Gracias.

Abstract

This thesis presents the development and results of a search for long-lived particles (LLPs) decaying into electromagnetic final states, motivated by a simplified model involving heavy vector-like leptons (VLLs). The analysis is based on the full Run 2 dataset recorded with the CMS detector at the CERN LHC, corresponding to an integrated luminosity of 138 fb^{-1} at $\sqrt{s} = 13$ TeV. The search targets displaced electromagnetic showers produced by LLP decays into photon pairs ($a_\tau \to \gamma\gamma$), reconstructed exclusively in the muon detectors.

To identify these events, dedicated reconstruction algorithms were developed to cluster energy deposits in the Drift Tube (DT) and Cathode Strip Chamber (CSC) systems, independent of tracking information. Backgrounds are estimated using a data-driven technique based on a parametric transfer factor derived from control regions. A comprehensive study of systematic uncertainties was carried out. The results set the first experimental constraints on this model, excluding VLL masses up to 700 GeV for proper decay lengths around 0.005–2.4 meters. These findings demonstrate the effectiveness of using the muon system to explore signatures of new physics beyond the Standard Model.

Keywords. LLP, CMS, Muon system, Displaced photons, Vector-like leptons, Long-lived particles

Contents

List of Figures

List of Tables

Part I

Introduction and Background

Chapter I: Introduction

This thesis presents a search for long-lived particles (LLPs) predicted in a simplified model that includes heavy vector-like leptons (VLLs). In this model, each VLL (τ') decays into a Standard Model tau lepton (τ) and a light pseudoscalar boson (a_τ), which subsequently decays into two photons. The pseudoscalar boson is assumed to be long-lived, potentially decaying several centimeters to meters away from the primary interaction point. Its decay produces a highly collimated photon pair that induces an electromagnetic shower when interacting with the steel yoke of the CMS muon system. These showers are reconstructed as localized clusters of hits, referred to as muon detector showers (MDS), using a dedicated clustering algorithm. This search targets events with at least one hadronically decaying tau lepton (τ_h) and at least one MDS cluster in the detector.

The Standard Model (SM) of particle physics has demonstrated outstanding success in describing the known fundamental particles and their interactions. The discovery of the Higgs boson [1, 2] has confirmed the last missing element of the SM. Nevertheless, the SM does not address several key questions, such as the nature of dark matter, the origin of neutrino masses [3], the matter-antimatter asymmetry, and the absence of gravity in the theoretical framework [4, 5]. These limitations strongly motivate the exploration of physics beyond the Standard Model (BSM).

Among various BSM extensions, vector-like fermions constitute a compelling possibility. Unlike SM fermions, which are chiral, vector-like fermions possess identical transformation properties for both left- and right-handed components under the electroweak gauge group. This property allows their inclusion without violating gauge invariance. Vector-like leptons (VLLs) are particularly interesting because they may decay into long-lived neutral bosons such as a_τ, offering novel experimental signatures at the LHC.

In the scenario studied here, VLLs are pair-produced via electroweak interactions, and each decays promptly into τa_τ, where a_τ is a CP-odd scalar arising from a complex scalar field coupled to the VLL [6]. If the pseudoscalar mass satisfies $m_{a_\tau} < 2m_\tau$, the dominant decay is $a_\tau \to \gamma\gamma$ via a one-loop process involving the heavy lepton. The boson a_τ can have a proper decay length in the range of millimeters to meters, resulting in displaced decays occurring inside the CMS muon system. The collimated photon pair produced by this decay may induce a particle shower in the muon chambers, yielding a high-multiplicity cluster of hits in the DT or CSC subsystems.

This signature is unique and unexplored: it combines a prompt tau lepton with an electromagnetic shower located several meters from the interaction point, reconstructed using MDS clustering techniques previously developed in CMS LLP searches [7, 8]. The muon system provides excellent spatial and temporal resolution, making it ideal for detecting these unconventional decays beyond the calorimeters.

The analysis is based on the full Run 2 dataset collected by CMS from 2016 to 2018, corresponding to an integrated luminosity of 138 fb^{-1}. Events are selected using missing transverse energy triggers and must contain at least one τ_h candidate and one MDS cluster. A data-driven background estimation is performed using control regions defined by inverting tau identification criteria. The signal extraction is based on a fit to the distribution of the number of reconstructed hits (N_{RecHits}) in the MDS cluster, which correlates with the energy of the decaying LLP.

The results are interpreted in the context of a simplified model where $\mathcal{B}(\tau' \to \tau a_\tau) = 100\%$ and $\mathcal{B}(a_\tau \to \gamma\gamma) = 100\%$. Upper limits at 95% confidence level are set on the VLL production cross section as a function of the VLL mass and the proper decay length of a_τ [6].

The thesis is organized as follows:

- Chapter II provides an overview of the Standard Model and the empirical observations that motivate extensions beyond it.
- Chapter III discusses theoretical frameworks predicting vector-like leptons and their decays into long-lived particles.
- Chapter IV describes the CMS detector with emphasis on its subsystems relevant for LLP searches.
- Chapter V details the analysis strategy, including event selection, background estimation, systematic uncertainties, and final results.

The main objective of this thesis is to search for long-lived pseudoscalar bosons produced in VLL decays using the full CMS Run 2 dataset. The analysis focuses on events with at least one hadronically decaying τ and one electromagnetic shower cluster reconstructed in the muon system. Backgrounds are suppressed using spatial and timing properties of the clusters, and events are categorized into CSC- and DT-cluster categories. The final results provide constraints on the production of new heavy leptons and expand the sensitivity of LLP searches beyond the reach of traditional prompt analyses.

Chapter II: The Standard Model of Particle Physics

2.1 Introduction

The Standard Model (SM) of particle physics is a quantum field theory that describes the electromagnetic, weak, and strong interactions between fundamental particles. Built on the gauge symmetry group $SU(3)_C \times SU(2)_L \times U(1)_Y$, the SM combines quantum electrodynamics (QED), the weak interaction, and quantum chromodynamics (QCD) into a unified framework.

Matter is organized into two fundamental classes of spin-1/2 fermions: **quarks** and **leptons**, each appearing in three generations. Quarks interact via all fundamental forces and are subject to color confinement due to the $SU(3)_C$ gauge symmetry. Leptons, including electrons and neutrinos, are not subject to the strong interaction.

Each fermion generation contains two quarks (one up-type and one down-type) and two leptons (a charged lepton and its corresponding neutrino). These particles are represented visually in Figure 2.1, which categorizes them by type and generation.

The weak interaction is responsible for flavor-changing processes, distinguishing fermion generations through charged current interactions mediated by the $W^{\pm}$ bosons. This structure enables phenomena such as quark flavor mixing via the CKM matrix and lepton flavor transitions observable in neutrino oscillations.

The bosons of the SM are spin-1 vector fields associated with the gauge symmetries: photons (γ), $W^{\pm}$ and Z^0 bosons for the weak interaction, and eight gluons (g) for the strong interaction. The Higgs boson, a scalar field discovered in 2012 [1, 2], is responsible for spontaneous electroweak symmetry breaking and mass generation.

The SM has achieved numerous experimental confirmations:

- Discovery of the W and Z bosons (1983, CERN) [10, 11].
- Discovery of the top quark (1995, Tevatron) [12, 13].
- Confirmation of the tau neutrino (ν_τ) (2000, DONUT experiment) [14].
- Discovery of the Higgs boson (2012, LHC) [1, 2].

These milestones reflect the robustness and predictive power of the theory. However, the SM remains incomplete: it does not incorporate neutrino masses, lacks a candidate for dark matter, does not include gravity, and suffers from the hierarchy and strong CP problems.

The dynamics of all known elementary particles and their interactions excluding gravity are governed by the Lagrangian of the Standard Model. This can be expressed schematically as:

$$\mathcal{L}_{\text{SM}} = \mathcal{L}_{\text{gauge}} + \mathcal{L}_{\text{fermion}} + \mathcal{L}_{\text{Higgs}} + \mathcal{L}_{\text{Yukawa}}. \tag{2.1}$$

Each component corresponds to a distinct part of the theory:

- $\mathcal{L}_{\text{gauge}}$: Kinetic terms for the gauge fields $G^a_{\mu\nu}$ (gluons), $W^i_{\mu\nu}$ (weak bosons), and $B_{\mu\nu}$ (hypercharge).

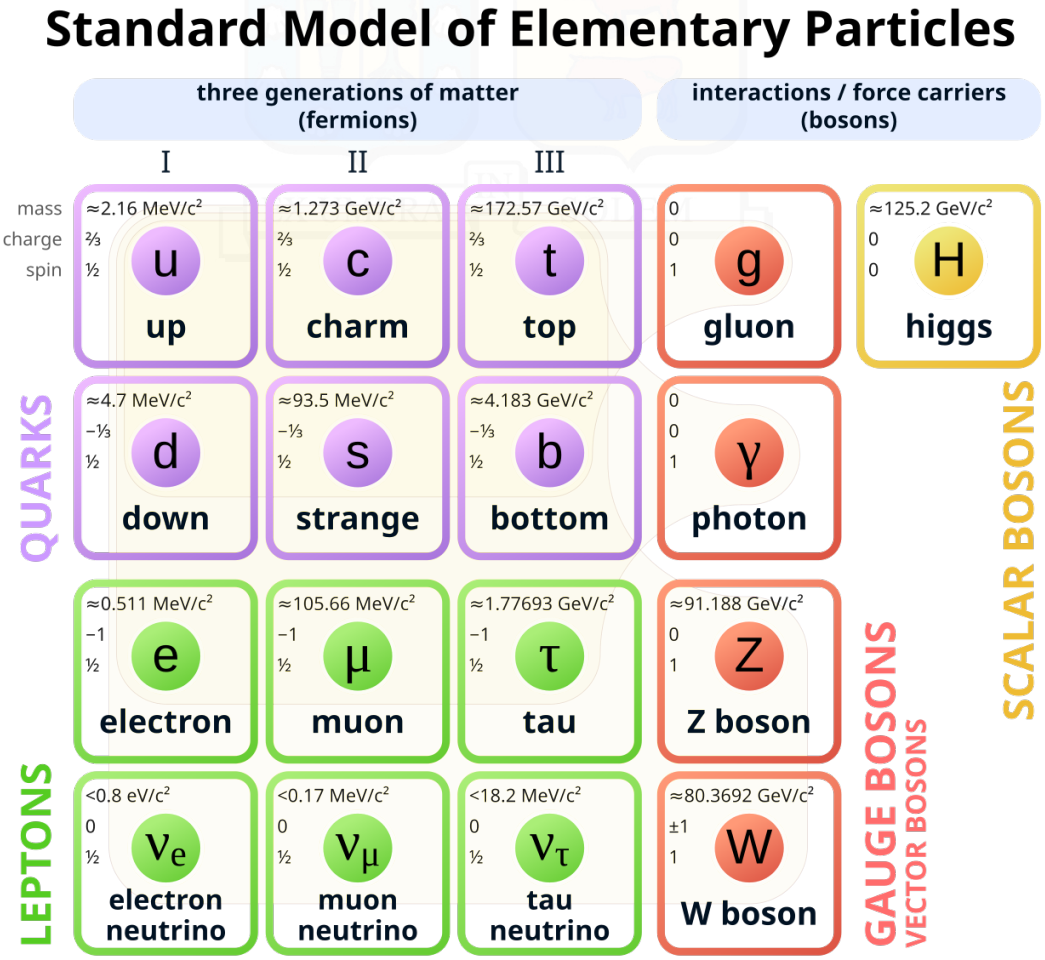

Figure 2.1: The Standard Model of elementary particles, organized into three generations of matter (quarks and leptons), gauge bosons (force carriers), and the Higgs boson [9].

- $\mathcal{L}_{\text{fermion}}$: Kinetic terms and gauge interactions for quarks and leptons.
- $\mathcal{L}_{\text{Higgs}}$: Dynamics of the scalar Higgs field and the mechanism of spontaneous symmetry breaking.
- $\mathcal{L}_{\text{Yukawa}}$: Fermion mass terms generated through Yukawa interactions with the Higgs field.

The full Lagrangian in compact form is: the SM encapsulates the dynamics of fermions, gauge fields, and the Higgs field:

$$\mathcal{L}_{\text{SM}} = -\frac{1}{4}G^a_{\mu\nu}G^{a\mu\nu} - \frac{1}{4}W^i_{\mu\nu}W^{i\mu\nu} - \frac{1}{4}B_{\mu\nu}B^{\mu\nu} + \sum_{\psi}\bar{\psi}i\gamma^\mu D_\mu\psi + |D_\mu\Phi|^2 - V(\Phi) - \sum_f y_f(\bar{\psi}_L\Phi\psi_R + \text{h.c.}). \quad (2.2)$$

Each term corresponds to a fundamental component of the theory:

- The first three terms represent the kinetic and self-interaction terms of the gauge fields:

$$G^a_{\mu\nu} = \partial_\mu G^a_\nu - \partial_\nu G^a_\mu + g_s f^{abc}G^b_\mu G^c_\nu,$$
$$W^i_{\mu\nu} = \partial_\mu W^i_\nu - \partial_\nu W^i_\mu + g\epsilon^{ijk}W^j_\mu W^k_\nu,$$
$$B_{\mu\nu} = \partial_\mu B_\nu - \partial_\nu B_\mu.$$

- The fermionic term includes the covariant derivative:

$$D_\mu = \partial_\mu - ig_s T^a G^a_\mu - ig\frac{\tau^i}{2}W^i_\mu - ig'\frac{Y}{2}B_\mu, \quad (2.3)$$

  which ensures gauge invariance under $SU(3)_C \times SU(2)_L \times U(1)_Y$.
- The term $|D_\mu\Phi|^2$ governs the kinetic behavior of the Higgs field.
- The potential $V(\Phi)$ has the form:

$$V(\Phi) = \mu^2\Phi^\dagger\Phi + \lambda(\Phi^\dagger\Phi)^2, \quad (2.4)$$

  which enables electroweak symmetry breaking when $\mu^2 < 0$.
- The final term represents Yukawa interactions, which couple left-handed and right-handed fermions to the Higgs field and generate their masses after symmetry breaking.

Each piece of this Lagrangian plays a critical role in the behavior of elementary particles, forming the basis for theoretical predictions and experimental tests of the SM.

In the following sections, we will explore the particle content and theoretical structure of the SM in greater detail, beginning with the classification of fermions and bosons.

2.2 Electroweak Symmetry Breaking

In the Standard Model, electroweak unification is described by a local gauge symmetry group $SU(2)_L \times U(1)_Y$. However, the $W^\pm$ and Z bosons are observed to be massive, which implies that this symmetry must be spontaneously broken in nature. This is achieved via the Brout-Englert-Higgs mechanism [15–17], where a complex scalar field doublet is introduced and acquires a non-zero vacuum expectation value (VEV), breaking the electroweak symmetry down to the electromagnetic $U(1)_{\text{EM}}$ subgroup.

The Lagrangian density describing the Higgs field Φ includes both a kinetic term and a potential:

$$\mathcal{L}_{\text{Higgs}} = (D_\mu\Phi)^\dagger(D^\mu\Phi) - V(\Phi), \quad (2.5)$$

with the covariant derivative defined as:

$$D_\mu = \partial_\mu - ig\frac{\tau^a}{2}W^a_\mu - ig'\frac{Y}{2}B_\mu, \quad (2.6)$$

and the Higgs potential given by the well-known "Mexican hat" form:

$$V(\Phi) = \mu^2 \Phi^\dagger \Phi + \lambda (\Phi^\dagger \Phi)^2, \tag{2.7}$$

where $\mu^2 < 0$ ensures spontaneous symmetry breaking.

Minimizing the potential, the scalar field acquires a VEV:

$$\langle \Phi \rangle = \frac{1}{\sqrt{2}} \begin{pmatrix} 0 \\ v \end{pmatrix}, \quad \text{with} \quad v = \sqrt{\frac{-\mu^2}{\lambda}}. \tag{2.8}$$

This breaks the $SU(2)_L \times U(1)_Y$ symmetry, generating masses for the weak gauge bosons. The physical mass eigenstates, the photon (A_μ) and the Z boson (Z_μ), are obtained via a rotation of the neutral gauge fields W^3_μ and B_μ:

$$\begin{pmatrix} A_\mu \\ Z_\mu \end{pmatrix} = \begin{pmatrix} \cos\theta_W & \sin\theta_W \\ -\sin\theta_W & \cos\theta_W \end{pmatrix} \begin{pmatrix} B_\mu \\ W^3_\mu \end{pmatrix} \tag{2.9}$$

where θ_W is the weak mixing angle, also known as the Weinberg angle. This mixing unifies the electromagnetic and weak interactions, relating their coupling constants g and g' to the elementary electric charge e through the relation:

$$e = g \sin\theta_W = g' \cos\theta_W. \tag{2.10}$$

The resulting masses of the gauge bosons are:

$$m_W = \frac{1}{2} v g', \tag{2.11}$$

$$m_Z = \frac{1}{2} v \sqrt{g^2 + g'^2}, \tag{2.12}$$

$$m_\gamma = 0. \tag{2.13}$$

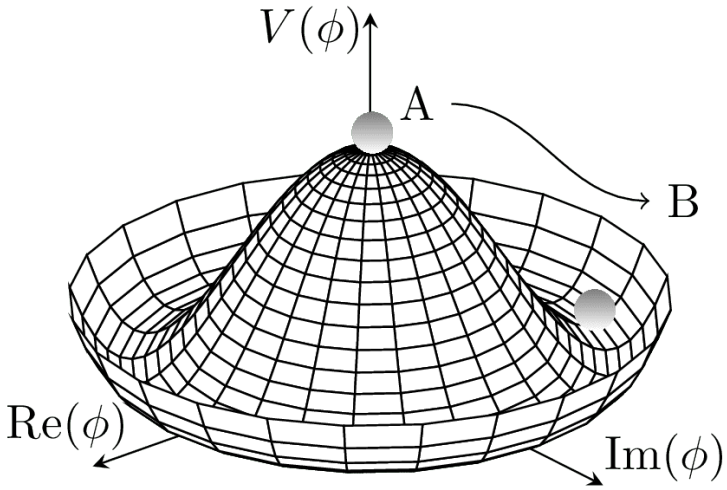

Figure 2.2: The Higgs potential [18] $V(\Phi) = \mu^2 \Phi^\dagger \Phi + \lambda (\Phi^\dagger \Phi)^2$, known as the "Mexican hat" potential. The field spontaneously chooses a vacuum expectation value $v \neq 0$ on the circle of minima.

The Yukawa interactions in the Standard Model allow fermions to acquire mass through coupling with the Higgs field. The general form is:

$$\mathcal{L}_{\text{Yukawa}} = -\sum_f y_f \bar{\psi}_L \Phi \psi_R + \text{h.c.}, \tag{2.14}$$

where y_f denotes the Yukawa coupling of fermion f.

Expanding for each generation and fermion type:

$$\mathcal{L}_{\text{Yukawa}} = -y_e \bar{L}_e \Phi e_R - y_\mu \bar{L}_\mu \Phi \mu_R - y_\tau \bar{L}_\tau \Phi \tau_R - y_d \bar{Q}_L \Phi d_R - y_u \bar{Q}_L \tilde{\Phi} u_R + \text{h.c.}, \tag{2.15}$$

where L and Q represent the lepton and quark $SU(2)_L$ doublets, respectively, and $\tilde{\Phi} = i\tau^2 \Phi^*$.

After electroweak symmetry breaking, this leads to mass terms:

$$m_f = \frac{y_f v}{\sqrt{2}}. \tag{2.16}$$

This spontaneous symmetry breaking mechanism elegantly solves the problem of gauge boson masses without explicitly violating gauge invariance. Moreover, it predicted the existence of a physical scalar boson, the Higgs boson, which was later discovered at the LHC in 2012 by the ATLAS and CMS collaborations [1, 2].

2.3 Limitations of the Standard Model

Despite its remarkable success in explaining a wide range of phenomena, the Standard Model (SM) of particle physics is incomplete. It leaves several fundamental questions unanswered, motivating the search for new physics beyond the SM.

- **Neutrino Masses:** In the SM, neutrinos are massless. However, the observation of neutrino oscillations has conclusively demonstrated that neutrinos have non-zero masses [19]. This implies the existence of physics beyond the SM, as neutrino masses require either Dirac or Majorana mass terms and, in either case, right-handed neutrino states or new interactions.
- **Dark Matter:** Observations of galactic rotation curves, gravitational lensing, and cosmological data from the cosmic microwave background point to the existence of non-luminous, non-baryonic dark matter. According to the Planck satellite measurements, ordinary matter described by the SM accounts for only about 5% of the total energy content of the universe, while dark matter constitutes roughly 27% [5]. The SM contains no viable candidate for this component.

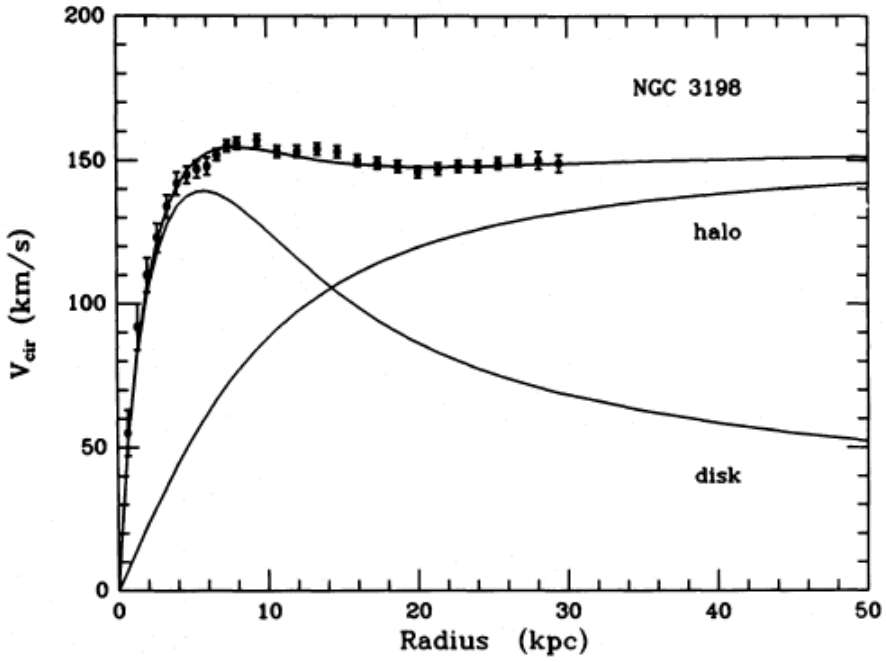

Figure 2.3: Galaxy rotation curve: the observed velocities (data points) remain approximately constant at large radii, in contrast to the expected Keplerian falloff from visible matter alone. This discrepancy points to the presence of dark matter. Adapted from [20].

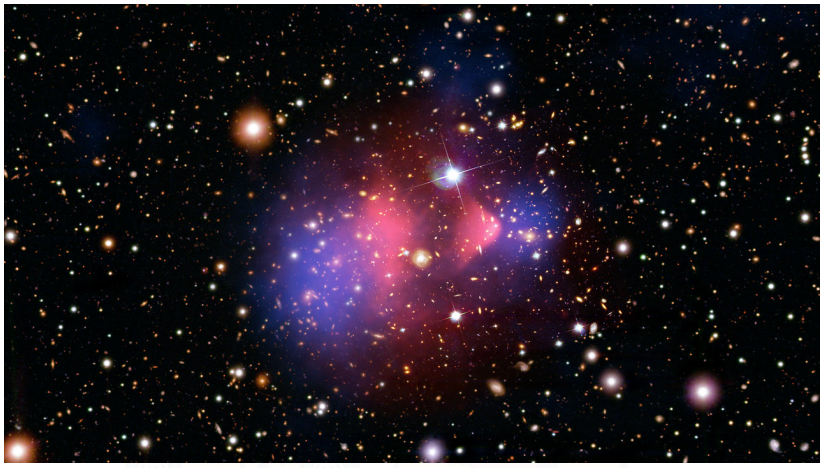

Figure 2.4: Mass map of the Bullet Cluster: X-ray emissions (pink) indicate hot baryonic gas, while gravitational lensing (blue) traces the total mass. Their separation demonstrates the existence of collisionless dark matter. Adapted from [21].

- **Baryon Asymmetry of the Universe:** The universe contains a substantial excess of matter over antimatter. Mechanisms like electroweak baryogenesis have been proposed, but the CP violation within the SM (e.g., from the CKM matrix) is insufficient to account for the observed asymmetry [22, 23]. Additional sources of CP violation or baryon-number violating interactions may be required.
- **Hierarchy Problem:** The mass of the Higgs boson is sensitive to quantum corrections at high energies. Without fine-tuning, the Higgs mass is expected to be driven toward the ultraviolet cutoff of the theory. The absence of stabilizing mechanisms such as supersymmetry, compositeness, or new symmetries renders this issue a profound puzzle [24].
- **Strong CP Problem:** Quantum chromodynamics (QCD) allows a CP-violating term in its Lagrangian, but experimental measurements, such as the electric dipole moment of the neutron, place stringent constraints on its size. The smallness of this parameter ($\theta < 10^{-10}$) is unexplained within the SM and constitutes the strong CP problem [25].
- **Gravity:** The SM does not incorporate gravity, which is described by general relativity. A quantum theory of gravity or a unified framework remains one of the outstanding goals of theoretical physics.

These limitations strongly motivate the development of extensions to the Standard Model. In particular, theories that introduce additional fermion generations—such as vector-like leptons (VLLs)—can naturally accommodate solutions to some of these problems, including neutrino masses, dark matter portals, and electroweak baryogenesis. These extensions often predict the existence of long-lived particles (LLPs) with distinct experimental signatures, such as displaced decays or detector-shielded interactions, offering powerful handles for experimental searches at the LHC.

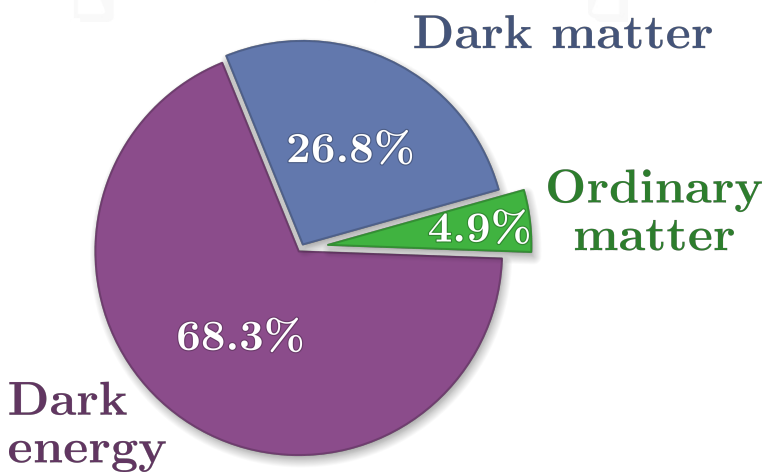

Figure 2.5: Estimated composition of the universe from Planck satellite data [5]. The Standard Model accounts only for ordinary (baryonic) matter.

Chapter III: Beyond the Standard Model and Long-Lived Particle Signatures

3.1 Motivations for Physics Beyond the Standard Model

The Standard Model (SM) has demonstrated remarkable success in describing the fundamental particles and their interactions. However, key phenomena remain unexplained, including the nature of dark matter, the origin of neutrino masses, and the matter-antimatter asymmetry. These limitations strongly suggest the existence of physics beyond the Standard Model (BSM).

These limitations, discussed in Chapter 2.1, motivate a wide variety of BSM frameworks. Many of them predict the existence of new weakly-coupled sectors or exotic fermions, including additional generations such as vector-like leptons (VLLs). The VLL scenario explored in this thesis is particularly attractive, as it provides a natural connection to dark matter through portal interactions, allows new CP-violating phases relevant for baryogenesis, and accommodates the smallness of neutrino masses via loop-level or seesaw-like mechanisms.

Two of the most compelling theoretical puzzles are the hierarchy problem and the strong CP problem.

- **The Hierarchy Problem:** The mass of the Higgs boson is subject to large quantum corrections from particles at very high energy scales, such as the Planck scale. Without an extreme fine-tuning of parameters, these corrections would naturally drive the Higgs mass to be enormous, contradicting the measured value of 125 GeV. This suggests the existence of new physics at the TeV scale, such as supersymmetry or composite Higgs models, to stabilize the Higgs mass.
- **The Strong CP Problem:** Quantum Chromodynamics (QCD) includes a term that can violate CP symmetry. However, experimental limits, particularly from the non-observation of a neutron electric dipole moment, constrain this term to be incredibly small ($\theta_{QCD} < 10^{-10}$). The reason for this smallness is not explained within the SM and points towards new physics, like the Peccei-Quinn mechanism and its associated particle, the axion.

These unresolved questions motivate a broad range of theoretical frameworks that often predict new particles, some of which could be long-lived. The most prominent examples of new fermions searched for at the LHC are Vector-Like Quarks (VLQs), Vector-Like Leptons (VLLs), and Heavy Neutral Leptons (HNLs), whose representative production diagrams are shown in Fig. 3.6.

3.2 Theoretical Landscape of Long-Lived Particles (LLPs)

The concept of Long-Lived Particles (LLPs) originates from theoretical efforts to extend the Standard Model (SM) in a way that naturally accommodates suppressed interactions or approximate symmetries. An LLP is a hypothetical particle whose proper lifetime is long enough to travel a macroscopic distance (from millimeters to kilometers) within a detector before decaying. Unlike most particles produced in high-energy collisions, which decay promptly near the interaction point, LLPs decay at displaced vertices, as schematically illustrated in Fig. 3.7.

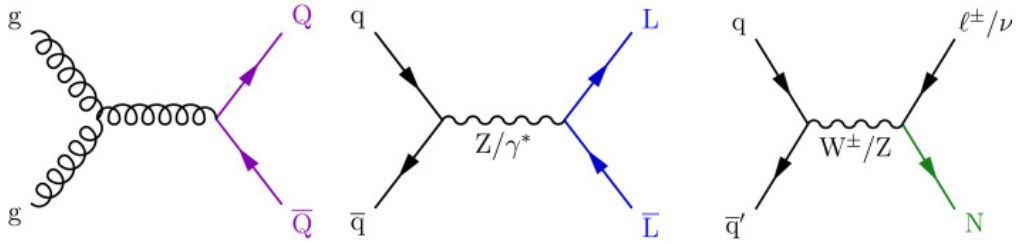

Figure 3.6: Representative Feynman diagrams showing the production of VLQs (Q, left), VLLs (L, middle), and HNLs (N, right) in proton–proton collisions. Figure adapted from the CMS Collaboration review [26].

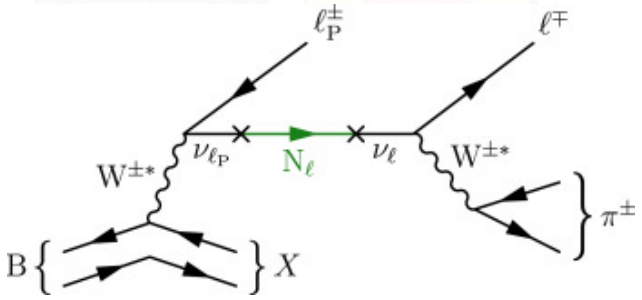

Figure 3.7: A representative diagram illustrating the concept of a displaced decay. A primary particle (here a B meson) produces a long-lived particle (N) which travels a macroscopic distance before decaying at a secondary, displaced vertex. Figure adapted from the CMS Collaboration review [26].

The lifetime (τ) of a particle is inversely proportional to its total decay width (Γ), $\tau = 1/\Gamma$. For a generic two-body decay of a particle with mass M into two particles with masses m_1 and m_2, the decay width is given by:

$$\Gamma = \frac{|\mathcal{M}|^2}{8\pi M^2} p_f \tag{3.17}$$

where $\mathcal{M}$ is the decay amplitude, which is proportional to the coupling constants of the interaction, and p_f is the momentum of the decay products in the rest frame of the parent particle. A long lifetime can thus naturally arise if:

- The couplings involved in the decay are very small (suppressing $|\mathcal{M}|^2$).
- The decay is kinematically suppressed, i.e., the mass M is very close to $m_1 + m_2$, making the available phase space (p_f) very small.

The idea was prominently featured in the context of **Hidden Valley models (2006)**, where a new sector weakly coupled to the SM could produce neutral bound states with long lifetimes [27]. Since then, the LLP framework has grown to encompass a wide range of theoretical scenarios, motivated by attempts to solve outstanding problems in particle physics.

LLPs are now predicted in a diverse set of models, each addressing different fundamental questions:

- **R-parity Violating Supersymmetry (late 1990s–2000s):** In many supersymmetric (SUSY) models, R-parity is a discrete symmetry that ensures the stability of the Lightest Supersymmetric Particle (LSP), making it a natural dark matter candidate. However, if R-parity is violated, the LSP is no longer stable and can decay into SM particles. If the R-parity-violating couplings are small, the LSP can be long-lived, leading to displaced signatures. This framework has been studied extensively as a source of LLP signals [28, 29].
- **Neutral Naturalness (2000s-2010s):** To address the hierarchy problem, theories of "neutral naturalness" propose that the partner particles responsible for stabilizing the Higgs mass are neutral under the SM's strong force. A prime example is the **Twin Higgs model (2005)**, which introduces a "twin" sector that mirrors the SM but is coupled to it only through the Higgs portal. The lightest particles in

the twin sector can be LLPs that decay back to SM particles [30]. Other variations include **Folded Supersymmetry (2015)**, which also predicts color-neutral top partners that can be long-lived [31].

- **Portal Models (2010s):** LLPs can arise as mediators to a dark sector via "portals." The **Higgs portal (2013)** allows the SM Higgs to decay into new, light scalar particles that inherit a long lifetime from the small mixing with the Higgs. Similarly, a new **vector-boson portal** can connect the SM to a dark sector via kinetic mixing with the SM hypercharge or Z boson. These models are strongly motivated by dark matter and baryogenesis scenarios and provide a generic mechanism for producing LLPs at colliders [32].

Another compelling direction involves the addition of vector-like fermions, which are non-chiral and do not spoil gauge invariance. These fermions can decay via new pseudoscalar mediators that are long-lived, leading to unique displaced signatures. In the model considered here, a charged vector-like lepton τ' decays to a SM τ and a long-lived pseudoscalar a_τ, which can subsequently decay into photons after traveling a measurable distance in the detector.

Such scenarios exemplify the broader class of long-lived particle (LLP) phenomena, whose existence would have profound implications: the presence of a new, feebly coupled sector and a unique window into physics beyond the Standard Model. Their distinct signatures—such as displaced vertices, disappearing tracks, and time-of-flight anomalies—motivate the dedicated experimental searches and reconstruction algorithms that are a central theme of this thesis.

3.3 Vector-like Fermions: Motivation and Phenomenology

Long-lived particles (LLPs) arise naturally in many BSM scenarios, especially those with weak couplings, small mass splittings, or approximate symmetries. These particles can have macroscopic lifetimes and decay at distances ranging from millimeters to several meters from the primary interaction point. Examples include neutralinos in gauge-mediated supersymmetry breaking, hidden sector mediators in dark portal models, and pseudoscalars in VLL decays. Depending on their properties, LLPs can decay into leptons, photons, or jets, producing signatures such as displaced vertices, delayed energy deposits, or detector-shielded electromagnetic showers.

Among the BSM candidates that can give rise to such LLP signatures, a particularly compelling class involves vector-like fermions.

Vector-like fermions (VLFs), which include vector-like leptons (VLLs) and vector-like quarks (VLQs), are a well-motivated extension to the SM. Unlike the chiral fermions of the SM, the left- and right-handed components of a VLF transform identically under the SM gauge group. This property allows them to have a direct, gauge-invariant mass term ($M\overline{\Psi}\Psi$) without needing the Higgs mechanism.

VLFs appear in many BSM theories, motivated by:

- Solutions to the hierarchy problem, for instance in Little Higgs or composite Higgs models.
- The cancellation of gauge anomalies in Grand Unified Theories (GUTs).
- Explanations for the mass hierarchy of SM fermions.

VLFs can mix with SM fermions through Yukawa couplings to the Higgs boson. The strength of this mixing governs their decay modes into SM particles, making them prime targets for searches at the LHC.

The phenomenology of VLFs is governed by their mass and their mixing with SM fermions. A general Lagrangian for a VLF (Ψ) interacting with an SM fermion (ψ) can be written as:

$$\mathcal{L}_{\text{VLF}} = \bar{\Psi}(i \not{D} - M_\Psi)\Psi - (y_{\text{mix}}\bar{\Psi}_L\Phi\psi_R + \text{h.c.}) \tag{3.18}$$

Here, M_Ψ is the gauge-invariant vector-like mass term. The second term describes the mixing with SM fermions via the Higgs field (Φ), where y_{mix} is the Yukawa coupling. The strength of this mixing determines the VLF's decay branching ratios into SM bosons (W, Z, H) and also governs the rate of single VLF production.

While both VLQs and VLLs are well-motivated, VLLs provide a particularly clean avenue for BSM searches at hadron colliders. Since they do not interact strongly, their production cross sections are smaller

but less overwhelmed by QCD backgrounds. Most importantly for this work, certain models predict that VLLs can decay into final states containing new, light bosons that inherit a long lifetime, thus making VLLs a prime source for LLP signatures. The search presented in this thesis focuses on precisely such a scenario.

3.4 Collider Signatures of VLL and VLQ

At the LHC, VLQs can be produced either in pairs or singly, as shown in Fig. 3.8.

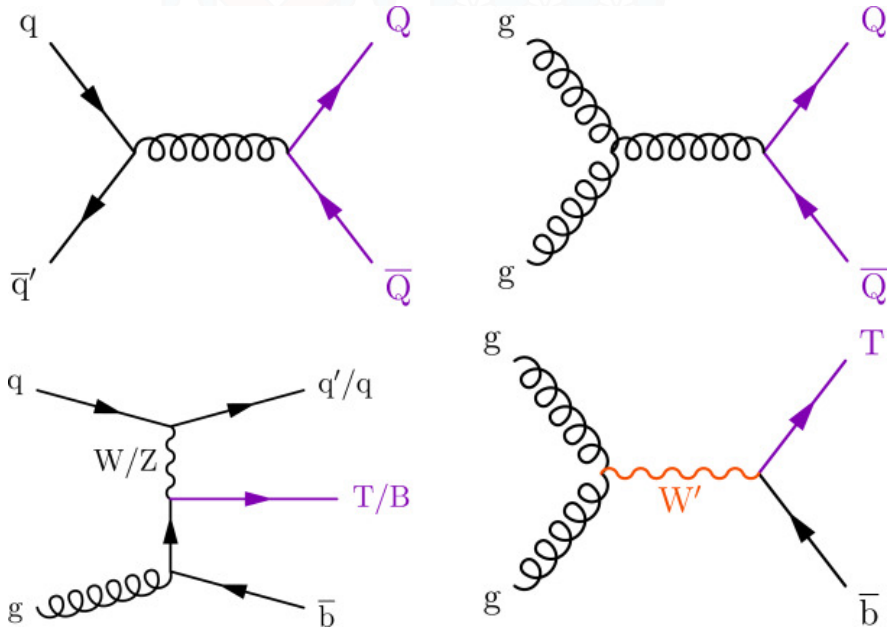

Figure 3.8: Representative LO Feynman diagrams for pair production of VLQs via the strong interaction (upper row) and single production of VLQs via EW processes (lower left) or via new interactions (lower right). Here, Q stands for either VLQ flavor. Figure adapted from the CMS Collaboration review [26].

- **Pair production** is model-independent and occurs primarily via the strong interaction for VLQs and the electroweak interaction (Drell-Yan) for VLLs.
- **Single production** is an electroweak process whose rate depends on the VLF's mixing with SM fermions.

The decay channels depend on the dominant mixing parameters and typically involve SM bosons. The main decay modes are:

- VLL $\rightarrow W\nu, Z\ell, H\ell$
- VLQ $\rightarrow Wq, Zq, Hq$

The ATLAS and CMS collaborations have performed extensive searches for VLFs, setting strong lower limits on their masses, often exceeding 1 TeV, depending on the assumed branching ratios [33, 34]. While these searches cover a wide range of final states, the analysis presented in this thesis explores a specific scenario where a VLL decays into an LLP. More generally, VLLs can lead to a rich phenomenology with final states containing multiple leptons, as exemplified in Fig. 3.9, making them powerful probes for new physics.

3.5 LLPs as Dark Matter Candidates or Mediators

LLPs play a crucial role in modern dark matter theories, particularly in scenarios beyond the standard WIMP (Weakly Interacting Massive Particle) paradigm. While WIMPs are produced via *freeze-out* from thermal equilibrium in the early universe, LLPs are often associated with the *freeze-in* mechanism.

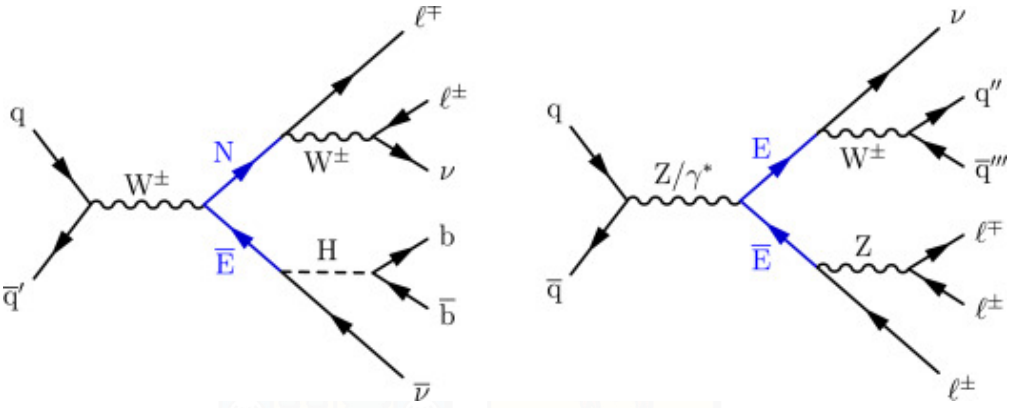

Figure 3.9: Example processes illustrating the production and decay of doublet (left) and singlet (right) VLL pairs at the LHC that result in multilepton final states. Figure adapted from the CMS Collaboration review [26].

In freeze-in scenarios, the dark matter particle interacts so feebly with the SM that it never reaches thermal equilibrium. Its relic abundance is gradually produced by the decays or annihilations of SM particles, often through a long-lived mediator particle. These LLPs are thus a generic prediction of such models.

Alternatively, LLPs themselves could be dark matter if their lifetime is longer than the age of the universe. More commonly, they act as mediators or "portals" to a secluded dark sector. For example, the Higgs boson could decay into a pair of LLPs ($h \to \text{LLP} + \text{LLP}$), which then decay back to SM particles after traveling a macroscopic distance.

More commonly, they act as mediators or "portals" to a secluded dark sector. For example, the Higgs boson could decay into a pair of LLPs ($h \to XX$), which then decay back to SM particles after traveling a macroscopic distance, as illustrated in Fig. 3.10.

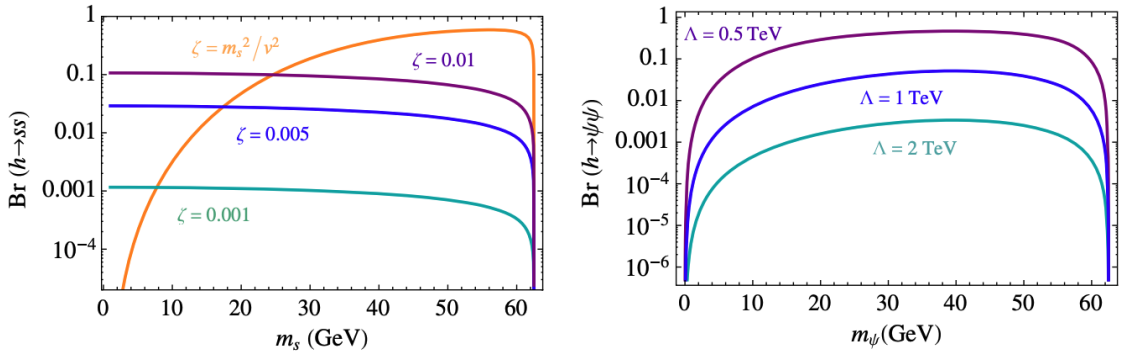

Figure 3.10: Expected exotic branching ratios of a 125 GeV Higgs boson into new weakly coupled particles. **Left:** Branching fraction $\text{Br}(h \to ss)$ for a scalar singlet s as a function of its mass m_s, assuming different values of the Higgs portal coupling ζ. **Right:** Branching fraction $\text{Br}(h \to \bar{\psi}\psi)$ for a new fermion ψ, interacting with the Higgs through a dimension-6 operator suppressed by the scale Λ. These scenarios illustrate how even small couplings or high suppression scales can lead to visible exotic decays. Figure adapted from [32].

These "Higgs portal" models provide a powerful motivation for LLP searches at the LHC.

3.6 Experimental Searches and Constraints

The search for LLPs is a rapidly expanding frontier at the LHC. Given their unusual signatures, they can evade standard searches designed for promptly decaying particles. Experimental collaborations have developed a diverse portfolio of dedicated search strategies targeting various LLP decay signatures:

- **Displaced vertices or jets:** Searches for jets or lepton-jets originating from a vertex that is significantly displaced from the primary interaction point.

- **Disappearing tracks:** Searches for charged LLPs that decay into neutral, invisible particles within the tracker volume, leaving a track that abruptly ends.
- **Delayed signals:** Using the excellent timing capabilities of detectors to identify particles that arrive later than expected from a prompt decay.
- **Showers in the muon system:** Searching for LLPs that decay within the dense material of the calorimeters or the muon spectrometer, producing a localized shower of particles, like the search presented in this work.

Recent LLP searches by CMS and ATLAS have placed significant constraints on a wide range of models, targeting displaced leptons, jets, photons, and other anomalous signatures [7, 8]. In particular, the CMS Collaboration has developed reconstruction strategies in the muon system to identify electromagnetic showers arising from LLP decays, such as those predicted by hidden sector or portal models. In the Fig. 3.11 shows a plot of the current experimental limits on the branching ratio of Higgs decays into long-lived particles, compiled from multiple collider searches across different experiments.

Building on these methods, this thesis focuses on a novel experimental signature: displaced photon pairs from $a_\tau \to \gamma\gamma$ decays, produced in association with hadronically decaying τ leptons. This channel probes previously unexplored regions of parameter space for VLL scenarios.

Future proposed experiments like MATHUSLA, FASER, and CODEX-b are expected to significantly extend sensitivity to LLPs with extremely long lifetimes, complementing the capabilities of ATLAS and CMS [35].

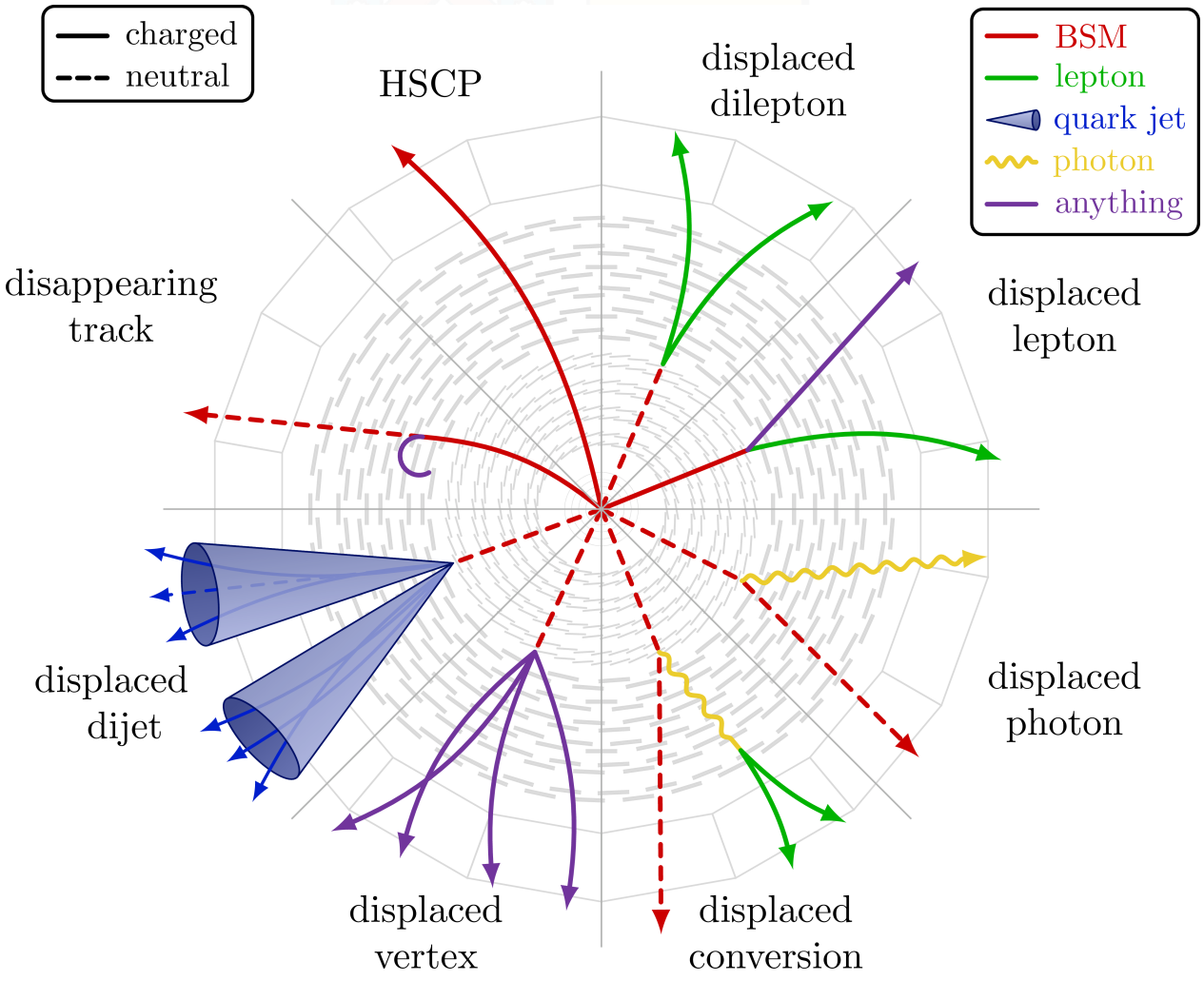

Figure 3.11: A schematic overview of various signatures of long-lived particles (LLPs) in a generic LHC detector cross-section. The diagram illustrates how different types of LLPs can result in distinct experimental signals, such as disappearing tracks, displaced vertices, and heavy stable charged particles (HSCPs). Figure created using a template by Izaak Neutelings [36].

Part II

Search for Long-lived Particles with the CMS Muon Detectors

Chapter IV: The CMS Experiment at the LHC

The Compact Muon Solenoid (CMS) is one of the two large general-purpose detectors at the LHC, designed to investigate a wide range of physics phenomena at the TeV energy scale. From the discovery of the Higgs boson to searches for supersymmetry and dark matter, CMS has played a central role in modern high-energy physics. Its design is optimized for excellent resolution in charged particle tracking, electromagnetic and hadronic calorimetry, and precise muon identification—making it especially powerful for detecting events with long-lived particles and displaced signatures.

This chapter describes the main components of the CMS detector, including the superconducting magnet, inner tracking system, calorimeters, and muon chambers. It also explains the trigger and data acquisition system (DAQ), which selects and records the most interesting collisions out of the billions occurring every second. Finally, the event reconstruction chain is presented, highlighting how raw detector signals are transformed into physics objects used in analysis.

By understanding the structure and performance of CMS, we gain the foundation needed to interpret experimental results and motivate new search strategies for physics beyond the Standard Model.

4.1 The Large Hadron Collider

The Large Hadron Collider (LHC) is the most powerful particle accelerator ever constructed. It is a 27 km circular ring located approximately 100 meters underground at CERN, near the border between Switzerland and France. Designed to probe the fundamental structure of matter, the LHC collides two counter-rotating beams of protons at center-of-mass energies of up to 14 TeV [37], with the aim of testing the mechanism of electroweak symmetry breaking and exploring phenomena beyond the Standard Model (BSM), including supersymmetry and potential dark matter candidates.

To achieve these high energies, protons are pre-accelerated through a series of injectors—Linac4, the Proton Synchrotron Booster (PSB), the Proton Synchrotron (PS), and the Super Proton Synchrotron (SPS)—before being injected into the LHC ring at 450 GeV. Inside the LHC, they are grouped into bunches of approximately 1.1×10^{11} protons, separated by 25 ns, leading to up to 40 million collisions per second. The beams are guided by 1232 superconducting dipole magnets operating at 8.33 T and cooled to 1.9 K using superfluid helium. Acceleration is provided by radiofrequency (RF) cavities running at 400 MHz.

A key operational parameter of the LHC is the instantaneous luminosity $\mathcal{L}$, which determines the rate of collisions:

$$\mathcal{L} = \frac{N_b^2 n_b f_{\text{rev}} \gamma}{4\pi \varepsilon_n \beta^*} F, \tag{4.19}$$

where N_b is the number of particles per bunch, n_b the number of bunches per beam, f_{rev} the revolution frequency, γ the Lorentz factor, ε_n the normalized transverse emittance, β^* the beta function at the interaction point, and F a geometric factor accounting for the crossing angle. High luminosity is crucial for probing rare processes with statistical significance.

The LHC ring is partitioned into eight sectors, each containing straight sections used for radio-frequency acceleration, beam diagnostics, and four major interaction points hosting detectors: ATLAS, CMS, ALICE, and LHCb is shown in Fig. 4.12. Among them, CMS and ATLAS are general-purpose detectors designed to explore a wide range of physics signatures.

During Run 2 (2015–2018), the LHC delivered proton-proton collisions at $\sqrt{s} = 13$ TeV, reaching a peak instantaneous luminosity of 2×10^{34} cm^{-2}s^{-1} and providing an integrated luminosity of over 150 fb^{-1} to each experiment [38]. The average number of interactions per bunch crossing (pileup) during this period was approximately $\langle \mu \rangle = 34$ [26].

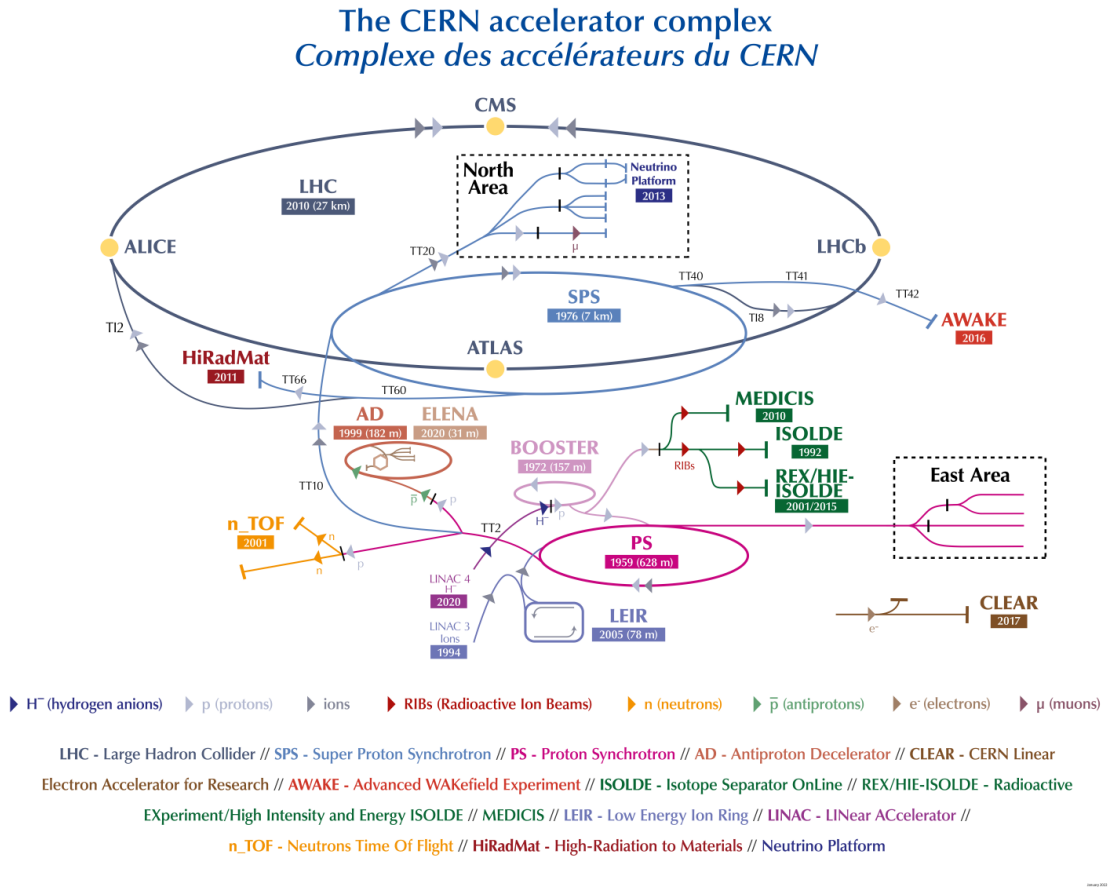

Figure 4.12: Diagram of the CERN accelerator complex. Protons are accelerated through Linac4, PSB, PS, and SPS before injection into the LHC ring. The four main experiments—ATLAS, CMS, ALICE, and LHCb—are located at separate interaction points. Source: [39].

The LHC also provides a unique environment to search for long-lived particles (LLPs), which are predicted by many extensions of the Standard Model. Such particles can travel macroscopic distances before decaying, and their detection requires specialized reconstruction techniques and trigger strategies. The CMS detector, described in the following section, is well-suited for this purpose, with extensive coverage and granularity in both its tracker and muon systems.

Given the importance of detecting particles that decay outside the inner tracker, such as long-lived particles (LLPs), the capabilities of the outer detectors—particularly the calorimeters and muon system—are crucial. This chapter focuses on the features of the CMS detector that are most relevant for reconstructing displaced electromagnetic signatures, especially those originating in the muon system.

4.2 The Compact Muon Solenoid Detector

The Compact Muon Solenoid (CMS) is a general-purpose detector located at Interaction Point 5 (IP5) of the LHC. It is designed to investigate a broad range of physics phenomena, including the Higgs boson, supersymmetry, dark matter candidates, and exotic long-lived particles (LLPs). The term "compact" refers to the highly integrated, dense configuration of its subsystems, which are all enclosed within a 21.6 m long, 14.6 m diameter structure, optimized for hermeticity and fine granularity.

CMS is built in a cylindrical geometry with approximate azimuthal symmetry, allowing for full 4π angular coverage. Its modular design features concentric layers of subdetectors surrounding the beam pipe, providing precise tracking, calorimetry, and muon identification. A schematic cross-section of the detector is shown in Fig. 4.13.

Among these subsystems, the muon system plays a critical role in both standard model measurements and searches for new physics.

The CMS muon system is composed of three technologies—Drift Tubes (DTs), Cathode Strip Chambers (CSCs), and Resistive Plate Chambers (RPCs)—covering the pseudorapidity range up to $|\eta| < 2.4$. These detectors are embedded in the steel return yoke of the solenoid and provide robust identification and momentum measurement of muons. However, their large volume and relatively low occupancy also make them ideal for detecting late-decaying neutral particles, such as long-lived particles (LLPs), that traverse the calorimeters before decaying.

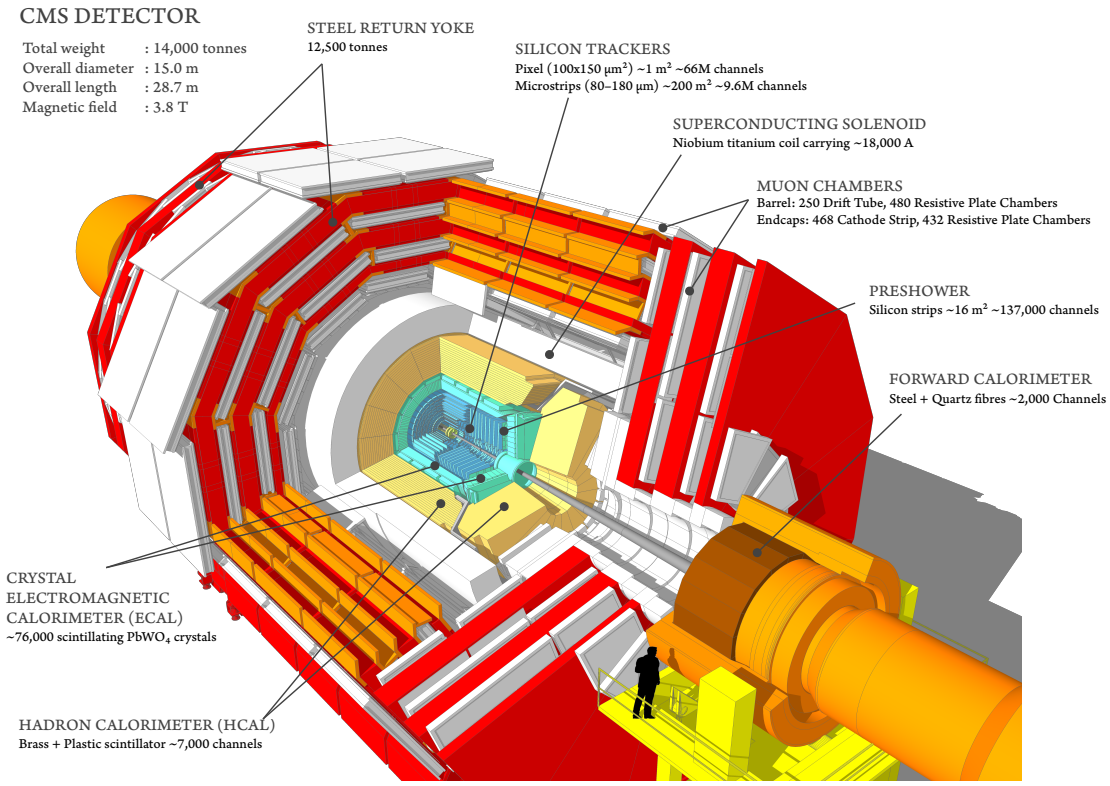

Figure 4.13: Cutaway view of the CMS detector after the Phase-1 pixel detector upgrade [40].

The CMS detector uses a right-handed coordinate system centered at the nominal collision point. The z-axis runs along the beam direction, the x-axis points radially towards the center of the LHC ring, and the y-axis points vertically upward. The azimuthal angle ϕ is measured in the x–y plane from the x-axis, and the polar angle θ is measured from the z-axis as shown in the Fig 4.14. These variables are essential for defining detector geometry, angular separations, and trigger conditions.

Rather than using the angle θ directly, high-energy physics experiments prefer the pseudorapidity η, defined as:

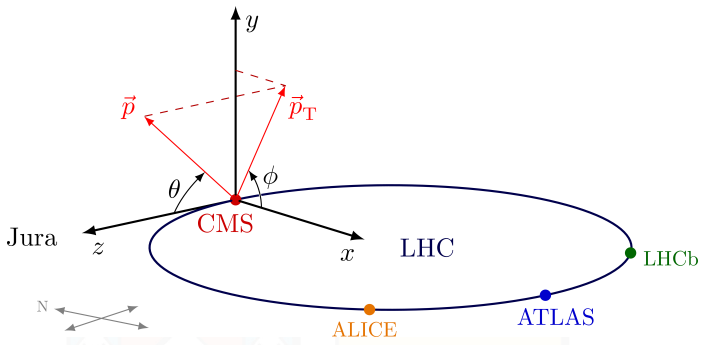

Figure 4.14: Coordinate system used in CMS. The pseudorapidity η is defined in terms of the polar angle θ and is commonly used due to its invariance under boosts along the beam axis. Image credit: CMS Collaboration [41].

$$\eta = -\ln\left[\tan\left(\frac{\theta}{2}\right)\right], \tag{4.20}$$

which is approximately equal to the rapidity y in the high-energy limit and remains invariant under longitudinal Lorentz boosts. This makes η a natural coordinate for defining detector regions and object acceptance.

In the transverse plane, the transverse momentum p_T and azimuthal angle ϕ are commonly used:

$$p_T = \sqrt{p_x^2 + p_y^2}, \quad \phi = \tan^{-1}\left(\frac{p_y}{p_x}\right). \tag{4.21}$$

These variables play a crucial role in event selection, trigger logic, and background discrimination. For instance:

- p_T thresholds are applied to reconstructed objects and trigger candidates. - η is used to define detector regions (e.g., barrel: $|\eta| < 1.2$; endcap: $1.2 < |\eta| < 2.4$). - ϕ is relevant for computing angular separations and isolation variables (e.g., $\Delta R = \sqrt{(\Delta\eta)^2 + (\Delta\phi)^2}$).

In searches for long-lived particles, these coordinates are indispensable. Displaced vertices are often characterized by large transverse impact parameters, and decays occurring in the muon system are localized in η and ϕ to reconstruct showers in specific chambers.

4.2.1 Superconducting Magnet

At the core of CMS lies a powerful superconducting solenoid magnet that provides a uniform magnetic field of 3.8 T. The solenoid has an inner bore of 6 m, a length of 12.5 m, and is constructed with four layers of niobium-titanium conductor. The magnetic field enables precise momentum measurement of charged particles by bending their trajectories inside the silicon tracker. The flux is returned via a 10,000-ton iron yoke, which also serves as the mounting structure for the muon system. A modeled map of the magnetic field is shown in Figure 4.15.

4.2.2 Tracker

The inner tracking system provides precise reconstruction of charged particle trajectories within the pseudo-rapidity range $|\eta| < 2.5$. It is composed entirely of silicon detectors and is located entirely inside the 3.8 T solenoidal magnetic field. The system consists of two main subsystems: the pixel detector and the silicon strip tracker.

The Phase-1 pixel detector includes four barrel layers and three endcap disks on each side, providing exceptional resolution close to the interaction point. The strip tracker comprises 10 barrel layers (divided into the Tracker Inner Barrel (TIB) and Tracker Outer Barrel (TOB)) and 12 disks in the endcap regions (Tracker Inner Disks (TID) and Tracker Endcap (TEC)). This layout ensures that most charged particles with

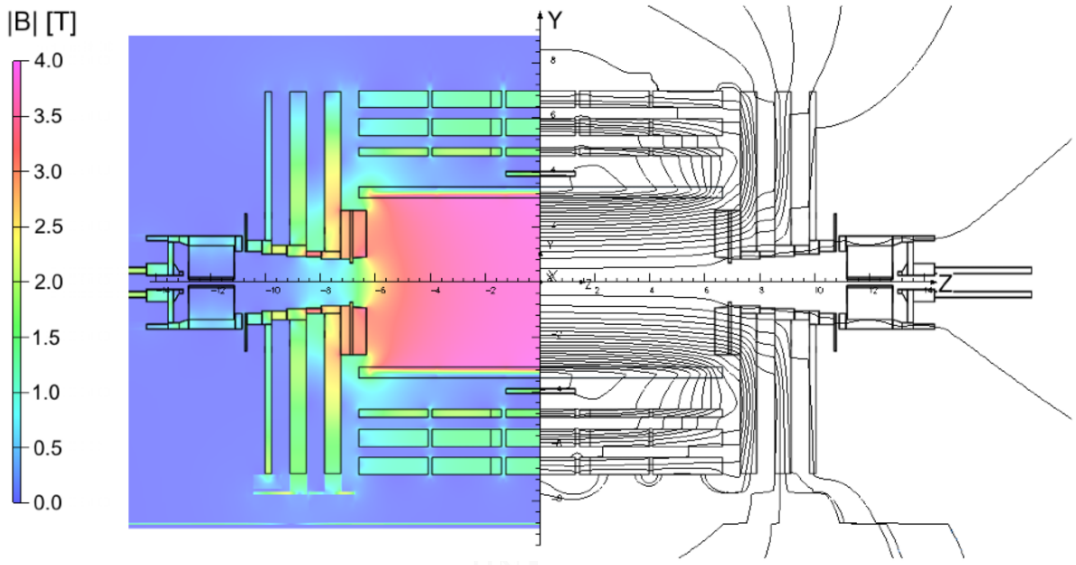

Figure 4.15: Longitudinal section of CMS showing the magnetic field magnitude and lines [42].

$p_T > 1$ GeV traverse at least 9 to 13 tracking layers, enabling robust track reconstruction. The schematic of the CMS Phase-1 tracking system is shown in Fig. 4.16

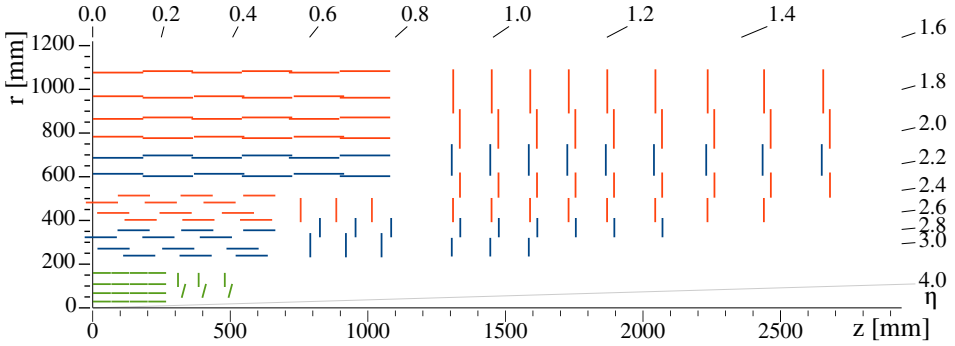

Figure 4.16: Schematic of one quarter of the CMS tracking system [43].

The CMS tracker provides outstanding spatial resolution. For tracks with $p_T > 10$ GeV, the transverse impact parameter resolution (d_0) is better than 20 μm, and the longitudinal impact parameter (z_0) resolution is approximately 25–40 μm, depending on η and pileup conditions [44]. These capabilities are essential for identifying primary and secondary vertices, particularly in high-density environments with up to 30–50 simultaneous interactions per bunch crossing during Run 2.

Tracking plays a crucial role in searches for long-lived particles. If the LLP decays within the tracker volume, its decay products may form a secondary vertex displaced from the beamline by several millimeters to centimeters. The fine granularity and high resolution of the pixel detector are particularly important in such cases. CMS tracking algorithms are optimized to reconstruct tracks with large impact parameters, enabling the identification of displaced vertices from LLP decays with high efficiency, even under high pileup conditions.

Furthermore, the tracker contributes significantly to pileup mitigation. By reconstructing multiple primary vertices within a single event, it enables the assignment of charged particle tracks to their respective collision vertices. This functionality is key for accurate object isolation and for computing corrected observables such as missing transverse momentum.

4.2.3 Electromagnetic Calorimeter

The CMS Electromagnetic Calorimeter (ECAL) is a homogeneous, high-resolution detector designed to measure the energies of electrons and photons. It is composed of nearly 76,000 lead tungstate ($PbWO_4$) scintillating crystals arranged in a barrel (EB) and two endcaps (EE). The high density (8.28 g/cm^3), short radiation length (0.89 cm), and fast response time (80% of light within 25 ns) of $PbWO_4$ make it ideal for use in a compact, high-granularity calorimeter inside the solenoid [45].

The ECAL is segmented into distinct geometric regions optimized for coverage and resolution. The barrel region covers $|\eta| < 1.479$ and consists of 61,200 crystals, each about 25.8 X_0 in depth. The endcaps extend coverage up to $|\eta| < 3.0$ with 14,848 shorter crystals (24.7 X_0). To enhance photon identification, a preshower detector composed of silicon strips and lead absorbers is placed in front of the EE, covering $1.653 < |\eta| < 2.6$.

Avalanche photodiodes (APDs) are used to detect scintillation light in EB, while vacuum phototriodes (VPTs) are used in EE due to their higher radiation tolerance. The compact crystal geometry ensures minimal lateral spread of electromagnetic showers, aiding in spatial separation of nearby particles. The ECAL achieves a relative energy resolution of 2–5% for electrons, as shown in Fig. 4.17, and is crucial for identifying LLP decays involving photons or electron pairs.

In the context of LLP searches, ECAL is essential for detecting displaced photons and electrons originating from late decays, which may exhibit non-standard topologies, large transverse impact parameters, or lack associated tracker activity.

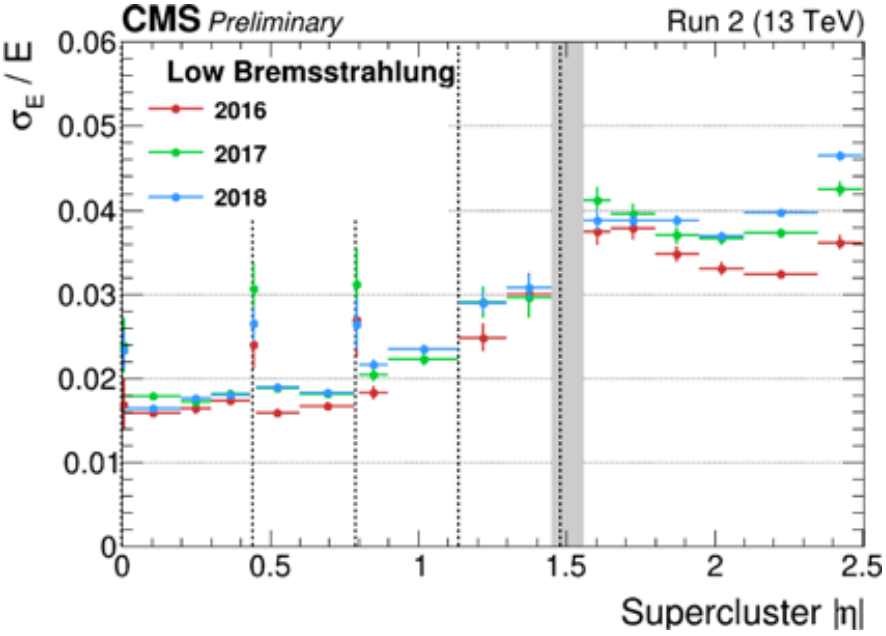

Figure 4.17: Relative energy resolution of the CMS ECAL as a function of pseudorapidity (η), measured using $Z \to e^+e^-$ events during Run 2. The stability across η demonstrates excellent performance despite radiation exposure and increased luminosity. Adapted from [46].

4.2.4 Hadron Calorimeter

Complementing the ECAL, the CMS Hadronic Calorimeter (HCAL) is responsible for measuring the energy of hadronic jets and is a key component in the reconstruction of missing transverse momentum (p_T^{miss}), particularly important in searches for LLPs that decay invisibly or outside the tracker.

The HCAL is a sampling calorimeter made of brass absorbers and plastic scintillator tiles. It is segmented longitudinally and read out by embedded wavelength-shifting fibers connected to hybrid photodiodes (HPDs) [47]. The system is divided into four major subsystems:

- HB (Hadron Barrel): $|\eta| < 1.3$

- HE (Hadron Endcap): $1.3 < |\eta| < 3.0$
- HF (Hadron Forward): $3.0 < |\eta| < 5.2$
- HO (Hadron Outer): extends hadronic depth in the barrel region up to $|\eta| < 1.2$

HB and HE are located inside the solenoid and provide 5.8 to 10 interaction lengths (λ_I) of absorber material, depending on η. The HO subsystem, located outside the solenoid, supplements HB with additional iron absorbers and scintillator layers to extend the depth to over 11.8 λ_I in total. The HF uses quartz fibers to detect Cherenkov radiation, allowing efficient identification of forward particles and extending detector acceptance for boosted topologies.

The layout of HCAL is shown in Fig. 4.18. The segmentation and geometry of the calorimeter system ensure efficient containment of hadronic showers and play a crucial role in identifying late or displaced hadronic decays from LLPs. In events where LLPs decay beyond the tracker or ECAL, HCAL often provides the only visible energy deposition.

Additionally, ECAL and HCAL information is combined in the Particle Flow algorithm to reconstruct jets and compute $\vec{p}_T^{\,\text{miss}}$, a central observable for LLP signatures involving undetected or delayed decays.

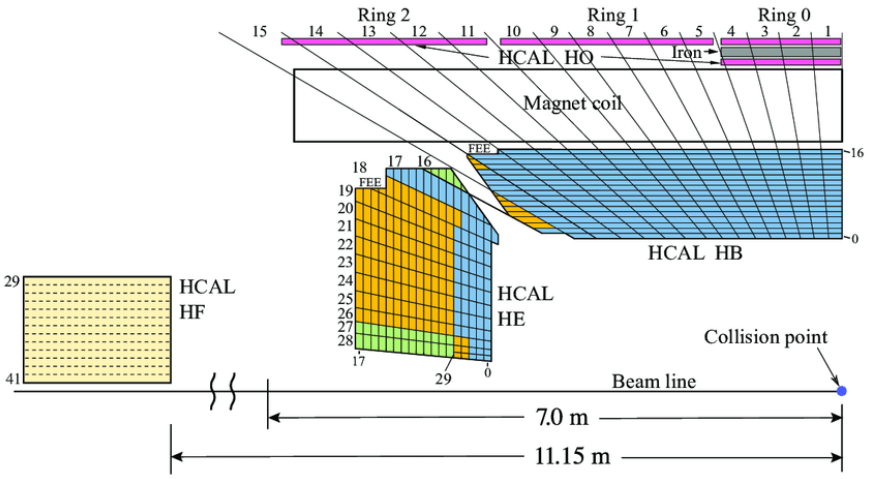

Figure 4.18: Schematic view of one quarter of the CMS hadron calorimeter (HCAL) during 2016 LHC operation. The layout shows the segmentation of the HB, HE, HO, and HF subsystems and the positioning of the front-end electronics (FEE). Adapted from [48].

4.2.5 Muon System

The CMS muon system forms the outermost layer of the detector and is designed to identify and measure muons, which are key signatures in many beyond the Standard Model (BSM) scenarios — including searches for long-lived particles (LLPs). Covering the pseudorapidity range $|\eta| < 2.4$, the system is embedded in the steel return yoke of the superconducting solenoid.

It comprises three different types of gaseous detectors (see Fig. 4.19):

- **Drift Tubes (DT)**, used in the barrel region ($|\eta| < 1.2$),
- **Cathode Strip Chambers (CSC)**, used in the endcaps ($0.9 < |\eta| < 2.4$),
- **Resistive Plate Chambers (RPC)**, present in both barrel and endcap regions ($|\eta| < 1.9$).

Drift Tubes (DTs): DTs are used in the barrel region, where radiation levels and particle fluxes are relatively low. Each chamber consists of multiple layers of aluminum tubes filled with a gas mixture and equipped with a central anode wire as shown in Fig 4.20. When a muon traverses a tube, it ionizes the gas; electrons drift toward the wire, and the drift time is measured to determine the hit position with a resolution of about 100–200 μm.

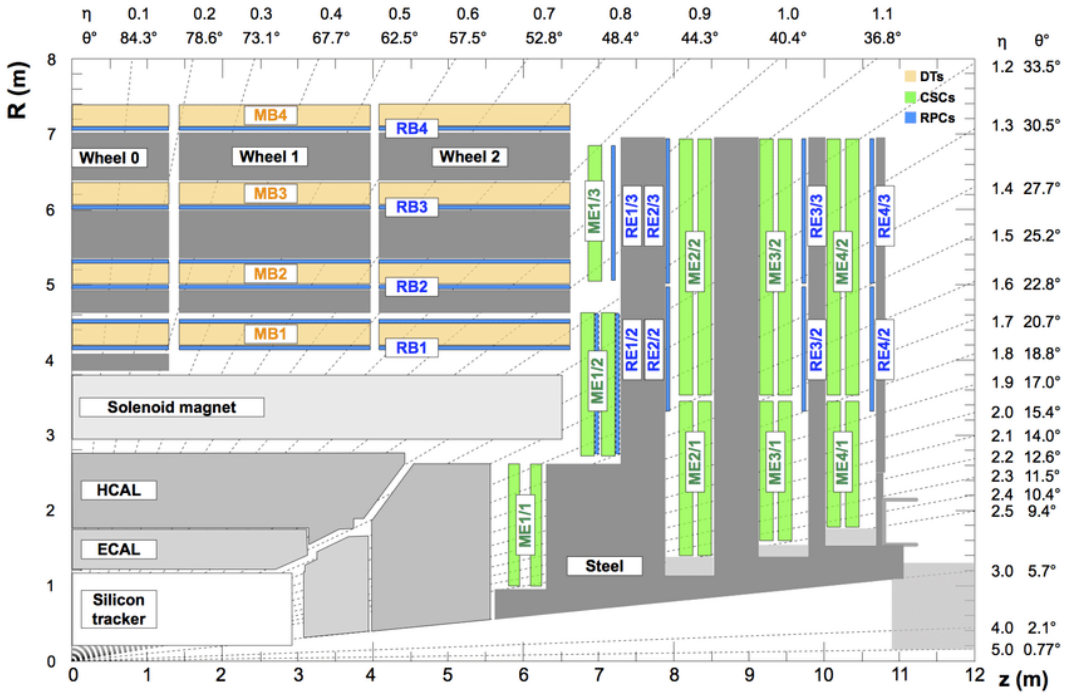

Figure 4.19: R–z cross section of a quadrant of the CMS detector, showing the arrangement of muon stations. DT chambers (light orange) are located in the barrel (MB), CSCs (green) in the endcaps (ME), and RPCs (blue) in both regions. The beamline runs horizontally from the interaction point at the lower left. Adapted from [49].

Each DT chamber includes two superlayers: one measuring the ϕ coordinate and another (in some chambers) the z coordinate. Chambers are arranged in four radial stations (MB1 to MB4) distributed across the steel yoke.

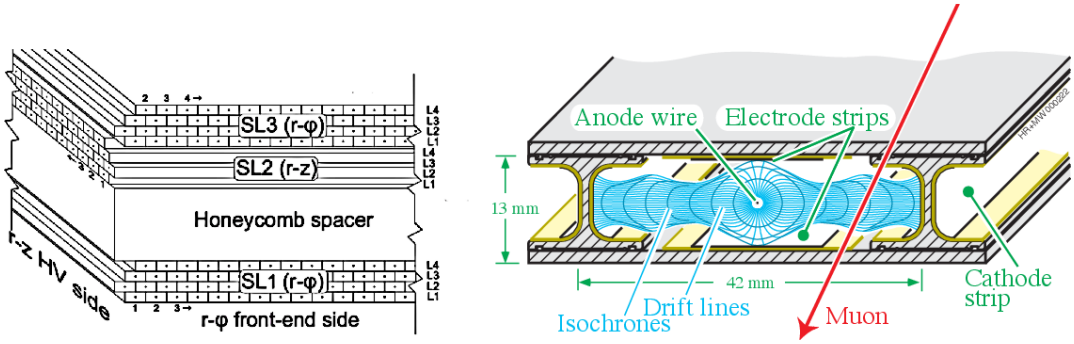

Figure 4.20: Left: schematic view of a DT chamber showing two superlayers. Right: cross-section of a drift tube cell with drift lines and isochrones indicating electron collection paths. Adapted from [49].

Cathode Strip Chambers (CSCs): CSCs are employed in the endcap regions, where radiation levels and magnetic field inhomogeneities are more severe. These multi-wire proportional chambers consist of radial anode wires and orthogonally segmented cathode strips aligned azimuthally. The intersection of a wire and the induced signal on the strip provides precise 2D position measurements.

Each CSC chamber includes six gas layers, offering multiple high-precision measurements per track as shown in Fig 4.21. The typical spatial resolution is better than 150 μm, and their fast response time makes them crucial for triggering in the forward region.

In this analysis, the focus is placed on CSCs due to their excellent spatial and temporal resolution, as well as their position in the forward region ($0.9 < |\eta| < 2.4$), where LLPs from boosted decays are more likely to be observed. The segmentation of the CSCs and their low background rate enable the reconstruction of

electromagnetic showers from displaced photon pairs, which is the key experimental signature targeted in this thesis.

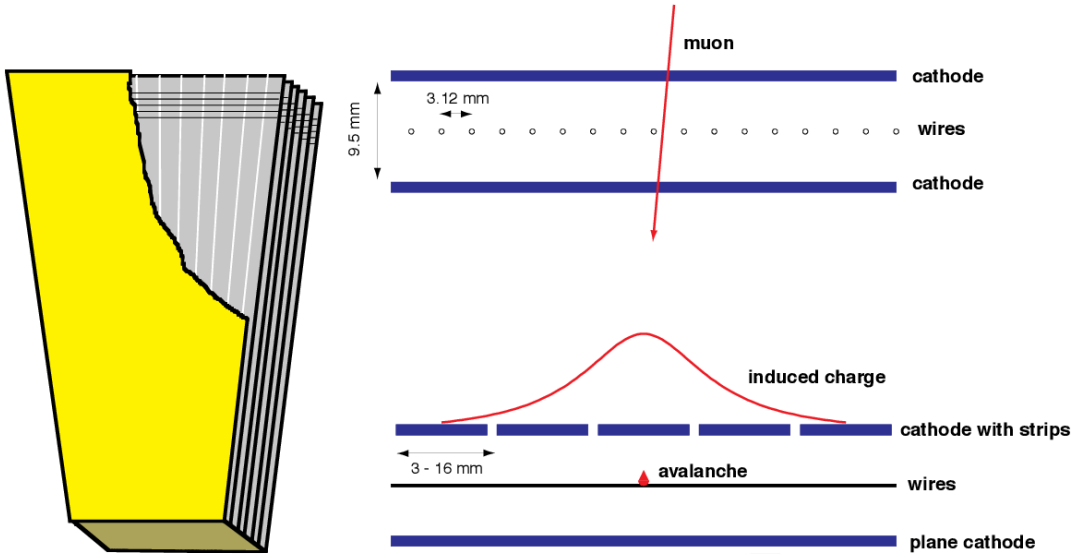

Figure 4.21: Left: cut-away diagram of a CSC chamber showing six detection layers and strip/wire orientation. Right: cross-section of a CSC gas gap illustrating avalanche formation and induced charge distribution on the cathode strips. Adapted from [49].

Muon System in LLP Searches: In LLP searches, the muon system is especially valuable. Its large volume and the dense iron yoke that returns the magnetic flux also serve as an ideal target for neutral LLPs, which might otherwise pass through the detector unseen. If an LLP decays within this material, it can produce a detectable shower. Decays of long-lived particles may occur outside the inner tracker and calorimeters, producing muons that do not originate from the beamline. In such scenarios, standalone muon reconstruction using DTs or CSCs becomes critical.

Additionally, RPCs provide timing information with resolutions of about 1–2 ns, enabling identification of delayed signals. This helps discriminate prompt backgrounds from genuine LLP decays. Signatures such as large impact parameter muons, displaced vertices reconstructed only in the muon system, and muon-only final states are typical in many LLP models.

Table 4.1: Comparison of muon detectors used in CMS.

Subsystem	Region	Coverage ($\|\eta\|$)	Resolution	Layers
Drift Tubes (DT)	Barrel	< 1.2	100–200 μm	8–12 (4 stations)
Cathode Strip Chambers (CSC)	Endcap	0.9–2.4	< 150 μm	6 (per chamber)
Resistive Plate Chambers (RPC)	Barrel/Endcap	< 1.9	$\sim$1–2 ns (timing)	6 (2 per station)

Detector Comparison and Performance Summary:

From Hits to Showers: CSC and DT in MDS Reconstruction Muon Detector Showers (MDS) are clusters of energy deposits in the muon chambers, often resulting from LLPs decaying within or near the steel return yoke of CMS. These decays may generate electromagnetic or hadronic showers, producing multiple spatially-correlated hits.

The reconstruction chain is as follows:

- **Hits:** Each chamber detects local signals — drift times in DTs or wire/strip pulses in CSCs.
- **Rechits (Reconstructed Hits):** Raw signals are converted to spatial points using detector geometry and calibration.

- **Segments:** Rechits in a single chamber are grouped into straight-line track stubs. In DTs, this is done layer-by-layer; in CSCs, it involves combining multiple gas gaps.
- **Showers (MDS):** Groups of RecHits or segments forming spatially dense clusters are identified as MDS candidates. These do not resemble single-muon trajectories and are instead consistent with collimated particle bursts from displaced decays.

The DT and CSC chambers are fundamental to this chain. Their multilayer structure and high spatial resolution allow for reliable standalone reconstruction of displaced signatures. These techniques enable CMS to remain sensitive to LLPs with decay lengths up to several meters and are directly employed in the search strategy discussed in Chapter V.

4.2.6 Trigger and Data Acquisition

The CMS trigger and data acquisition (DAQ) system is responsible for selecting, reading out, and assembling data from collisions at the LHC, which occur at a rate of 40 MHz. Since only a small fraction of these collisions produce events of physical interest, a multi-level trigger architecture is employed to reduce the event rate to a manageable level for offline processing.

Level-1 (L1) Trigger: The L1 trigger is a hardware-based system that uses information from the calorimeters and muon detectors with coarse granularity to make decisions within 3.8 μs. Fig. 4.22 shows the configuration of L1 trigger system during Run 2. It reduces the input rate from 40 MHz to approximately 100 kHz [50].

Trigger primitives (TPs) from CSCs, DTs, and RPCs are processed by three regional track finders:

- **Barrel Muon Track Finder (BMTF):** reconstructs muons in $|\eta| < 0.83$, combining DT and RPC TPs via the TwinMux board.
- **Overlap Muon Track Finder (OMTF):** covers $0.83 < |\eta| < 1.24$, integrating all three muon subsystems.
- **Endcap Muon Track Finder (EMTF):** reconstructs muons in $|\eta| > 1.24$ from CSCs and RPCs using Muon Port Cards and the CPPF system.

Track candidates are then ranked by p_T and quality and sent to the Global Muon Trigger (μGMT), which merges them with calorimetric objects for the final trigger decision [50].

High-Level Trigger (HLT): Events passing L1 are forwarded to the HLT, a software-based system running on a farm of ∼30,000 commercial CPUs. It reduces the event rate further to ∼1 kHz by performing near-offline-quality reconstruction using full detector information. The average decision latency is about 300 ms per event.

HLT paths are organized modularly: each path includes increasingly sophisticated filters targeting specific signatures (e.g., muons, jets, p_T^{miss}). Events rejected early in a path are not processed further, optimizing computing resources [51].

Data Acquisition (DAQ): The DAQ system receives L1-accepted events and assembles them through a two-stage event building architecture. First, front-end fragments are collected underground and grouped into super-fragments by Front-End Drivers (FEDs). These are transmitted to the surface and fully assembled by Readout Units (RUs) before reaching the HLT farm [51].

The system supports input rates up to 100 kHz and total throughput exceeding 100 GB/s. Accepted events are written to disk and later transferred to the Tier-0 computing center at CERN for permanent storage and processing [51].

Triggering on Long-Lived Particles: Long-lived particles often produce non-standard signatures such as displaced muons, delayed hits, or muon-only events with no tracker activity. Conventional prompt-object triggers are often inefficient for such scenarios.

During Run 2, p_T^{miss}-based triggers were the primary LLP handle, albeit with low efficiency. In Run 3, a new dedicated Level-1 High-Multiplicity Trigger (HMT) was deployed using CSCs. This trigger selects

events with anomalously high anode and cathode hit multiplicities in individual CSC chambers, enhancing sensitivity to showers produced by LLP decays in the muon system [52].

This was complemented by new HLT paths seeded on the HMT. These developments expanded the LLP-sensitive phase space by an order of magnitude and are central to the analyses presented in Chapter V.

System Architecture and Synchronization: The CMS Level-1 trigger system follows a modular FPGA-based architecture optimized for parallel processing of detector information. Trigger primitives (TPs) generated in the muon and calorimeter systems are routed through optical links to regional track finders — the BMTF, OMTF, and EMTF — each responsible for different η regions. These components reconstruct muon candidates independently and forward them to the Global Muon Trigger (μGMT), which merges them with calorimetric objects before passing the decision to the Global Trigger (μGT) [50].

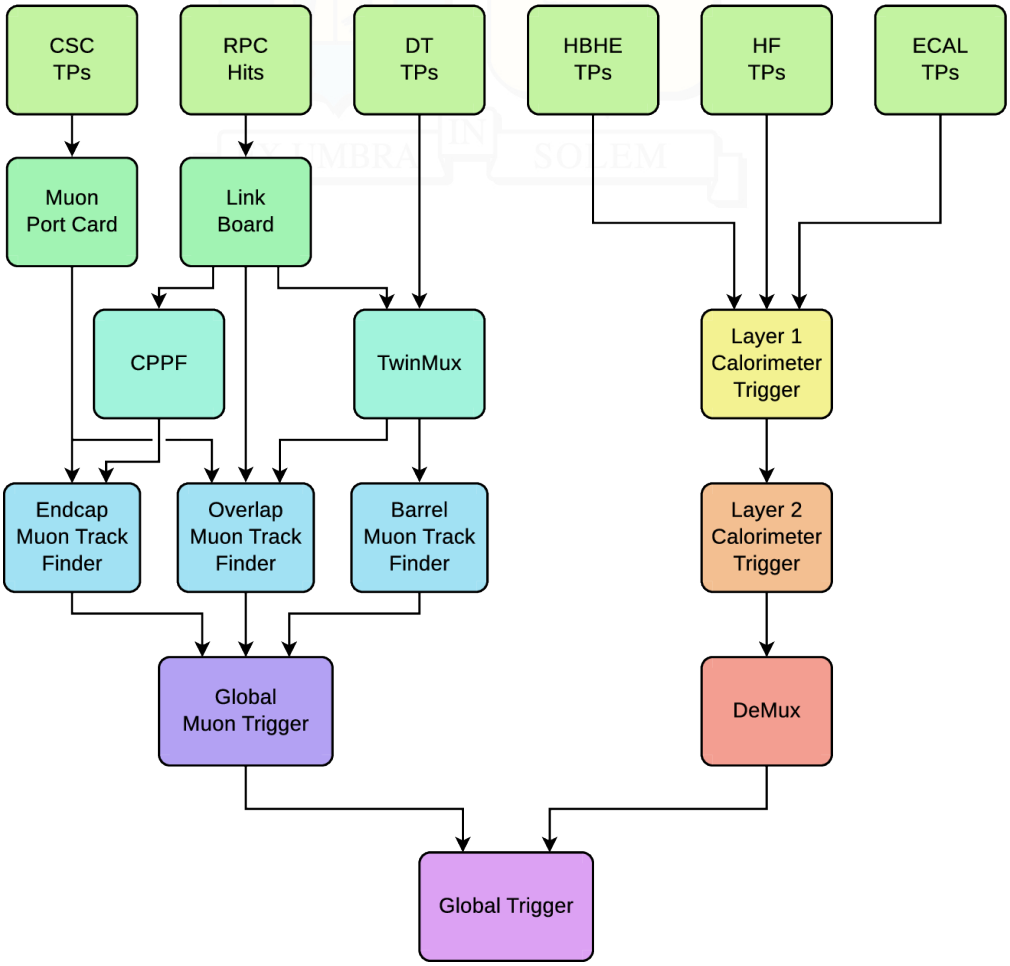

Figure 4.22: Schematic diagram of the upgraded CMS Level-1 trigger system architecture used during Run 2. Muon and calorimeter TPs are processed in parallel and fed into the Global Trigger via dedicated FPGA-based logic modules. Adapted from [50].

To ensure correct temporal alignment across all detector components, the system uses a centralized Trigger and Timing Control (TTC) system. This distributes the 40 MHz LHC clock, the Level-1 Accept (L1A) signal, and synchronization commands to all subsystems. Timing alignment within and between DT, CSC, and RPC systems is critical for producing coherent muon track candidates at the L1 stage.

All data flow through custom AMC13 modules that act as the bridge between the trigger and DAQ. Event fragments from Front-End Drivers (FEDs) are gathered and transmitted via optical links to Readout Units (RUs) located on the surface. These elements complete the full event assembly before delivery to the High-Level Trigger (HLT) [50].

This architecture enables high throughput (up to 100 kHz) with low latency, while providing the flexibility to implement advanced selection algorithms. In particular, it allows for the deployment of custom strategies targeting rare and unconventional signatures—such as displaced muon showers from long-lived particle decays—discussed in Chapter 5.1.

Nonetheless, standard trigger algorithms are typically optimized for prompt objects originating near the interaction point. Consequently, LLPs that decay outside the tracker may leave atypical signatures that fail to match standard trigger patterns. This challenge has driven the development of dedicated algorithms capable of identifying displaced objects already at the trigger level.

4.2.7 Data Format and Event Reconstruction

The reconstruction of displaced signatures in CMS requires specialized algorithms capable of identifying particles originating far from the interaction point. While standard reconstruction chains are optimized for prompt objects, the CMS muon system and calorimeters provide a unique opportunity to detect and reconstruct displaced electromagnetic activity from LLP decays.

Once an event is accepted by the High-Level Trigger (HLT), it is transferred to the Tier-0 computing center at CERN, where a prompt reconstruction is performed on a subset of events for quality monitoring and rapid calibration. A full reconstruction of the entire dataset is typically completed within 48 hours to avoid buffer overflows in the storage system [53].

The CMS data model includes several event formats with increasing levels of abstraction and decreasing size:

- **RAW:** Contains unprocessed detector output (order of MBs per event), mainly used for calibration and reprocessing.
- **RECO:** Includes reconstructed hits (RecHits), clusters, and high-level objects (jets, muons, electrons), about 4 MB/event.
- **AOD (Analysis Object Data):** Derived from RECO, includes all high-level objects and essential rechits, 0.4 MB/event.
- **MINIAOD:** Compact format (40 kB/event) sufficient for 95% of Run 2 analyses.
- **NANOAOD:** Extremely compact format (1–2 kB/event) containing only final physics objects; used in up to 70% of CMS analyses [53, 54].

Particle Flow (PF) Reconstruction: CMS employs a global reconstruction algorithm called *Particle Flow* (PF), which aims to reconstruct and identify every particle in an event using information from all subdetectors. This method links tracker tracks, ECAL/HCAL clusters, and muon segments to form PF candidates, classified as electrons, muons, photons, charged hadrons, or neutral hadrons [53]. Fig. 4.23 shows a sketch CMS detector with the behavior of different particles passing through it from the interaction point to the muon chambers.

Track reconstruction is central to PF. It begins with seeding (using pairs or triplets of hits), followed by trajectory building using a combinatorial Kalman Filter, and final fitting and selection based on track quality metrics. Tracks are independently built in the tracker and muon systems; they are matched and combined into global muons when compatible [53].

Calorimeter clusters are formed separately in ECAL, HCAL, and preshower layers, and then linked to tracks to refine energy and direction estimates. Electrons and photons are distinguished based on ECAL supercluster shape, associated tracks, and energy/momentum matching. Muons are identified by matching tracker tracks to muon chamber segments.

Jets, Taus, and Missing Transverse Momentum: PF candidates are clustered into jets using the anti-k_T algorithm with a distance parameter of $R = 0.4$ [55]. Jet energy corrections are applied to account for pileup and detector response. Hadronically decaying tau leptons (τ_h) are reconstructed using the Hadrons-Plus-Strips algorithm, and identified using DeepTau, a deep-learning-based discriminator [56].

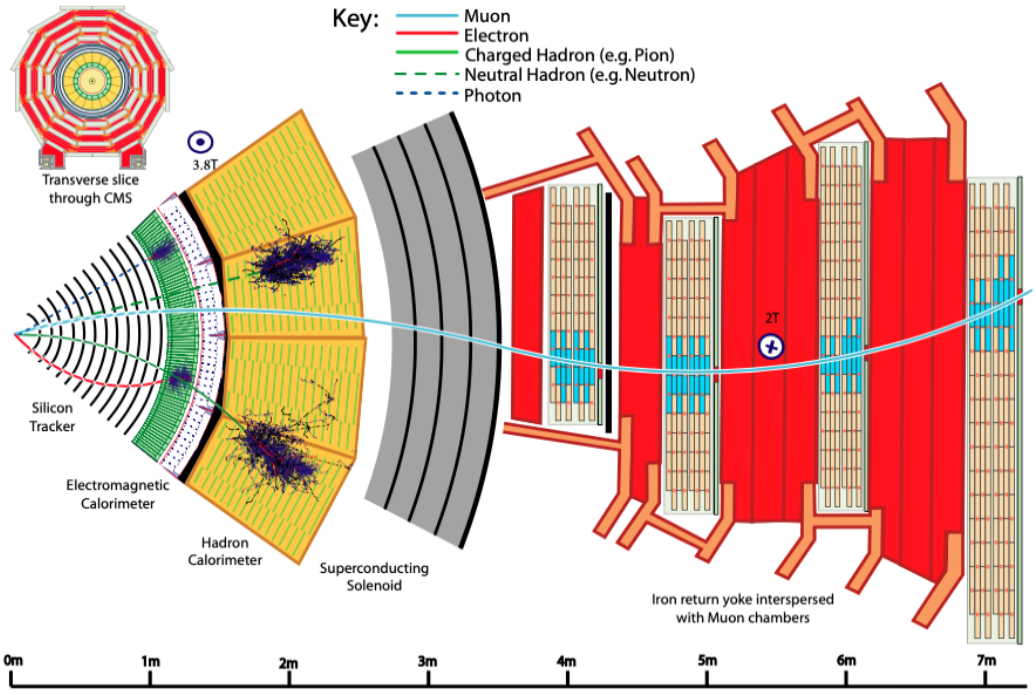

Figure 4.23: Schematic view of the expected behavior of different particles across the CMS detector layers, from interaction point to muon chambers. Adapted from [53].

The missing transverse momentum ($\vec{p}_T^{\text{miss}}$) is computed as the negative vector sum of all reconstructed PF candidates:

$$\vec{p}_T^{\text{miss}} = -\sum_{i=1}^{N} \vec{p}_{T,i}$$

Jet energy corrections and pileup mitigation techniques are propagated to this computation to ensure accurate reconstruction, essential for many searches involving neutrinos or undetected LLP decays. The final physics objects reconstructed via the Particle Flow algorithm and stored in the NANOAOD format form the basis of the analysis presented in Chapter V.

4.2.8 Suitability for Long-Lived Particle Searches

The CMS detector provides a unique environment for detecting long-lived particles (LLPs), thanks to its excellent spatial, temporal, and kinematic coverage. Several subsystems contribute crucially to this capability:

- **High-granularity silicon tracking** enables the reconstruction of displaced vertices with sub-100 μm resolution, essential for LLP decays occurring millimeters to centimeters from the interaction point.
- **The muon system** allows detection of particles decaying at large radii — even several meters from the beamline — and supports standalone reconstruction when tracker information is absent.
- **Fast-timing detectors**, such as RPCs, provide nanosecond-scale time resolution, allowing identification of out-of-time signals typical of LLP decays.
- **Hermetic calorimetry** enables full event energy reconstruction and the measurement of missing transverse momentum, vital for decays involving invisible particles.
- **Dedicated trigger and reconstruction algorithms**, such as those based on Muon Detector Showers (MDS), high-multiplicity CSC activity, or p_T^{miss}-based triggers, target signatures atypical of prompt Standard Model processes.

These features collectively allow CMS to explore regions of the parameter space in beyond-the-Standard-Model (BSM) scenarios that would be inaccessible using only prompt-object searches. LLPs decaying within the tracker, calorimeters, or muon system — including those with delayed, displaced, or non-isolated signatures — can be efficiently reconstructed and selected.

Table 4.2: Overview of CMS subdetectors and their properties relevant to LLP searches.

Subsystem	**Technology**	**Coverage ($\|\eta\|$)**	**Role in LLP Search**
Tracker	Si pixels + strips	< 2.5	Displaced vertices, track stubs
ECAL	$PbWO_4$ crystals	< 3.0	EM showers, γ, $e^{\pm}$
HCAL	Brass + scintillator	< 5.0	Missing energy, displaced jets
Muon System	DTs, CSCs, RPCs	< 2.4	MDS, standalone muons, delayed hits

The detector design, reconstruction capabilities, and dedicated trigger paths position CMS as one of the most powerful detectors in the world for LLP searches. The following chapter presents a concrete application of these features in a data-driven analysis targeting long-lived particles decaying within the CMS muon system.

Chapter V: Search for Vector-like Leptons with Long-lived Particle Decays in the CMS Muon System

5.1 Introduction

This chapter presents a search for long-lived particles (LLPs) predicted in a simplified model involving heavy vector-like leptons (VLLs). The analysis was conducted using the full Run 2 dataset collected with the CMS detector at the LHC, corresponding to an integrated luminosity of 138 fb^{-1} at a center-of-mass energy of $\sqrt{s} = 13$ TeV [57]. I contributed directly to the development, implementation and validation of this analysis during my time with the CMS LLP group at Fermilab.

The theoretical motivation arises from the model proposed in [58], which introduces new heavy singlet leptons τ' that couple weakly to the Standard Model (SM). These VLLs can decay via several channels, but particular interest is placed on the decay $\tau' \to \tau a_\tau$, where a_τ is a light long-lived pseudoscalar boson with a mass of approximately 2 GeV. This boson decays exclusively to two photons: $a_\tau \to \gamma\gamma$ as shown in Fig. 5.24.

The production of VLLs at the LHC proceeds predominantly through the annihilation of quark-antiquark pairs in the initial state:

$$q\bar{q} \to \gamma^*/Z \to \tau'^{+}\tau'^{-},$$

followed by the decay of each τ' into a τ lepton and an a_τ boson. If the a_τ decays inside the steel return yoke of CMS, the resulting photons may initiate electromagnetic showers in the muon detectors. These energy deposits can be reconstructed as *Muon Detector Showers* (MDS), providing a clean and distinctive signature of long-lived particle decays.

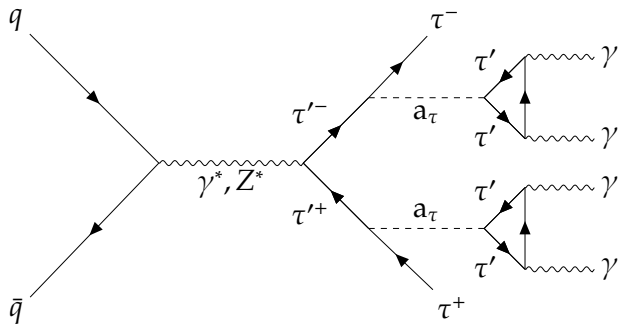

Figure 5.24: Feynman diagram illustrating the pair production of singlet vector-like leptons (τ'), each decaying into a Standard Model τ lepton and a light long-lived pseudoscalar boson (a_τ). In this benchmark model, $a_\tau \to \gamma\gamma$, and the photons may be detected via showers in the CMS muon system. Adapted from [57].

The search strategy uses dedicated reconstruction algorithms to identify clusters of muon chamber hits consistent with electromagnetic showers from displaced decays. Events are selected using a high missing

transverse momentum (p_T^{miss}) trigger, and candidate showers are classified according to whether they occur in the Drift Tubes (DT) or Cathode Strip Chambers (CSC) of the CMS muon system.

This chapter details the theoretical motivation, dataset and simulation samples, reconstruction techniques, event selection, background estimation, systematic uncertainties, and results of the search. Limits are set on the production cross section of $\tau'^{+}\tau'^{-}$ as a function of the proper decay length $c\tau$ of a_τ, using signal regions defined by the location and properties of reconstructed MDS objects.

Since the a_τ decays into two photons, the resulting electromagnetic energy deposits do not leave tracks in the inner tracker. Instead, these photons may interact with the steel return yoke and initiate electromagnetic showers within the muon system. This feature motivates the reconstruction of Muon Detector Showers (MDS), which rely solely on localized energy deposits in the DT and CSC chambers, rather than on associated charged particle tracks.

5.2 Datasets

This analysis uses data and simulated samples to search for events consistent with the production and decay of vector-like leptons (VLLs) into long-lived pseudoscalar bosons a_τ, which subsequently decay into two photons. The dataset corresponds to the full Run 2 proton-proton collisions collected by the CMS detector at $\sqrt{s} = 13$ TeV.

5.2.1 Data

Data used in this search were collected during 2016–2018, totaling an integrated luminosity of 138 fb^{-1}:

- 2016: 35.9 fb^{-1}
- 2017: 41.5 fb^{-1}
- 2018: 59.7 fb^{-1}

Events are required to pass the high-level trigger (HLT) paths designed for displaced showers in the muon system, seeded by CSC and DT activity. To suppress backgrounds and enhance sensitivity to long-lived particles, only events with missing transverse energy (MET) greater than 200 GeV are retained.

5.2.2 Signal MC Simulation

The simulation of signal events is crucial to understand the expected spatial and kinematic distributions of LLP decays in the CMS muon system. These distributions guide the design of signal regions, trigger strategies, and reconstruction algorithms.

Simulated signal samples are generated using a simplified model implemented via `FeynRules` [59], exported to a UFO model, and interfaced with `MadGraph5_aMC@NLO` [60] for leading-order matrix element generation. Parton showering and hadronization are performed using `PYTHIA 8.230` [61], with the CUETP8M1 underlying event tune [62]. Detector simulation is carried out with the full CMS software stack based on `GEANT4` [63].

The benchmark model assumes pair production of vector-like leptons τ', each decaying via $\tau' \to \tau a_\tau$, with $m_{\tau'} = 300$ GeV and $m_{a_\tau} = 2$ GeV. The pseudoscalar a_τ is long-lived and decays exclusively to two photons. Several samples are generated with different $c\tau$ values, ranging from millimeters to several meters, to map out the geometric acceptance and lifetime-dependent sensitivity of the detector.

Generated events are reweighted to target different proper lifetimes using generator-level decay time information [57]. This avoids regenerating large simulated samples and allows for precise interpolation across lifetime hypotheses.

5.2.2.1 Gen-level Properties

The kinematic properties of the generated τ' and a_τ particles are studied to understand their acceptance and decay behavior. Figures 5.25 show the transverse momentum (p_T) of the τ' and the pseudorapidity (η) of the a_τ, respectively.

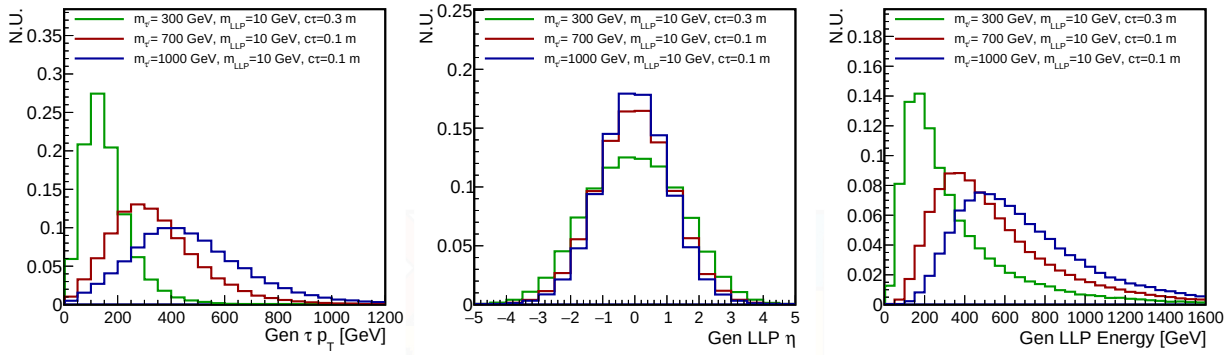

Figure 5.25: Signal gen-level properties of the tau lepton and LLP from the vector-like lepton decay in simulation: τ p_T (left), LLP η (center), and LLP energy (right).

5.2.2.2 LLP Lifetime Reweighting

To maximize coverage of the LLP lifetime parameter space, signal events are reweighted to different proper decay lengths $c\tau$ using the generator-level lifetime information. This allows extrapolation of acceptance for intermediate decay lengths without regenerating events. The decay length distribution of a_τ in the lab and rest frames is shown in Figures 5.26.

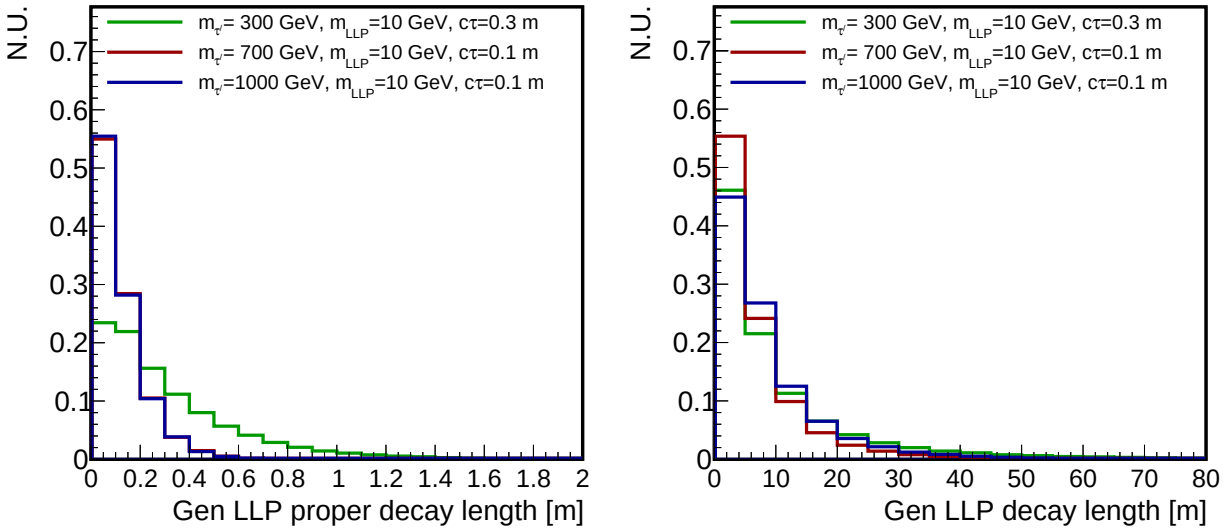

Figure 5.26: Signal gen-level properties of LLP from the vector-like lepton decay in simulation. (Left) LLP proper decay length, and (right) decay length in lab frame.

To interpolate between simulated a_τ lifetimes, an event-by-event reweighting procedure is applied. Given a simulated lifetime τ_{old} and a target lifetime τ_{new}, the reweighting factor is calculated as:

$$w = \left(\frac{\tau_{\text{old}}}{\tau_{\text{new}}}\right)^2 \exp\left[(t_1 + t_2)\left(\frac{1}{\tau_{\text{old}}} - \frac{1}{\tau_{\text{new}}}\right)\right], \tag{5.22}$$

where t_1 and t_2 are the proper decay times of the two LLPs in the event. This allows continuous sensitivity evaluation across a range of $c\tau$ values.

5.2.2.3 LLP Decay Geometric Acceptance

The geometric acceptance of the CMS muon system is used to determine where the a_τ decays are likely to be observed. Figure 5.27 shows the distribution of $\beta\gamma$ for the a_τ, which influences decay distance.

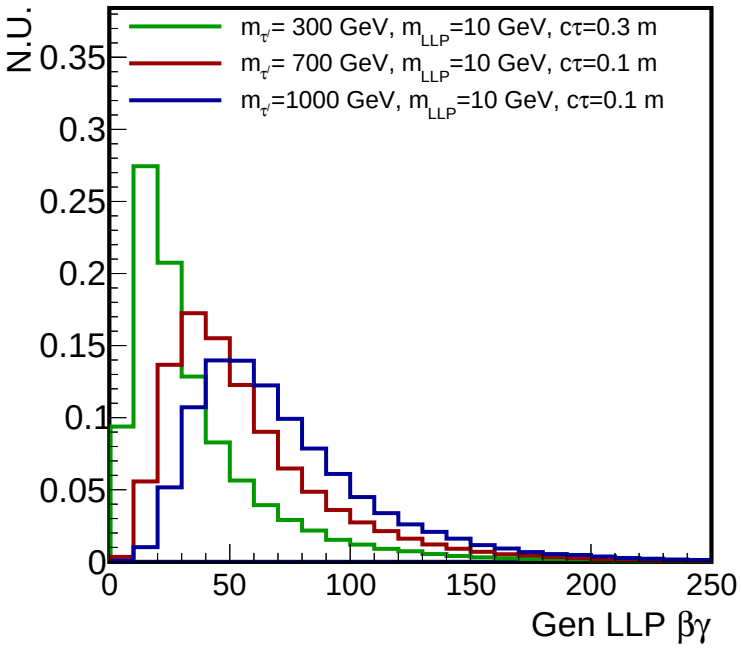

Figure 5.27: Distribution of $\beta\gamma$ for the a_τ LLP.

The acceptance as a function of $c\tau$ is shown for the DT and CSC regions, with and without a MET cut, in Figures 5.28 and 5.29.

The study of these generator-level distributions is essential for understanding the spatial and kinematic behavior of the LLP decays. Variables such as the η, energy, and $\beta\gamma$ of the a_τ directly influence the decay position and its probability of intersecting the instrumented regions of the CMS muon system. This information guides the design of signal regions, the development of clustering algorithms in DT and CSC chambers, and the optimization of event selection criteria for enhanced signal sensitivity across a range of lifetimes.

These simulated and data samples provide the foundation for the trigger and reconstruction studies described in the next sections.

5.3 Trigger Selection

Triggering is essential for the identification of signal-like events in this analysis. The signature targeted involves large missing transverse momentum (MET) and displaced activity in the muon system, as expected from long-lived particle decays.

In particular, the analysis exploits High-Level Trigger (HLT) paths designed to select events with large missing transverse energy *excluding contributions from reconstructed muons*, denoted as MET_{NoMu}. This choice ensures sensitivity to events where the final-state muons are non-prompt or poorly reconstructed due to the displaced nature of the LLP decays.

These triggers were chosen to maximize signal acceptance while suppressing backgrounds associated with prompt activity or well-reconstructed muons. The MET_{NoMu} requirement is effective in selecting events containing invisible or displaced decays not associated with tracks in the inner tracker.

To further validate trigger performance, the efficiency of the MET_{NoMu} requirement is studied using

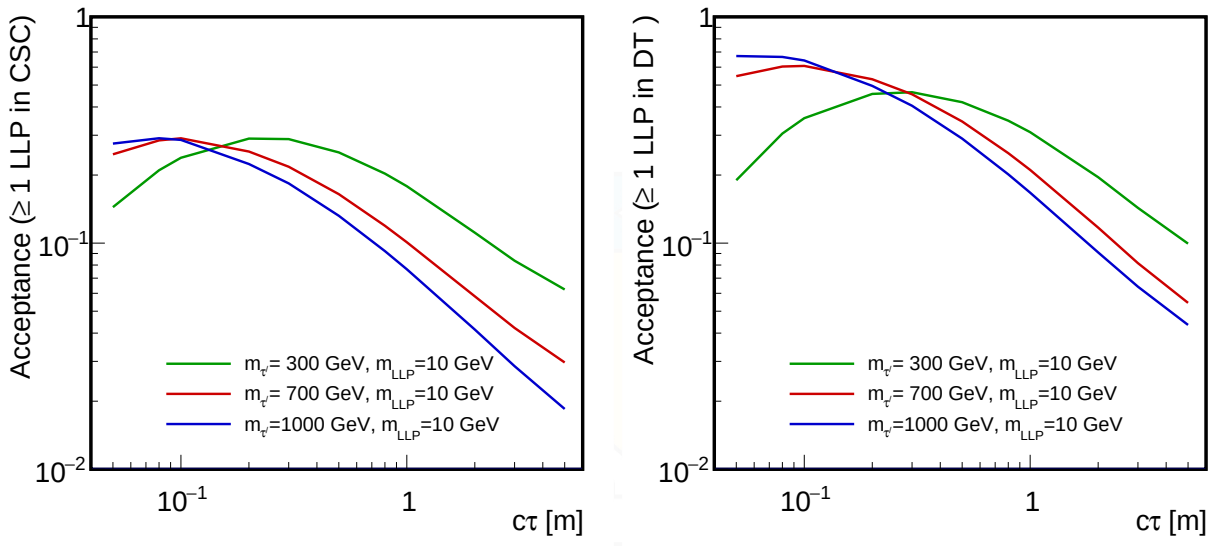

Figure 5.28: Geometric acceptance of at least one LLP decaying in CSC (left) and DT (right) as a function of $c\tau$. No additional event selection is applied.

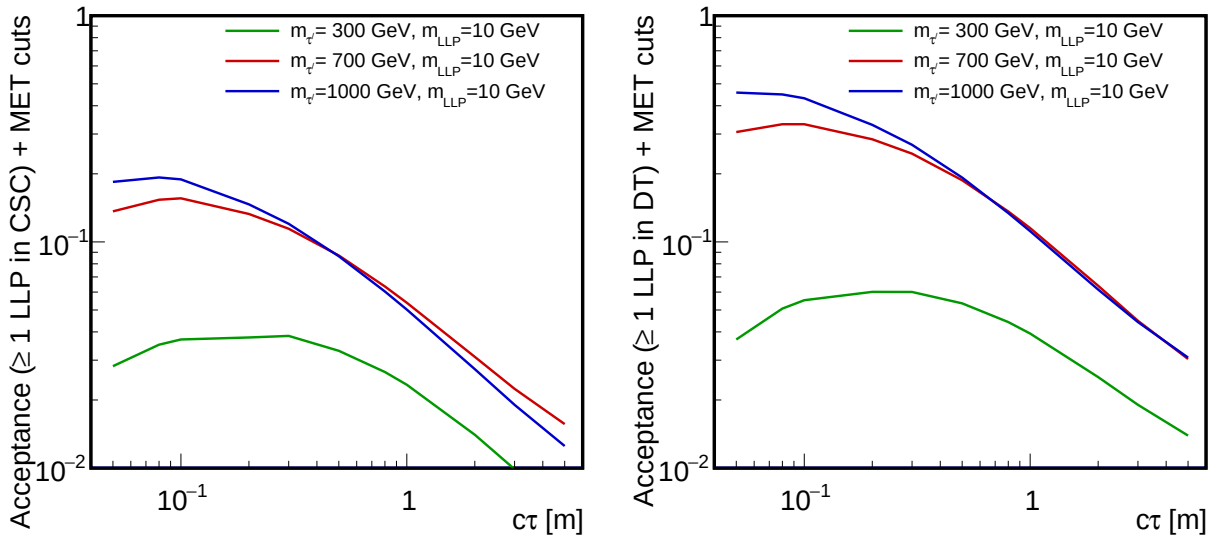

Figure 5.29: Fraction of events with LLP decay in CSC (left) and DT (right) and passing MET $>$ 200 GeV selection, as a function of $c\tau$.

Table 5.3: Summary of HLT paths used for each data-taking year. All triggers require $MET_{\text{NoMu}} > 120$ GeV at HLT level.

Year	Trigger Name	Description
2016	`HLT_NoMu120_MET_CaloMET`	Calorimeter-based MET without muons
2017	`HLT_PFMETNoMu120_PFMHTNoMu120_IDTight`	PF-based MET and MHT, no muons
2018	`HLT_PFMETNoMu120_PFMHTNoMu120_IDTight`	Same as 2017

signal simulation. Fig. 5.30 shows the trigger turn-on curves for each year, confirming that the chosen threshold of $MET > 200$ GeV (applied offline) lies in the plateau region of the HLT efficiency.

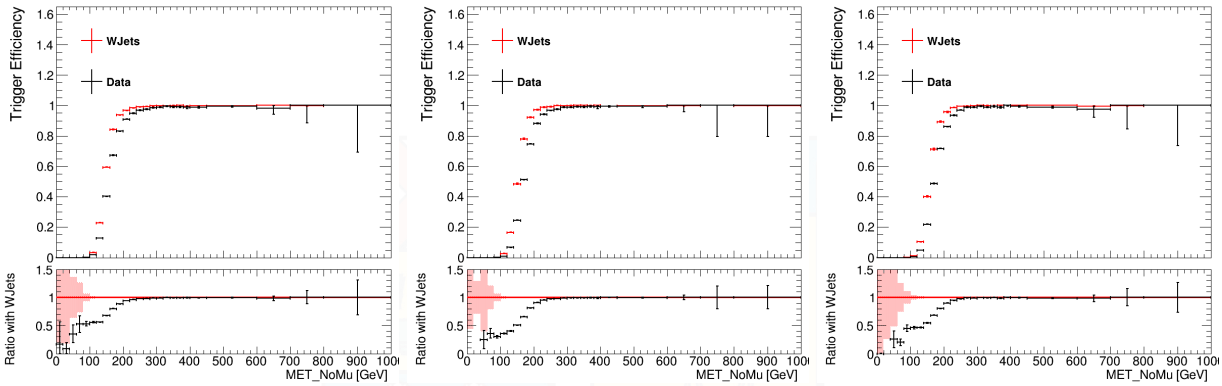

Figure 5.30: Trigger efficiency curves for the MET_{NoMu} requirement in simulated signal samples for 2016 (left), 2017 (center), and 2018 (right). The offline MET cut of 200 GeV lies on the plateau of each curve.

Additionally, the offline MET distribution for signal events passing both CSC and DT shower selection is shown in Figure 5.31, further validating the trigger strategy.

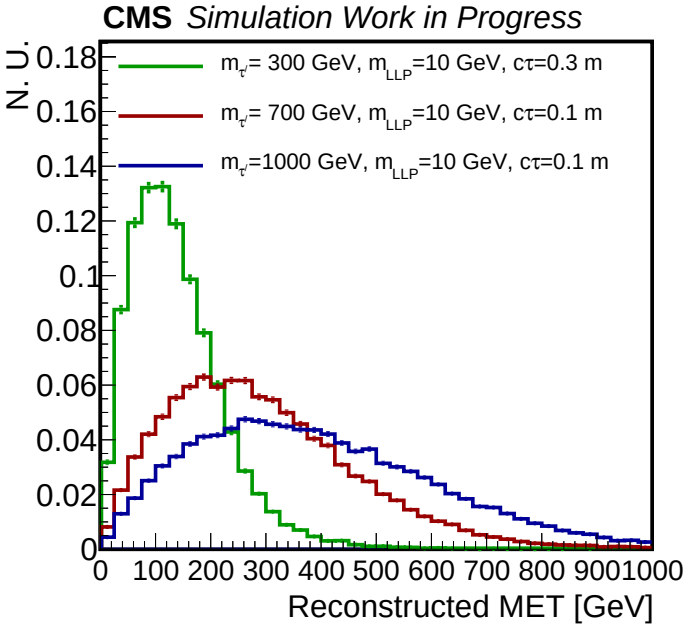

Figure 5.31: Reconstructed MET for different signal hypotheses.

5.4 Event Reconstruction and Object Identification

5.4.1 Primary Vertex

The primary interaction vertex is reconstructed from tracks using the deterministic annealing algorithm [64], optimized for Run 2 conditions. Events are required to have at least one reconstructed primary vertex with $\geq$ 4 associated tracks, located within 24 cm along the z-axis and within 2 cm in the transverse plane from the detector center [57].

5.4.2 CSC and DT Clusters

Long-lived particles (LLPs) that decay inside the CMS muon system often leave localized patterns of hits in the Cathode Strip Chambers (CSCs) or Drift Tubes (DTs), forming clusters that can be reconstructed algorithmically. These clusters originate from electromagnetic showers initiated by the decay products of the light pseudoscalar boson $a_\tau \to \gamma\gamma$, which do not leave charged particle tracks, making them identifiable primarily via their energy deposits in the muon subdetectors.

Clusters are reconstructed using the DBSCAN algorithm [65], grouping spatially close RecHits within a cone of $\Delta R = \sqrt{(\Delta\eta)^2 + (\Delta\phi)^2} < 0.2$. A minimum of 50 RecHits is required per cluster to ensure quality and suppress noise. When both DT and CSC clusters exist in the same η region, CSC clusters are preferred due to their higher granularity.

Figure 5.32 shows the number of RecHits per cluster for LLP decays in the CSC (left) and DT (right) detectors for various vector-like lepton (VLL) masses. These distributions help discriminate genuine LLP-induced activity from instrumental or cosmic backgrounds.

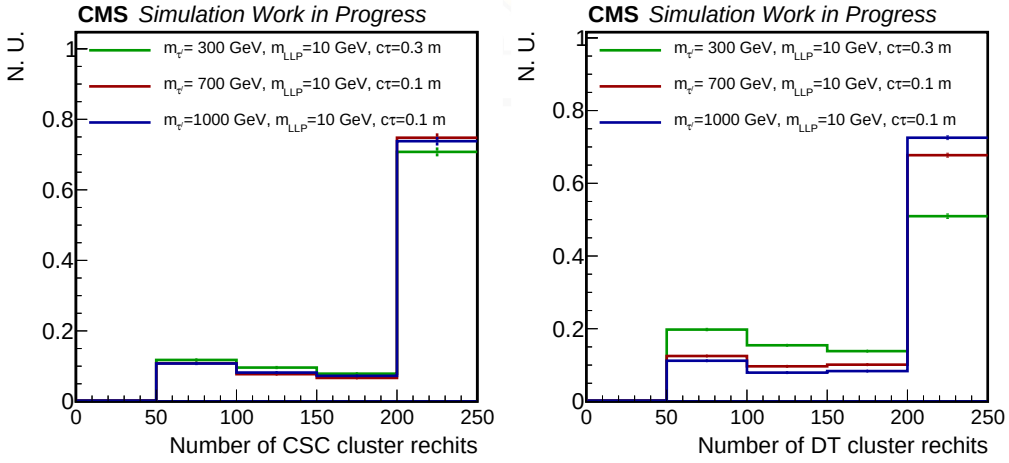

Figure 5.32: Number of RecHits in the cluster produced by the LLP decay within the CSC (left) and DT (right) geometric acceptance. Scenarios with VLL mass of 300 (green), 700 (red), and 1000 (blue) GeV are shown. The last histogram bin contains all overflow events.

To further guide the optimization of selection criteria and clustering algorithms, we characterize the spatial dependence of the cluster reconstruction efficiency. The following Figures 5.33, 5.34 and 5.35 show this efficiency as a function of the LLP decay location for several VLL mass hypotheses. The distributions are overlaid with the CMS muon system geometry to illustrate detector acceptance boundaries. Its efficiency is studied as a function of the LLP decay position (R and $|Z|$). This efficiency depends on the amount of material the decay products traverse before reaching the muon chambers, which influences the development of the particle shower.

More details about the clustering algorithm and its performance can be found in CMS internal analysis notes [66, 67].

5.4.3 Muon Reconstruction

Muons are reconstructed using information from both the silicon tracker and the muon subdetectors. To ensure reliable association with displaced showers, high-purity global muon identification is required, including hits in at least one muon station and a matched track in the inner tracker [68].

Muons must satisfy $p_T > 15$ GeV and $|\eta| < 2.4$, and be geometrically associated with a CSC or DT cluster within a cone of $\Delta R < 0.4$. This requirement reduces contamination from prompt or unrelated muons and defines orthogonal control regions.

The p_T and angular thresholds are optimized to maintain high efficiency for signal muons from τ decays while rejecting cosmic rays and misreconstructed tracks.

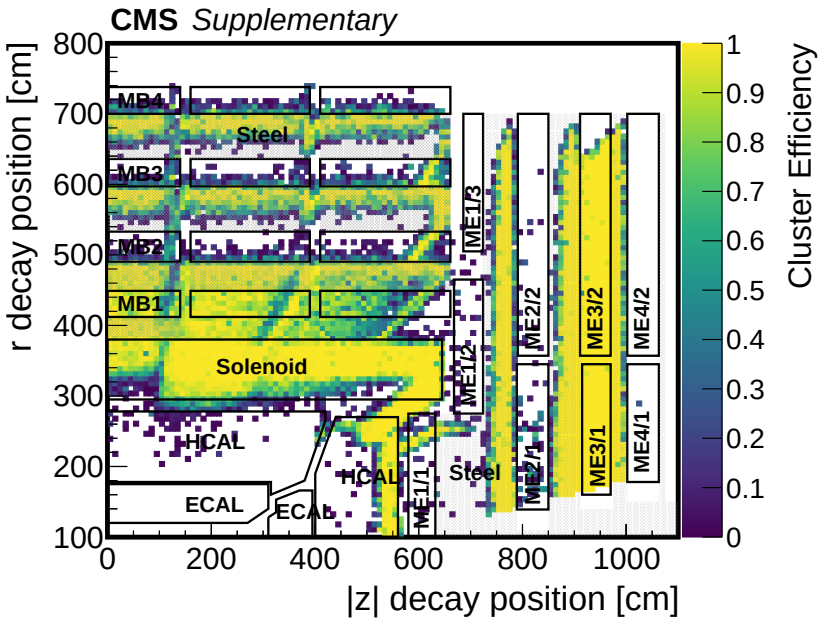

Figure 5.33: Cluster reconstruction efficiency as a function of the LLP decay position for a VLL mass of 300 GeV and a pseudoscalar boson mass of 2 GeV.

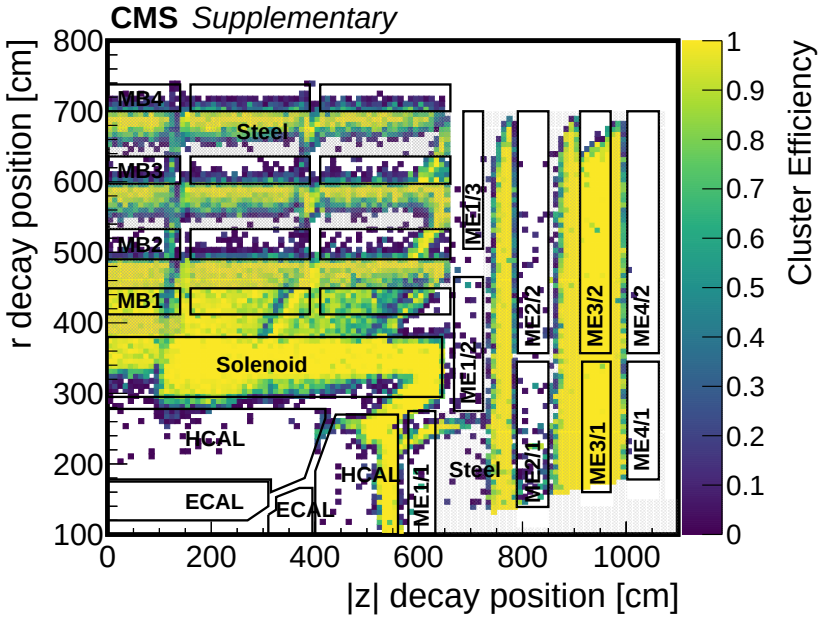

Figure 5.34: Cluster reconstruction efficiency as a function of the LLP decay position for a VLL mass of 500 GeV and a pseudoscalar boson mass of 2 GeV.

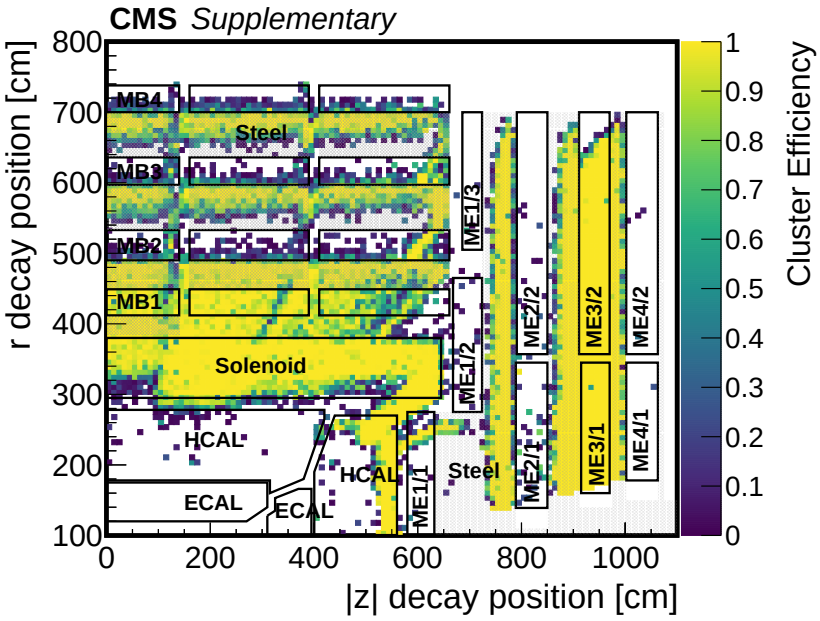

Figure 5.35: Cluster reconstruction efficiency as a function of the LLP decay position for a VLL mass of 700 GeV and a pseudoscalar boson mass of 2 GeV.

5.4.4 Jet Reconstruction

Jet reconstruction plays a supporting role in this analysis, primarily used to veto candidate clusters that may arise from hadronic activity mimicking an MDS. They are reconstructed using the Particle Flow (PF) algorithm [69], clustered with the anti-k_T algorithm [70] using a distance parameter of $R = 0.4$. Jet energy corrections (JEC) are applied according to the global tags listed in Table 5.4, consistent with the NanoAODv9 production [71].

PF jets with $p_T > 15$ GeV and $|\eta| < 3.0$ are used to veto clusters reconstructed in the DT and CSC subsystems [72]. This veto helps reduce contamination from hadronic activity that could mimic a displaced electromagnetic shower.

Table 5.4: Jet Energy Correction (JEC) global tags used for each data-taking period and simulation era in NanoAODv9 production.

Data 2016 BCD	Summer19UL16APV_RunBCD_V7_DATA
Data 2016 EF	Summer19UL16APV_RunEF_V7_DATA
Data 2016 FGH	Summer19UL16_RunFGH_V7_DATA
Data 2017 B	Summer19UL17_RunB_V5_DATA
Data 2017 C	Summer19UL17_RunC_V5_DATA
Data 2017 D	Summer19UL17_RunD_V5_DATA
Data 2017 E	Summer19UL17_RunE_V5_DATA
Data 2017 F	Summer19UL17_RunF_V5_DATA
Data 2018 A	Summer19UL18_RunA_V5_DATA
Data 2018 B	Summer19UL18_RunB_V5_DATA
Data 2018 C	Summer19UL18_RunC_V5_DATA
Data 2018 D	Summer19UL18_RunD_V5_DATA
MC 2016 APV	Summer19UL16APV_V7_MC
MC 2016	Summer19UL16_V7_MC
MC 2017	Summer19UL17_V5_MC
MC 2018	Summer19UL18_V5_MC

5.4.5 Tau Reconstruction

Hadronically decaying tau leptons (τ_h) are reconstructed using the DeepTau v2p1 algorithm [73], which employs a deep neural network to classify tau candidates against jets, electrons, and muons. Selected τ_h candidates are required to have $p_T > 30$ GeV, $|\eta| < 2.3$, and to fall into one-prong decay modes. Loose working point criteria are applied to maximize signal efficiency while suppressing background.

Tau candidates are used to define control regions and validate the reconstruction of displaced showers originating from $a_\tau \to \gamma\gamma$ decays in signal-like topologies. Additional isolation and decay mode discrimination variables are applied, including rejection against electrons and muons, following CMS standard recommendations [72, 74].

This reconstruction strategy ensures compatibility with CMS Run 2 object definitions and facilitates systematic uncertainty estimation based on well-established identification efficiencies.

5.4.6 Missing Transverse Momentum

The missing transverse momentum vector ($\vec{p_T}^{miss}$), or MET, is defined as the negative vector sum of the transverse momenta of all particle-flow (PF) candidates in the event [69, 75]. It serves as a key observable in searches for invisible or weakly interacting particles, such as neutrinos or long-lived particles (LLPs) decaying outside the calorimeters and tracker.

This analysis uses the Type-I corrected PF MET, where jet energy corrections are applied to the jets contributing to the MET calculation [71, 76]. An additional xy-shift correction is applied to reduce the ϕ modulation in the MET distribution. Although this correction significantly improves resolution at low MET, its effect is marginal (around 1%) for events with large MET, such as those passing the offline threshold of MET > 200 GeV used in this analysis.

During 2017 data-taking, excess ECAL Endcap (EE) noise was observed, which introduced anomalous jet activity and spurious MET. To mitigate this, a dedicated veto is applied to jets with raw $p_T < 50$ GeV in the forward region $2.65 < |\eta| < 3.139$, following the recommendations of [77]. This correction is applied consistently to both data and Monte Carlo (MC) events recorded under 2017 conditions.

To further suppress instrumental backgrounds such as beam halo, cosmic rays, and detector noise that can fake large MET, a set of event-level filters are applied. These filters, recommended by the CMS JETMET group [78], are listed in Table 5.5 and applied identically to both data and simulation. The efficiency of these filters on signal events exceeds 99%.

Table 5.5: MET filters used in data and MC.

Filter	Years Applied	Data	MC
Primary vertex filter	2016, 2017, 2018	Yes	Yes
Beam halo filter	2016, 2017, 2018	Yes	Yes
HBHE noise filter	2016, 2017, 2018	Yes	Yes
ECAL TP filter	2016, 2017, 2018	Yes	Yes
Bad PF Muon Filter	2016, 2017, 2018	Yes	Yes
Bad PF Muon Dz Filter	2016, 2017, 2018	Yes	Yes
EE badSC noise filter	2016, 2017, 2018	Yes	Yes
ECAL bad calibration filter	2017, 2018	Yes	Yes

5.4.7 Detector Effects During Run-2 Data-Taking

Although the Run-2 dataset used in this analysis underwent standard certification and quality monitoring procedures, several known detector issues were investigated to ensure they had negligible impact on signal modeling and event selection. The following subsections summarize these effects and the steps taken to evaluate them.

ECAL Endcap L1 Pre-firing (2016–2017): During the 2016 and 2017 data-taking periods, the ECAL endcap experienced L1 trigger pre-firing due to spurious early signals. This effect can lead to the loss of

events with high-p_T jets in the affected η range. Following the recommendations from the EXO pre-approval checklist [79], jets with $p_t > 100$ GeV and $2.25 < |\eta| < 3.0$ were removed from the simulated signal samples and the full analysis chain was re-run. The resulting change in the number of reconstructed muon showers was found to be below 1%, and thus no correction was applied.

HCAL Endcap (HEM15/16) Power Loss (2018): Two modules of the hadronic calorimeter (HEM15 and HEM16) were non-operational from Run 3109077 (late 2018B) until the end of data-taking. This affected the region $-3.0 < \eta < -1.3$ and $-1.57 < \phi < -0.87$. To quantify the effect, jets falling into this η–ϕ region were removed and signal selection distributions were re-evaluated. No significant impact on distributions or yields was observed (less than 1%), and no correction was deemed necessary.

Drift Tube (DT) Noise in 2016 Data: Localized noise in the DT system was observed in Station 2 (MB2), Wheel 1, ϕ sector 2 during a small subset of 2016 data (runs 275750 to 275950), corresponding to approximately 1.5 fb^{-1} of integrated luminosity. This noise could lead to the spurious reconstruction of muon clusters in the affected region. Following the recommendations in [80], clusters reconstructed in this specific region and run range were vetoed in the data. The effect was not present in signal simulations and was estimated to impact yields at the percent level; thus, no correction or veto was applied to simulated samples.

Overall, all investigated detector effects were found to have a negligible impact on the signal acceptance or background estimation. Therefore, no corrections or additional systematic uncertainties are applied in this analysis.

5.5 Event Selection and Analysis Strategy

This analysis targets events characterized by the presence of at least one muon detector shower (MDS) cluster and one hadronically decaying tau lepton (τ_h), as expected in signal scenarios involving long-lived pseudoscalars (a_τ) produced from vector-like lepton (VLL) decays. The CSC system comprises a total of 18 rings (ME±1/1, ME±1/2, ME±1/3, ME±2/1, ME±2/2, ME±3/1, ME±3/2, ME±4/1, ME±4/2), while the DT system consists of five wheels (MB0, MB±1, MB±2), each segmented into four layers, for a total of 20 rings.

The main backgrounds for such events include punch-through jets, muon bremsstrahlung, cosmic ray muons, detector noise, and pileup. Standard Model (SM) processes such as multijet, W+jets, and $\bar{t}t$ production also contribute to backgrounds for hadronic taus, both real and fake.

Events must satisfy the high-level MET-based trigger conditions described in Section 5.3, along with an offline MET requirement of $p_T^{\text{miss}} > 200$ GeV. Quality filters listed in Section 5.4.6 are applied to reject spurious MET from beam halo, detector noise, and misreconstructed objects. In addition, events with more than 10 muon detector rings (either CSC or DT) containing at least 50 RecHits are vetoed to suppress cosmic ray showers [81].

Signal candidates must contain at least one CSC or DT cluster with more than 50 RecHits, and at least one hadronic tau candidate passing the identification and kinematic requirements detailed in Section 5.4.5. The τ_h selection efficiency ranges from 70% to 88% depending on the signal hypothesis, with approximately 99% background rejection. The number of RecHits in the selected cluster (N_{RecHits}) serves as the primary observable for signal extraction. Backgrounds are estimated using a data-driven "alphabet" method, in which a control region is defined by inverting the τ_h selection and fitting a parametric model to extrapolate into the signal region, as detailed in Section 5.6.

Shower clusters are categorized as CSC or DT based on their reconstruction subsystem. For CSC clusters, the selection includes geometric vetoes against nearby jets and muons, exclusion of sensitive regions with minimal shielding, and timing-based criteria to reject out-of-time backgrounds. Similarly, DT cluster selections adapt to the barrel geometry and cosmic muon patterns. Additional discrimination is achieved using the angular separation $\Delta\phi(\vec{p}_T^{\,\text{miss}}, \text{cluster})$, which is small for signal and flat for background, in combination with N_{RecHits}. These variables are used in a two-dimensional control method for background validation in Section 5.6.

5.5.1 CSC Cluster Selections

To reject CSC clusters produced by punch-through jets and muon bremsstrahlung, clusters are vetoed if geometrically matched within $\Delta R < 0.4$ to any jet (muon) with $p_T > 15$ GeV and $|\eta| < 3.0$ ($|\eta| < 2.4$). No object identification is required for these vetoes. These selections yield a signal efficiency above 87% (jets) and 99% (muons), depending on the signal hypothesis. The inefficiency is primarily driven by accidental overlaps with pileup jets [80].

Additional vetoes are applied to reject clusters from punch-through jets and bremsstrahlung not associated with reconstructed objects. Clusters with RecHits in the ME1/1 region are rejected due to low shielding. Clusters matched to DT segments or RPC hits in the MB1 station are also vetoed to remove showers from muons traversing $0.8 < |\eta| < 1.2$. A requirement of $|\eta| < 2.2$ is applied to ensure well-contained showers. ME1/2 and RE1/2 vetoes used in earlier analyses are not applied here. While previous studies included a ClusterID discriminator, it was found suboptimal for $a_\tau \to \gamma\gamma$ decays and is not used.

The cluster time spread is defined as:

$$t_{\text{spread}} = \sqrt{\frac{1}{N}\sum_i (t_i - \bar{t})^2},$$

where t_i are strip digi times of individual RecHits and $\bar{t}$ their mean. A requirement of $t_{\text{spread}} < 20$ ns is applied to reject clusters composed of RecHits from multiple bunch crossings, with over 98% signal efficiency.

The cluster time (t_{cluster}) is defined as the weighted mean of wire and strip digi times of all RecHits. Figure 5.36 (left) shows the t_{cluster} distribution, where signal peaks near zero, and out-of-time pileup dominates the tails. The in-time region is defined as $-5.0 < t_{\text{cluster}} < 12.5$ ns, removing pileup-induced clusters with over 98% signal retention. An early out-of-time control region is defined by $t_{\text{cluster}} < -12.5$ ns.

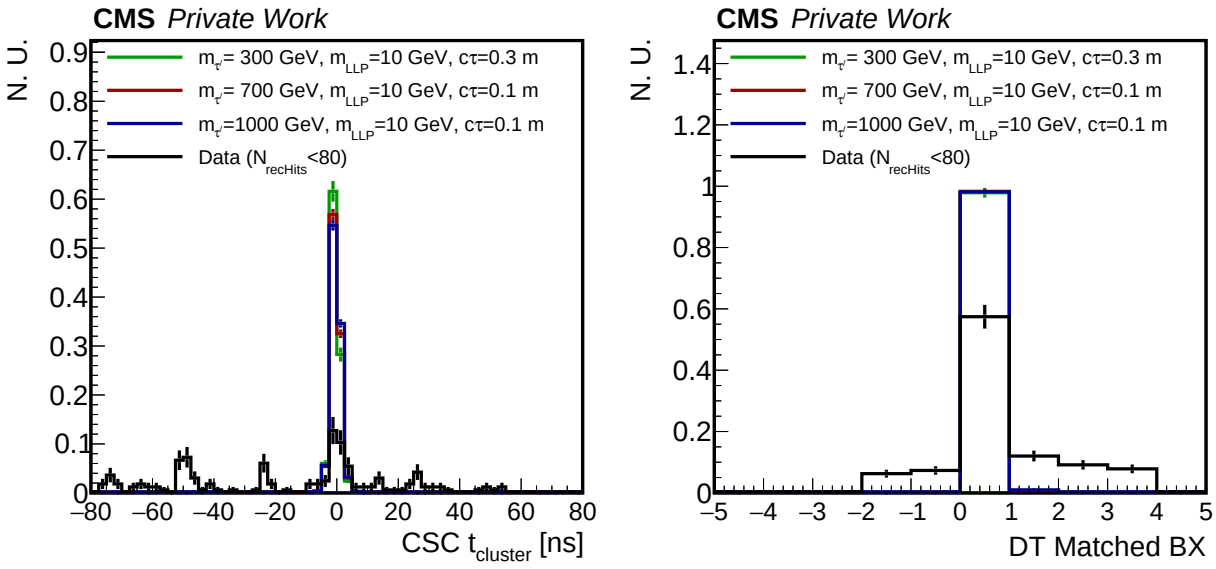

Figure 5.36: Distribution of cluster time of the selected CSC (left) and DT (right) clusters in signal and data ($N_{\text{RecHits}} < 80$). All other selections are applied.

Selection efficiencies in Run-2 data and signal simulation for different mass hypotheses are presented in Tables 5.6–5.9.

5.5.2 DT Cluster Selections

DT cluster selection applies a similar rejection strategy, adapted to the DT geometry and characteristic cosmic muon backgrounds. Clusters are rejected if geometrically matched within $\Delta R < 0.4$ to any jet or muon with $p_T > 15$ GeV and $|\eta| < 3.0$ ($|\eta| < 2.4$ for muons). To suppress cosmic ray muons that produce large showers

Selection	cut eff.	cumulative eff.	Number of events
MET filters	94.39	94.39174	10291184.0
CSC+DT rings ≤ 10	100.00	94.39112	10291116.0
$N^{CSC}_{clusters} \geq 1$	5.89	5.56112	606308.0
$N_{\tau_h} \geq 1$	1.96	0.10873	11854.0
Muon Veto	68.73	0.07473	8147.0
Jet Veto	66.01	0.04933	5378.0
Chamber Vetos	10.88	0.00537	585.0
Cluster $\lvert\eta\rvert < 2.2$	72.99	0.00392	427.0
Time spread	72.37	0.00283	309.0
Cluster Time	33.01	0.00094	102.0

Table 5.6: Efficiency(%) of each CSC selection for the full Run-2 dataset. The cumulative efficiency is calculated with respect to events passing the Trigger and MET cuts. The cut efficiency is calculated with respect to the previous cut.

	$c\tau = 0.3$m		$c\tau = 1.0$m	
Selection	cut eff.	cumulative eff.	cut eff.	cumulative eff.
Acceptance	28.52	28.52	17.76	17.76
MET Trigger and MET>200 GeV	11.53	3.29	12.33	2.18
MET filters	98.90	98.90	99.41	99.41
CSC+DT rings ≤ 10	100.00	98.90	100.00	99.41
$N^{CSC}_{clusters} \geq 1$	32.75	32.39	29.60	29.42
$N_{\tau_h} \geq 1$	69.23	22.42	72.91	21.45
Muon Veto	99.27	22.26	99.52	21.35
Jet Veto	90.17	20.07	92.43	19.73
Chamber Vetos	67.10	13.46	69.60	13.73
Cluster $\lvert\eta\rvert < 2.2$	96.99	13.06	97.61	13.41
Time spread	97.94	12.79	98.73	13.24
Cluster Time	98.50	12.60	99.50	13.16

Table 5.7: Signal efficiency(%) of each CSC selection for the VLL mass of 300 GeV (LLP mass of 10 GeV). The cumulative efficiency is calculated with respect to events in acceptance passing the Trigger and MET cuts. The cut efficiency is calculated with respect to the previous cut. Acceptance is defined as when at least one LLP decays inside CSC.

	$c\tau = 0.1$m		$c\tau = 1.0$m	
Selection	cut eff.	cumulative eff.	cut eff.	cumulative eff.
Acceptance	29.08	29.08	10.11	10.11
MET Trigger and MET>200 GeV	52.19	15.18	51.66	5.22
MET filters	98.70	98.70	99.48	99.48
CSC+DT rings ≤ 10	100.00	98.70	100.00	99.48
$N^{CSC}_{clusters} \geq 1$	34.53	34.09	30.92	30.76
$N_{\tau_h} \geq 1$	84.42	28.77	91.42	28.12
Muon Veto	99.21	28.54	99.53	27.99
Jet Veto	87.09	24.86	89.38	25.01
Chamber Vetos	62.70	15.59	71.29	17.83
Cluster $\|\eta\| < 2.2$	97.69	15.22	98.18	17.50
Time spread	98.53	15.00	98.35	17.21
Cluster Time	97.70	14.66	99.41	17.11

Table 5.8: Signal efficiency(%) of each CSC selection for the VLL mass of 700 GeV (LLP mass of 10 GeV). The cumulative efficiency is calculated with respect to events in acceptance passing the Trigger and MET cuts. The cut efficiency is calculated with respect to the previous cut. Acceptance is defined as when at least one LLP decays inside CSC.

	$c\tau = 0.1$m		$c\tau = 1.0$m	
Selection	cut eff.	cumulative eff.	cut eff.	cumulative eff.
Acceptance	28.54	28.53	7.73	7.73
MET Trigger and MET>200 GeV	64.74	18.49	64.62	4.99
MET filters	98.53	98.53	99.01	99.00
CSC+DT rings ≤ 10	100.00	98.53	100.00	99.00
$N^{CSC}_{clusters} \geq 1$	35.14	34.63	32.73	32.40
$N_{\tau_h} \geq 1$	88.02	30.47	90.09	29.19
Muon Veto	99.32	30.27	98.85	28.86
Jet Veto	86.29	26.11	89.25	25.76
Chamber Vetos	61.30	16.00	67.17	17.30
Cluster $\|\eta\| < 2.2$	98.25	15.73	98.26	17.00
Time spread	98.30	15.46	97.40	16.56
Cluster Time	98.16	15.18	97.34	16.12

Table 5.9: Signal efficiency(%) of each CSC selection for the VLL mass of 1000 GeV (LLP mass of 10 GeV). The cumulative efficiency is calculated with respect to events in acceptance passing the Trigger and MET cuts. The cut efficiency is calculated with respect to the previous cut. Acceptance is defined as when at least one LLP decays inside CSC.

across adjacent wheels, clusters are vetoed if more than 8 MB1 hits are found in adjacent wheels within $\Delta\phi < \pi/4$.

A matched RPC hit is required in the same wheel within $\Delta\phi < 0.5$ to validate the timing. The DT cluster time is assigned based on the most frequently occurring bunch crossing (BX) among the matched RPC hits. Only clusters with BX = 0 are retained in the signal region to ensure consistency with the primary interaction timing. The corresponding distribution of t_{cluster} is shown in Figure 5.36 (right). The DT selection efficiencies for data and signal samples with varying LLP lifetimes and VLL masses are reported in Tables 5.10–5.13.

Selection	cut eff.	cumulative eff.	Number of events
MET filters	94.39	94.39174	10291184.0
CSC+DT rings ≤ 10	100.00	94.39112	10291116.0
$N^{DT}_{clusters} \geq 1$	4.83	4.55876	496725.0
$N_{\tau_h} \geq 1$	2.61	0.11915	12990.0
Muon Veto	24.92	0.02969	3237.0
Jet Veto	27.03	0.00803	875.0
MB1 Adjacent	83.89	0.00673	734.0
RPC Matching	84.74	0.00571	622.0
Cluster Time	57.72	0.00329	359.0

Table 5.10: Efficiency(%) of each DT selection for the full Run-2 dataset. The cumulative efficiency is calculated with respect to events passing the Trigger and MET cuts. The cut efficiency is calculated with respect to the previous cut.

	$c\tau = 0.3$m		$c\tau = 1.0$m	
Selection	cut eff.	cumulative eff.	cut eff.	cumulative eff.
Acceptance	46.02	46.02	30.82	30.82
MET Trigger and MET>200 GeV	11.82	5.43	12.01	3.70
MET filters	99.63	99.63	99.77	99.77
CSC+DT rings ≤ 10	100.00	99.63	100.00	99.77
$N^{DT}_{clusters} \geq 1$	39.41	39.27	33.90	33.82
$N_{\tau_h} \geq 1$	75.85	29.78	77.91	26.35
Muon Veto	99.33	29.58	99.54	26.22
Jet Veto	91.54	27.08	91.69	24.05
MB1 Adjacent	87.88	23.79	90.60	21.79
RPC Matching	99.03	23.56	98.39	21.44
Cluster Time	98.16	23.13	97.70	20.94

Table 5.11: Signal efficiency(%) of each DT selection for the VLL mass of 300 GeV (LLP mass of 10 GeV). The cumulative efficiency is calculated with respect to events in acceptance passing the Trigger and MET cuts. The cut efficiency is calculated with respect to the previous cut. Acceptance is defined as when at least one LLP decays inside DT.

5.6 Background Modeling

This analysis uses a fully data-driven strategy to model backgrounds from standard-model processes mimicking displaced showers in the muon system. The discriminant variable is the number of RecHits in the selected cluster (N_{RecHits}), which is expected to be significantly higher for signal-like showers than for backgrounds.

To estimate backgrounds in the signal region (SR), defined as the in-time window with all nominal selections applied, we implement a parametric "alphabet" method. This technique utilizes control regions defined by inverting the hadronic tau identification to model the fake rate transfer factor from background-dominated (Fail) to signal-enriched (Pass) regions. The transfer factor is parametrized as a function of N_{RecHits} and is fitted simultaneously to the Pass and Fail regions.

	$c\tau = 0.1$m		$c\tau = 1.0$m	
Selection	cut eff.	cumulative eff.	cut eff.	cumulative eff.
Acceptance	60.72	60.72	21.15	21.15
MET Trigger and MET>200 GeV	53.19	32.30	52.89	11.18
MET filters	99.37	99.37	99.59	99.59
CSC+DT rings ≤ 10	100.00	99.37	100.00	99.59
$N^{DT}_{clusters} \geq 1$	47.60	47.29	41.40	41.23
$N_{\tau_h} \geq 1$	85.63	40.49	88.36	36.43
Muon Veto	98.97	40.08	98.92	36.04
Jet Veto	87.03	34.88	90.22	32.51
MB1 Adjacent	86.22	29.72	88.88	28.89
RPC Matching	98.84	29.38	98.67	28.51
Cluster Time	98.58	28.96	98.54	28.09

Table 5.12: Signal efficiency(%) of each DT selection for the VLL mass of 700 GeV (LLP mass of 10 GeV). The cumulative efficiency is calculated with respect to events in acceptance passing the Trigger and MET cuts. The cut efficiency is calculated with respect to the previous cut. Acceptance is defined as when at least one LLP decays inside DT.

	$c\tau = 0.1$m		$c\tau = 1.0$m	
Selection	cut eff.	cumulative eff.	cut eff.	cumulative eff.
Acceptance	64.17	64.17	16.77	16.78
MET Trigger and MET>200 GeV	65.87	42.26	65.69	11.01
MET filters	99.22	99.22	99.48	99.46
CSC+DT rings ≤ 10	100.00	99.22	100.00	99.46
$N^{DT}_{clusters} \geq 1$	50.35	49.95	43.63	43.40
$N_{\tau_h} \geq 1$	88.21	44.06	88.40	38.36
Muon Veto	98.60	43.44	98.27	37.69
Jet Veto	86.77	37.69	88.48	33.35
MB1 Adjacent	85.99	32.41	87.60	29.21
RPC Matching	98.75	32.01	98.76	28.85
Cluster Time	98.43	31.50	97.66	28.18

Table 5.13: Signal efficiency(%) of each DT selection for the VLL mass of 1000 GeV (LLP mass of 10 GeV). The cumulative efficiency is calculated with respect to events in acceptance passing the Trigger and MET cuts. The cut efficiency is calculated with respect to the previous cut. Acceptance is defined as when at least one LLP decays inside DT.

5.6.1 Data-driven Background Model

The background estimation in this analysis is fully data-driven and based on a parametric "alphabet" method. This technique is illustrated in Figure 5.37, where events are divided into a signal-enriched “Pass” region and a background-dominated “Fail” region. The Pass region includes events satisfying the nominal DeepTau identification for at least one τ_h candidate, while the Fail region is defined by requiring the presence of at least one τ_h candidate that fails the VVLoose working point. This inversion suppresses signal contamination by a factor of approximately 9, while maintaining statistical power and preserving the shape of the background N_{RecHits} distribution.

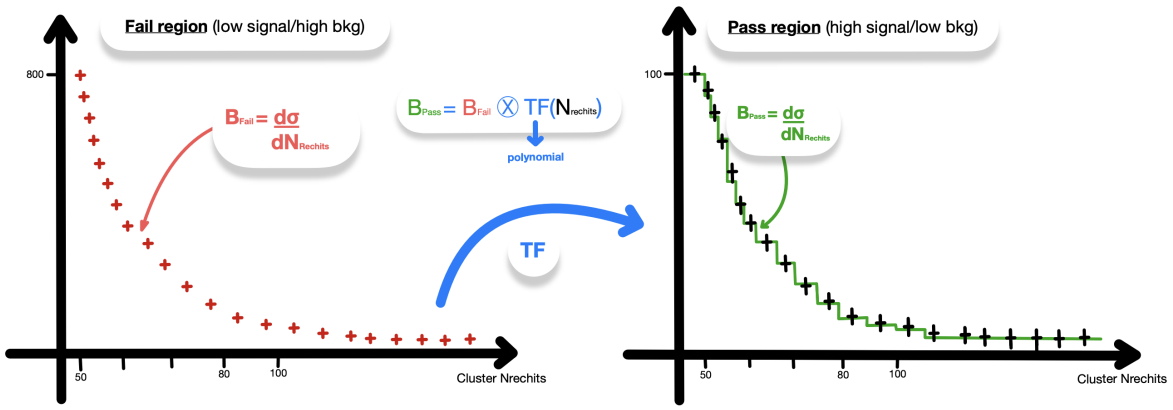

Figure 5.37: Sketch of the parametric alphabet method.

A transfer factor, defined as a function of the number of RecHits (N_{RecHits}), is used to extrapolate the background yield from the Fail to the Pass region. This transfer factor is modeled as a polynomial, and its order is selected using a statistically robust iterative procedure. The methodology is as follows:

1. Start with the simplest polynomial model, denoted p_1 (in this case, a zeroth-order polynomial or constant).
2. Fit p_1 to the data in the Fail and Pass regions and generate toy Monte Carlo datasets using the best-fit parameters.
3. Define a higher-order model p_2 with one additional polynomial term.
4. Fit both p_1 and p_2 to the data and toys, and compute the F-test statistic (Eq. 5.23) and the GoF statistic for p_1.
5. If both the F-test p-value (model comparison) and GoF p-value (absolute fit quality) are ≥ 0.05, model p_1 is accepted as sufficient.
6. If not, repeat the procedure with p_2 as the new baseline.

$$F = \frac{\frac{-2\log\lambda_1 + 2\log\lambda_2}{p_2 - p_1}}{\frac{-2\log\lambda_1}{n_{\text{bins}} - p_2}} \tag{5.23}$$

This data-driven method balances model simplicity and statistical robustness. For both CSC and DT categories, statistical tests confirm that a constant transfer factor (pol-0) provides sufficient modeling power. This choice minimizes overfitting while capturing the essential behavior of the background distribution. This conclusion is supported by high p-values from both the F-test and GoF tests, as shown in Figure 5.38 and summarized in Table 5.14.

The fitted background distributions in the in-time signal region (low N_{RecHits}) for the CSC and DT categories are shown in Figure 5.39, and demonstrate excellent agreement with the observed data.

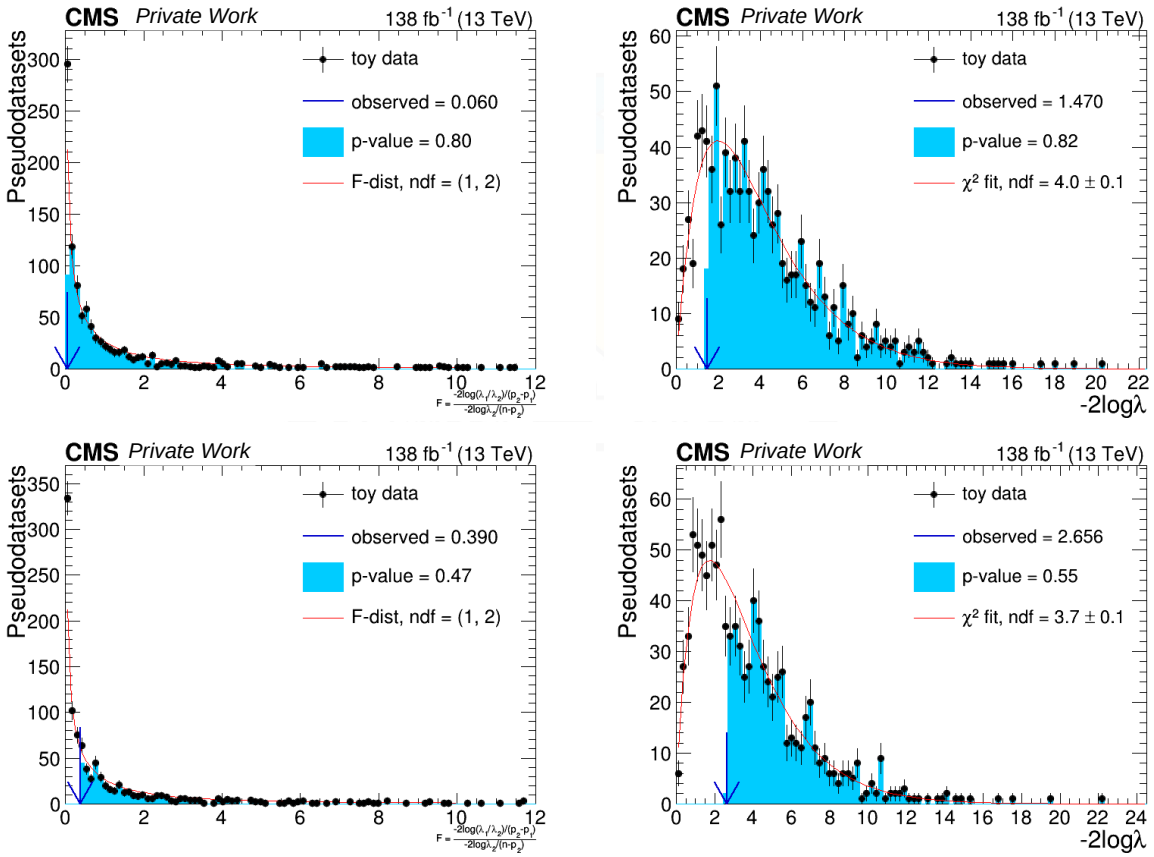

Figure 5.38: F-test (left) and GoF (right) results in the in-time signal region for CSC (top) and DT (bottom) categories.

Table 5.14: Statistical test results for model selection in different regions.

Region	F-test p-value	GoF p-value	Selected Model
CSC In-time (SR)	0.80	0.82	pol-0
DT In-time (SR)	0.47	0.55	pol-0
CSC OOT	0.71	0.61	pol-0
DT OOT	0.97	0.87	pol-0

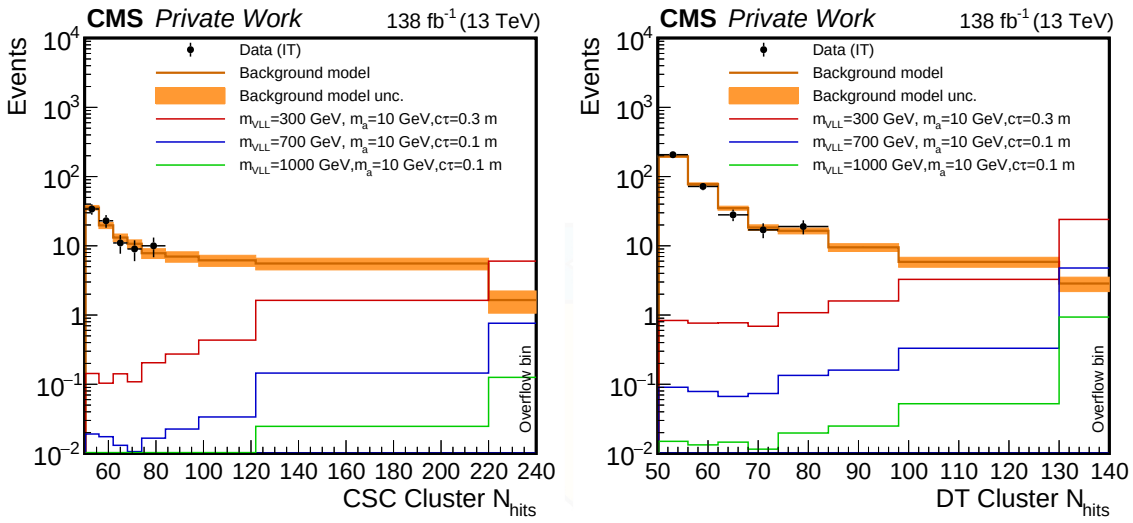

Figure 5.39: Signal, background model, and data (low N_{RecHits}) distributions in the in-time signal region for the CSC (left) and DT (right) categories.

5.6.2 Out-of-time Validation

To validate the background model, an out-of-time (OOT) control region is defined by requiring $t_{\text{cluster}} < -12.5$ ns for CSC and $t^{DT}_{\text{cluster}} < 0$ for DT clusters. The same transfer factor fitting procedure is applied. The corresponding statistical tests confirm that a constant model (pol-0) provides an adequate description, as shown in Figure 5.40.

The OOT N_{RecHits} distributions are shown in Figure 5.41.

5.6.3 Bias Studies

To verify the robustness of the background model, pseudo-experiments are performed using toy datasets with injected signal strengths $\mu_{inj} = 1, 2, 3$. The fitted signal strength μ_{fit} is compared to the injected value, and the bias is computed as:

$$\text{bias}(\mu_{fit}, \mu_{inj}, \sigma_\mu) = \frac{\mu_{fit} - \mu_{inj}}{\sigma_\mu} \tag{5.24}$$

where σ_μ is the uncertainty on the fitted signal strength. For an unbiased estimator, the distribution of bias should be a Gaussian centered at zero with a width of one. The distributions of bias for the pol-0 and pol-1 models are shown in Figure 5.42. The means of the distributions are all consistent with zero, confirming that the chosen background model is unbiased.

5.6.4 Unblinded Background Model

After validating the background estimation strategy in control regions, the method is applied to the full dataset, including the high-N_{RecHits} signal region (SR) which was previously blinded. This unblinding is the final step to determine the background estimate and compare it with the observed data.

As shown in Fig. 5.43, the data in the SR are found to be in good agreement with the background-only prediction. No significant excess of events is observed in the high-N_{RecHits} region, where a signal from VLL decays would be expected to appear.

To confirm the validity of the model across the full range, the statistical tests were re-evaluated after unblinding. The results, shown in Fig. 5.44, confirm that the constant transfer factor (pol-0) remains a valid and robust choice for describing the background, with high p-values obtained from both the F-test and the Goodness-of-Fit test.

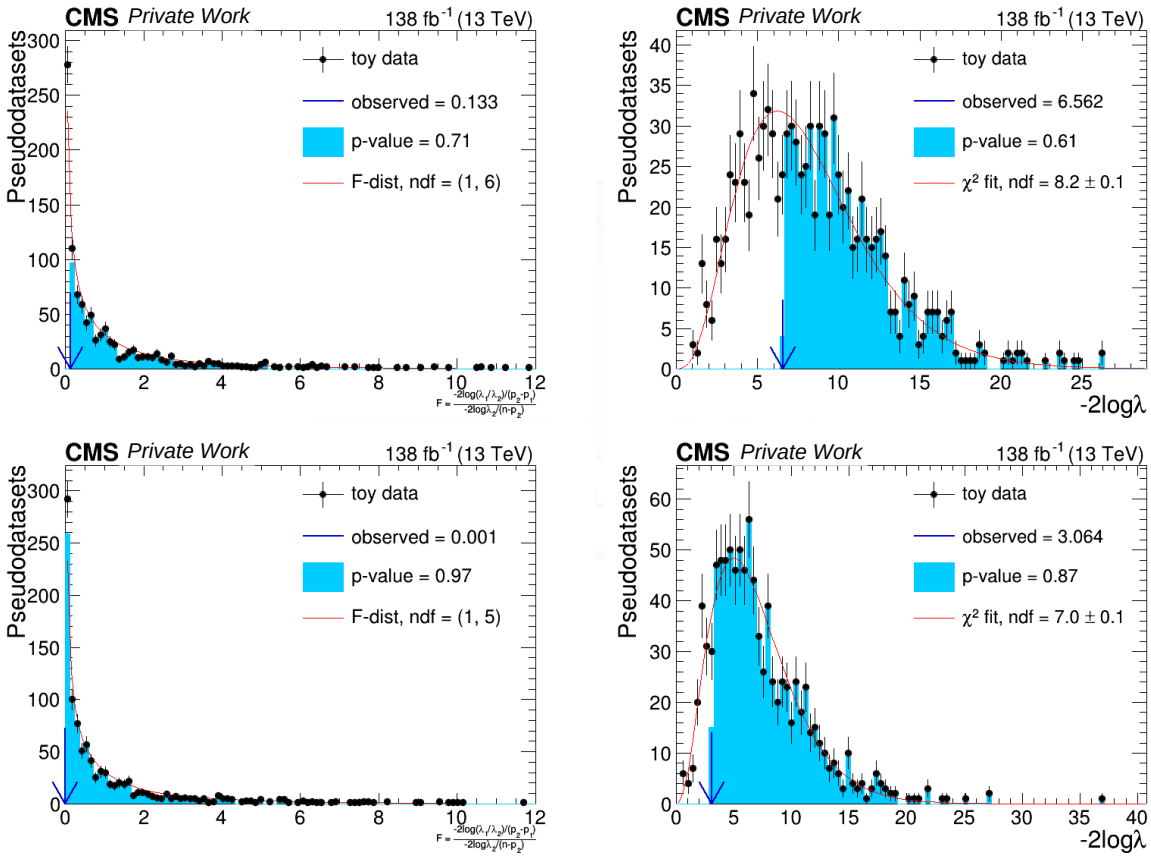

Figure 5.40: F-test (left) and GoF (right) results in the OOT regions for CSC (top) and DT (bottom).

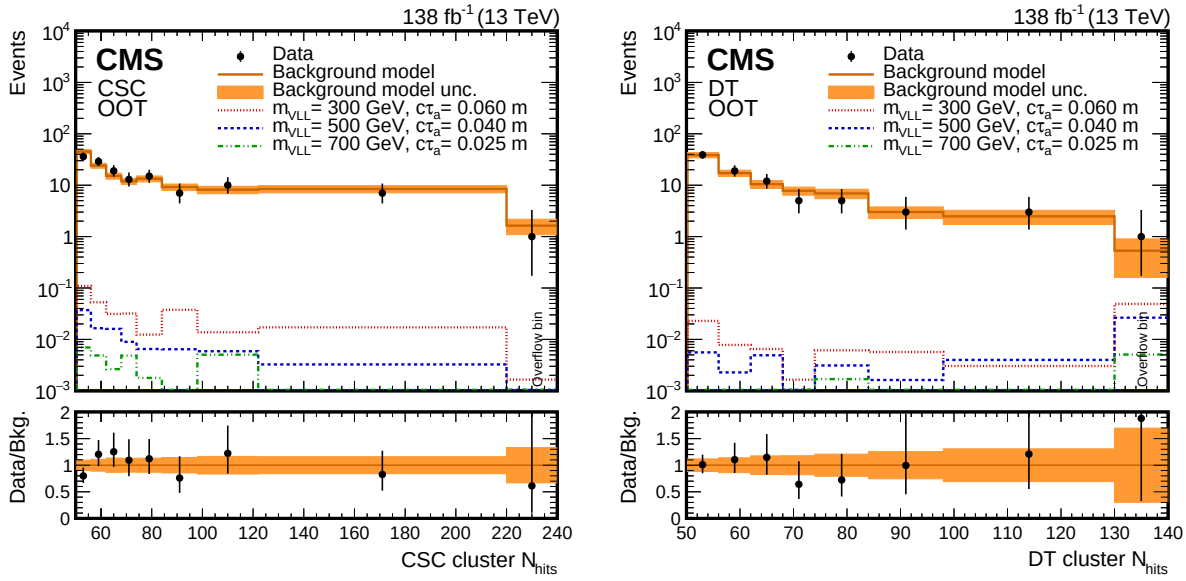

Figure 5.41: OOT validation: N_{RecHits} distributions for CSC (left) and DT (right). Data, background model, and signal hypotheses are shown.

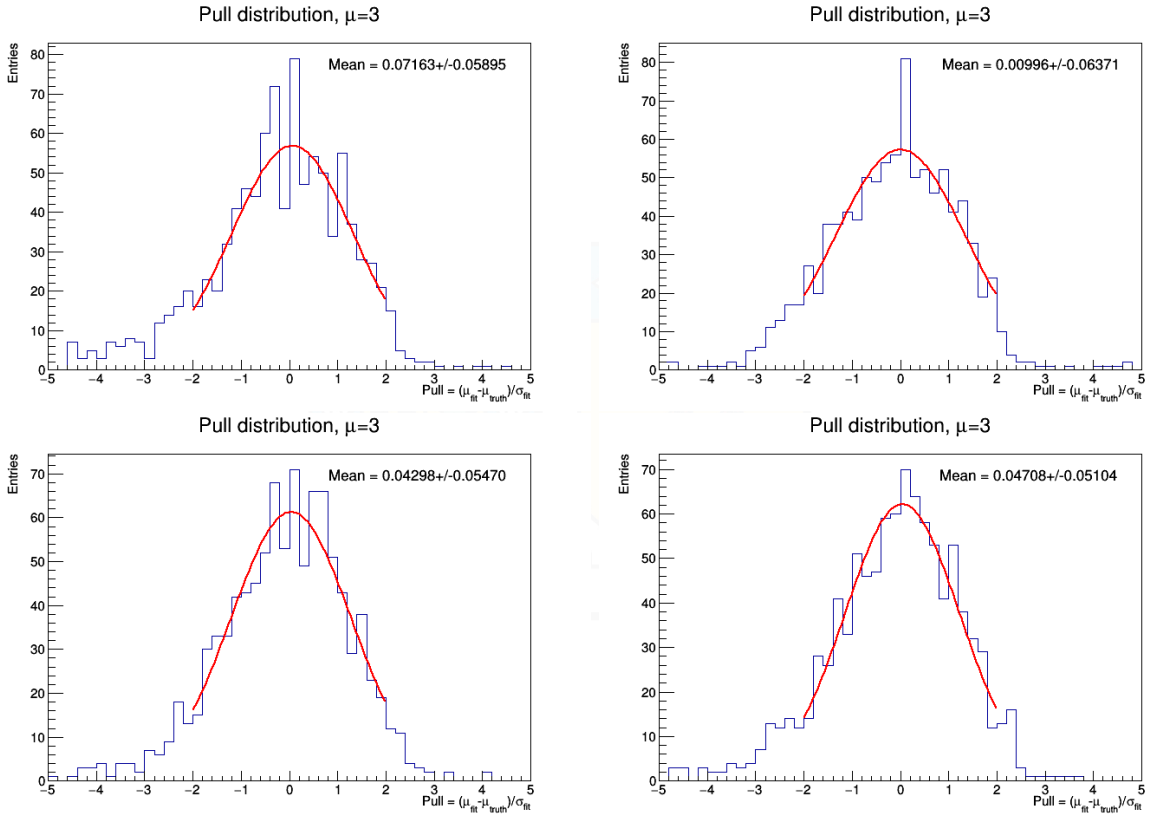

Figure 5.42: Bias on μ_{fit} for CSC (top) and DT (bottom) for pol-0 (left) and pol-1 (right) models.

With the background model validated and applied to the full dataset, the final distributions are used to set upper limits on the signal production cross section, as will be detailed in Section 5.8.

5.7 Systematic Uncertainties

The precision of the search results is influenced by various sources of systematic uncertainty. These uncertainties can affect the normalization and shape of both the signal and background predictions, and must be properly accounted for when interpreting the final outcome. In the statistical analysis, these effects are modeled as "nuisance parameters", each constrained by a probability density function, allowing their impact on the signal strength to be profiled in the final fit.

The following sections detail the main sources of systematic uncertainty considered in this analysis, which are grouped into two primary categories: those affecting the data-driven background model and those related to the modeling of the signal simulation. Finally, the post-fit impact of each uncertainty on the result is presented.

5.7.1 Background Model Uncertainties

Since the background is estimated entirely from data using the alphabet method, the associated uncertainties are not derived from theoretical cross section calculations but rather from the statistical power and the assumptions of the method itself. Two main categories of uncertainty are considered:

- **Statistical Uncertainty:** The limited number of events in the control regions, particularly in the ‘Fail‘ region used to derive the transfer factor, introduces a statistical uncertainty on the final background prediction in the signal region. This uncertainty is propagated through the fit by the alphabet method.
- **Transfer Factor (TF) Model Uncertainty:** A systematic uncertainty is assigned to account for the choice of the functional form of the transfer factor. The nominal background estimate is derived using a

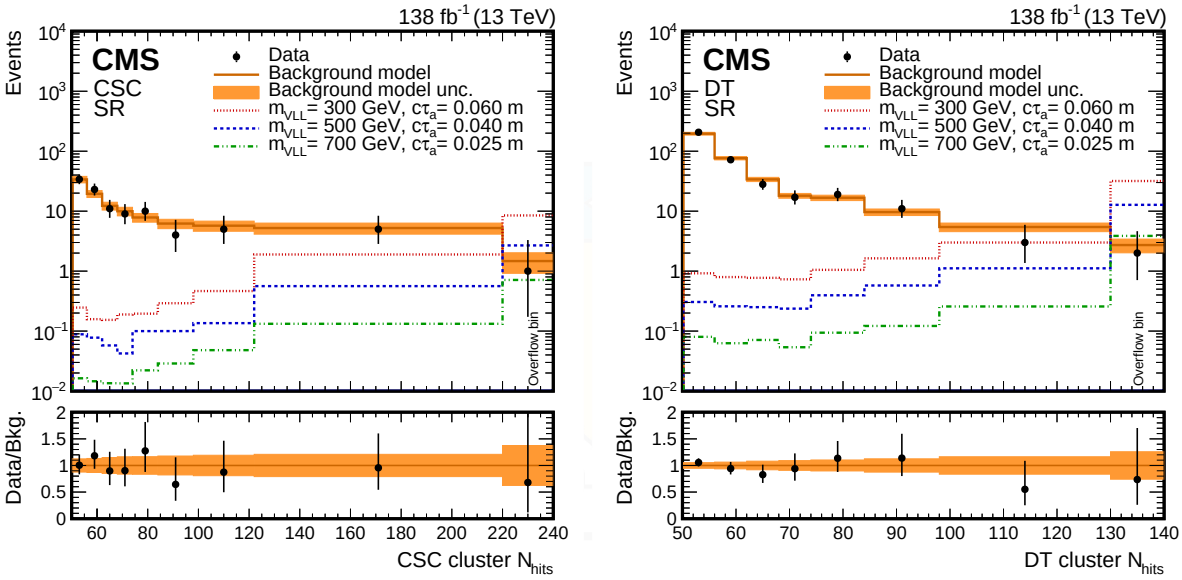

Figure 5.43: Final N_{RecHits} distributions in SR for CSC (left) and DT (right).

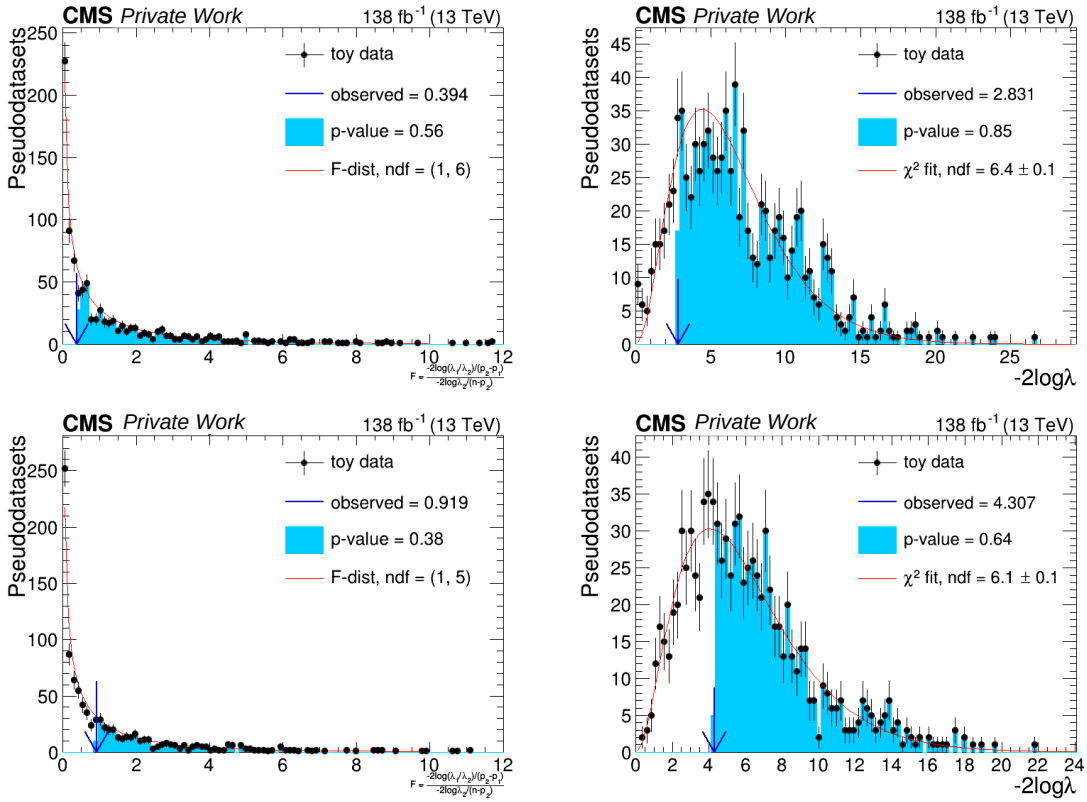

Figure 5.44: F-test and GoF results in unblinded SR for CSC (top) and DT (bottom).

zeroth-order polynomial (a constant TF). This uncertainty is evaluated by taking the difference in the background prediction when using an alternative first-order polynomial. This difference is then applied as a shape-based uncertainty on the nominal background template.

5.7.2 Signal Modeling Uncertainties

The expected signal yield is affected by several sources of systematic uncertainty, related to the detector simulation, object reconstruction, and theoretical modeling. The main sources are:

- **Luminosity:** This uncertainty affects the overall normalization of the signal yield. It is estimated to be 1.6% for the combined 2016–2018 dataset [38] and is treated as correlated across all years.
- **Pile-up reweighting:** The uncertainty on the modeling of pileup affects the simulation's kinematic distributions. It is estimated by varying the total inelastic proton-proton cross section by 4.6% from its nominal value [6].
- **Trigger efficiency:** The efficiency of the HLT paths is measured in data and applied as a scale factor to the simulation. The uncertainty on this scale factor, typically around 2%, is assigned as a systematic uncertainty on the signal yield [6].
- **Jet energy scale (JES) and resolution (JER):** Uncertainties on JES and JER are propagated to the calculation of missing transverse energy. This affects the signal acceptance due to the $p_T^{miss} > 200$ GeV requirement. The impact is found to be small, typically below 1%. These uncertainties are derived from dedicated studies of jet performance [82].
- **CSC chamber readout:** A 2% inefficiency is applied to CSC readout chambers in the simulation to account for known dead channels not modeled by default. The uncertainty associated with this correction is taken as a systematic [66].
- **Cluster reconstruction efficiency:** This is a dominant uncertainty for this analysis. Since there is no standard candle for MDS signatures in data, the efficiency is estimated using simulated photon showers that are smeared to match the resolution observed in data. A conservative uncertainty of 20% is assigned to this efficiency to cover potential differences between data and simulation [66].
- **Veto efficiencies (Muon, Jet, Chamber):** The efficiencies of the various vetoes used to reject backgrounds have associated uncertainties. These are estimated to be less than 1% for the muon veto, 3% per jet for the jet veto, and a conservative 10% for the chamber-based vetoes, such as the ME1/1 veto [66].
- **Cluster Time:** The uncertainty on the cluster timing selection is evaluated by shifting the timing window of the in-time region by ± 2.5 ns in the simulation and taking the resulting change in signal acceptance as the systematic uncertainty [66].
- **Tau ID efficiency and energy scale:** An uncertainty of 5% is applied for the tau identification efficiency for each hadronically decaying tau. The uncertainty on the tau energy scale (TES) is also considered, as it can affect the kinematics and thus the efficiency of other selections [56].

5.7.3 Unblinded systematic impacts

To assess the significance of each source of uncertainty on the final result, a maximum likelihood fit is performed on the data, combining all signal and control regions. The impacts of the individual nuisance parameters on the best-fit signal-strength modifier, μ, are shown in Figure 5.45. The plot ranks the nuisance parameters by their post-fit impact on μ, separating the effects of statistical and systematic uncertainties.

The analysis is found to be predominantly limited by the statistical uncertainty of the data-driven background estimate.This is common in searches for rare processes that rely on control regions with a limited number of events, and in this case, the largest impacts arise from the limited number of events in the 'Fail' control regions of the alphabet method, particularly for the CSC category (`stat_fail_csc`).

Among the systematic uncertainties, the dominant sources are:

- The 20% uncertainty assigned to the **cluster reconstruction efficiency** (`eff_cluster`), which has the largest impact on the signal normalization.

- The uncertainty on the choice of the **background model's transfer factor** (`TF_model`), which affects the background prediction.
- The uncertainty on the **trigger efficiency** scale factors (`eff_trig`).
- The uncertainty on the integrated **luminosity** (`lumi`).

The right side of Figure 5.45 shows the post-fit values of the nuisance parameters (the "pulls"). All parameters are observed to be consistent with their pre-fit expectation of zero within their uncertainties, which indicates a good and stable fit.

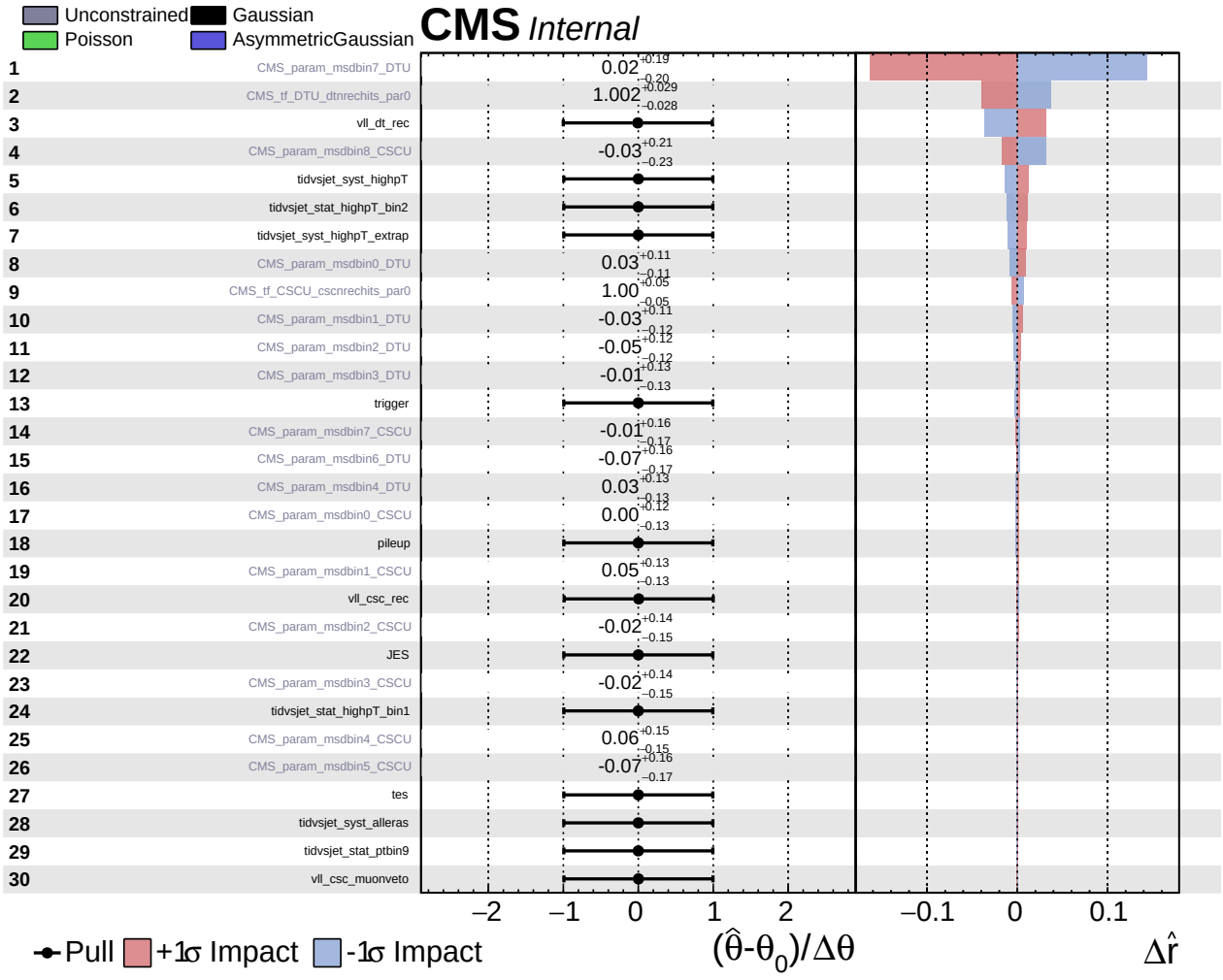

Figure 5.45: Unblinded systematic uncertainty impacts. The signal hypothesis corresponds to a VLL mass = 700 GeV, LLP mass = 10 GeV, and $a_{c\tau} = 0.1$ m.

5.8 Results

Since no significant excess of events is observed in data above the background-only prediction detailed in Section 5.6, the results of the search are interpreted in terms of upper limits on new physics. Upper limits are set at a 95% confidence level (CL) on the pair production cross section of vector-like leptons, $\sigma(pp \to \tau'^{+}\tau'^{-})$.

The limits are calculated using the asymptotic approximation of the CLs method [83, 84], as implemented in the `COMBINE` software tool [85]. The statistical analysis incorporates the binned N_{RecHits} distributions from all signal and control regions, with all systematic uncertainties, as described in Section 5.7, included as constrained nuisance parameters in a maximum likelihood fit.

The results are presented in the following subsections in two ways: first, as a function of the LLP proper decay length ($c\tau_a$) for several benchmark VLL masses, and second, as a function of the VLL mass ($m_{\tau'}$) for various fixed LLP lifetimes. These observed limits are compared to the theoretical production cross section to determine the excluded regions of the model's parameter space.

5.8.1 Limits vs Lifetime

The results of the search are first presented as 95% CL upper limits on the VLL pair production cross section, $\sigma(pp \to \tau'^{+}\tau'^{-})$, as a function of the pseudoscalar boson's proper decay length, $c\tau_a$. These limits are calculated for several benchmark VLL masses.

Figure 5.46 shows the observed and expected limits for a representative VLL mass of 700 GeV and an LLP mass of 2 GeV. The search achieves its highest sensitivity for lifetimes around $c\tau_a \approx 0.1$ m. At this point, the probability of the LLP decaying within the instrumented volume of the muon system is maximized. For shorter lifetimes, the sensitivity decreases as the LLP is more likely to decay before reaching the muon detectors. Conversely, for longer lifetimes, the acceptance is reduced as the LLP tends to decay outside the CMS detector volume entirely.

For this benchmark scenario with $m_{\tau'} = 700$ GeV, the observed (expected) 95% CL upper limit on the cross section at the point of highest sensitivity is 0.12 (0.10) fb. By comparing the observed limit to the theoretically predicted cross section (solid red line), a range of proper decay lengths can be excluded. For this mass point, lifetimes between approximately 0.03 and 0.4 m are excluded at 95% CL.

While the 700 GeV mass point serves as a representative benchmark, the analysis was performed across a wide range of VLL masses, from 200 to 1000 GeV. These additional scenarios show a similar behavior, with the sensitivity peaking at intermediate lifetimes that correspond to decays inside the muon system. For completeness, the full set of exclusion limits as a function of $c\tau_a$ for the other benchmark masses investigated in this work are presented in Appendix A.

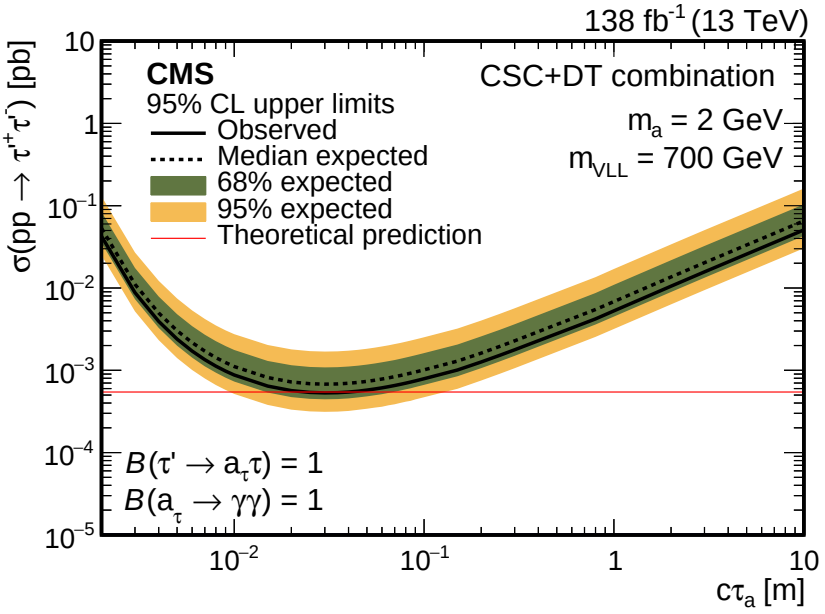

Figure 5.46: The 95% CL observed (solid black line) and expected (dashed black line) upper limits on the VLL production cross section as a function of the LLP proper decay length, for a VLL mass of 700 GeV. The inner (green) and outer (yellow) bands represent the 68% and 95% CL intervals on the expected limit, respectively. The theoretical cross section is shown by the solid red line. Figure from [6].

5.8.2 Limits vs VLL Mass

To explore the sensitivity of the search across the VLL mass range, upper limits are also set as a function of $m_{\tau'}$. This is done for several fixed lifetime hypotheses of the pseudoscalar boson, a_τ. Figure 5.47 shows the 95% CL upper limits for a benchmark lifetime of $c\tau_a = 0.025$ m.

As the VLL mass increases, the theoretical production cross section (red line) decreases steeply due to phase-space suppression. The observed and expected limits also become weaker at higher masses, as fewer signal events are produced. The intersection of the observed limit curve with the theoretical prediction defines the excluded mass range for that specific lifetime. For this scenario, VLL masses below 700 GeV are observed to be excluded at 95% CL, which is consistent with the expected exclusion limit of 670 GeV.

The full exclusion contour in the two-dimensional plane of VLL mass versus LLP lifetime is presented in Figure 5.48. This plot summarizes the overall result of the search, combining the information from all tested benchmark points. The region enclosed by the white contour represents the parameter space excluded by this analysis, setting the most stringent constraints to date on this model.

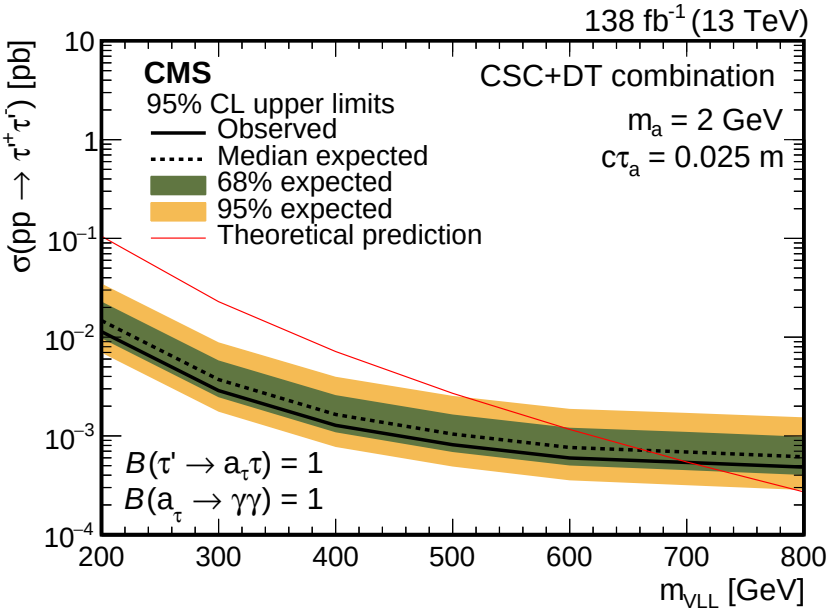

Figure 5.47: The 95% CL observed and expected upper limits on the VLL production cross section as a function of the VLL mass for a fixed LLP proper decay length of $c\tau_a = 0.025$ m. The pseudoscalar boson mass is 2 GeV. The theoretical prediction is shown as a red line. Figure from [6].

5.9 Summary

This chapter presented a novel search for long-lived particles originating from the decay of vector-like leptons decaying into a final state containing at least one hadronically decaying tau lepton and a long-lived pseudoscalar boson, exploiting the unique capabilities of the CMS muon system to detect displaced electromagnetic showers. The analysis was performed using 138 fb^{-1} of proton-proton collision data collected by the CMS experiment at $\sqrt{s} = 13$ TeV. Through the development of dedicated reconstruction algorithms, a robust data-driven background model, and a comprehensive treatment of systematic uncertainties, the analysis sets the first experimental limits on this specific decay topology.

The results exclude significant portions of the model's parameter space, including VLL masses up to 700 GeV at 95% confidence level for proper decay lengths of the LLP near 0.005–2.4 meters. These findings highlight the potential of unconventional reconstruction strategies in extending the discovery reach of the LHC, and pave the way for future LLP searches in the muon system and beyond.

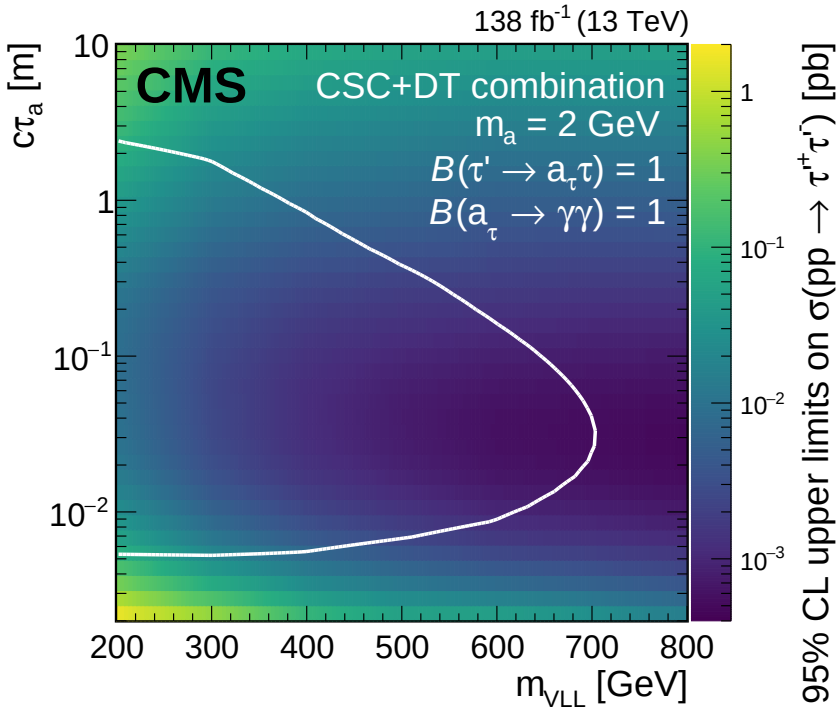

Figure 5.48: The 95% CL observed upper limits on the VLL production cross section in the plane of VLL mass versus the pseudoscalar boson mean proper decay length, $c\tau_a$. The pseudoscalar boson mass is 2 GeV. The area enclosed by the white line corresponds to the excluded region. Figure from [6].

With this search, the thesis culminates in an original experimental contribution to the broader effort of exploring physics beyond the Standard Model through long-lived particles.

A | Supplemental Plots: Limits vs Lifetime

This appendix contains the full set of 95% CL upper limits on the VLL pair production cross section as a function of the LLP proper decay length ($c\tau_a$) for all benchmark VLL mass points studied in this analysis.

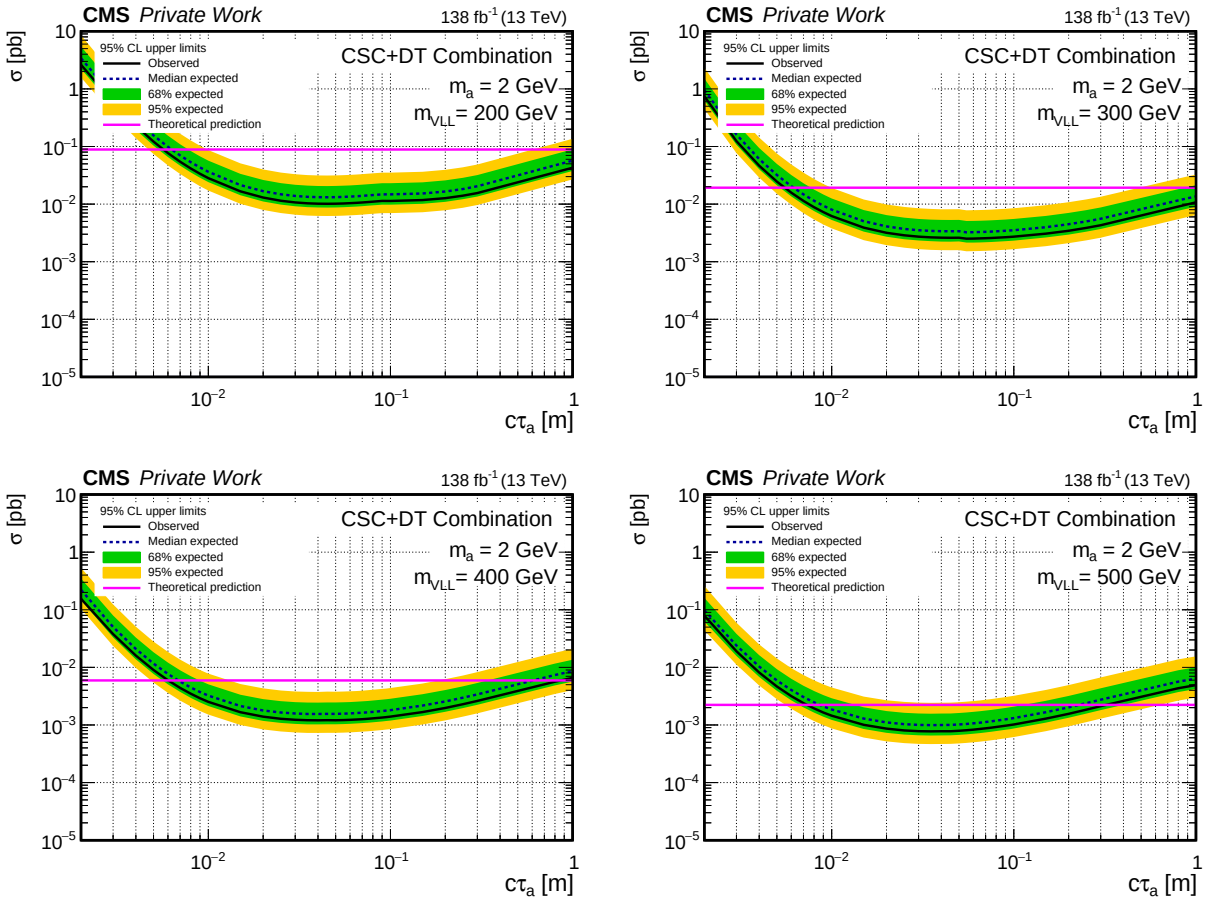

Figure A.1: 95% CL observed and expected upper limits on the VLL production cross section as a function of the LLP $c\tau_a$. The LLP mass is 2 GeV. The VLL mass hypotheses shown are 200, 300, 400, and 500 GeV.

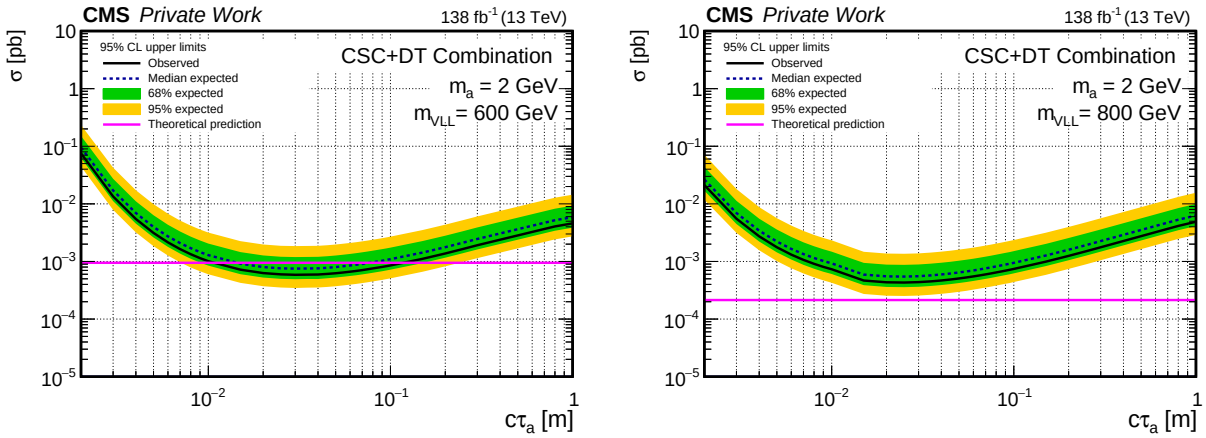

Figure A.2: 95% CL observed and expected upper limits on the VLL production cross section as a function of the LLP $c\tau_a$. The LLP mass is 2 GeV. The VLL mass hypotheses shown are 600 and 800 GeV.

B | Supplemental Plots: Limits vs VLL Mass

This appendix contains the full set of 95% CL upper limits on the VLL production cross section as a function of the LLP $c\tau_a$ for different VLL masses. Figures B.1 and B.2 show the results for LLP masses corresponding to 10 GeV, Figures B.3 and B.4 show the results for LLP masses corresponding to 2 GeV.

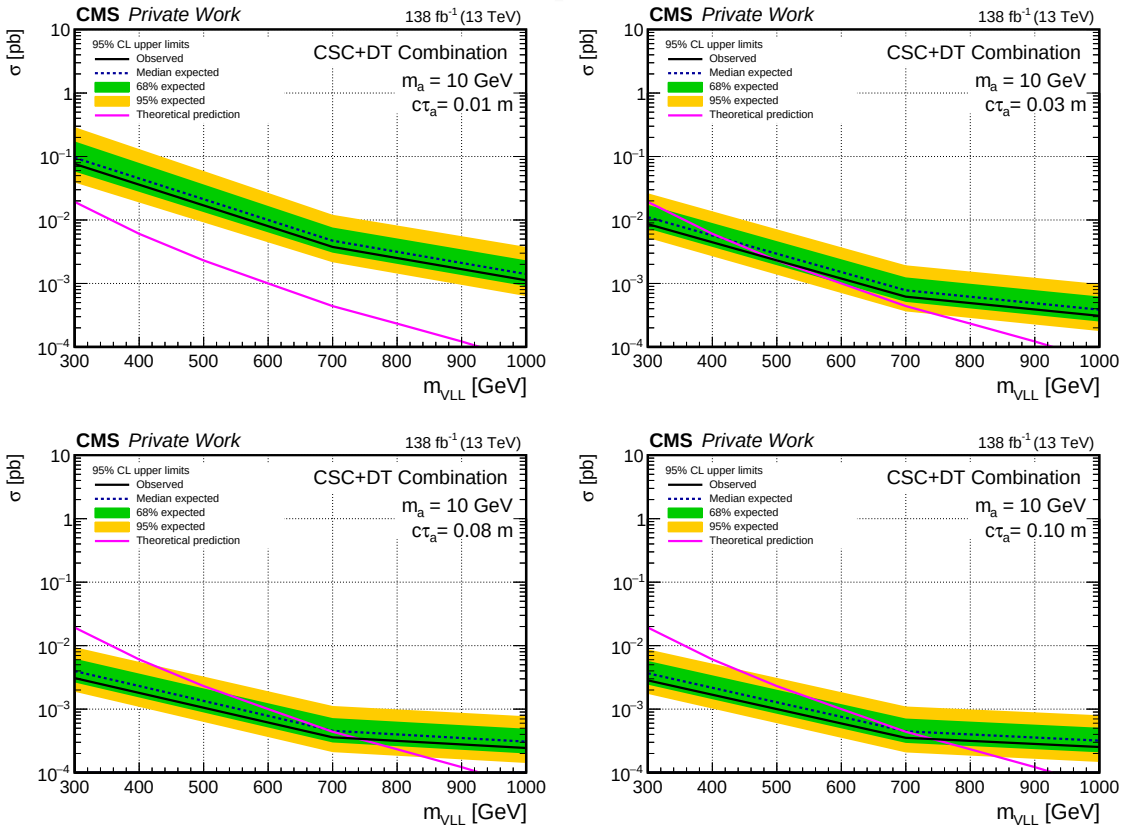

Figure B.1: 95% CL observed and expected upper limit on the production cross section as a function of the VLL mass for different LLP $c\tau_a$ values: 0.01, 0.03, 0.08 and 0.1 meters. The pseudoscalar mass is 10 GeV. The theoretical prediction is shown (pink line).

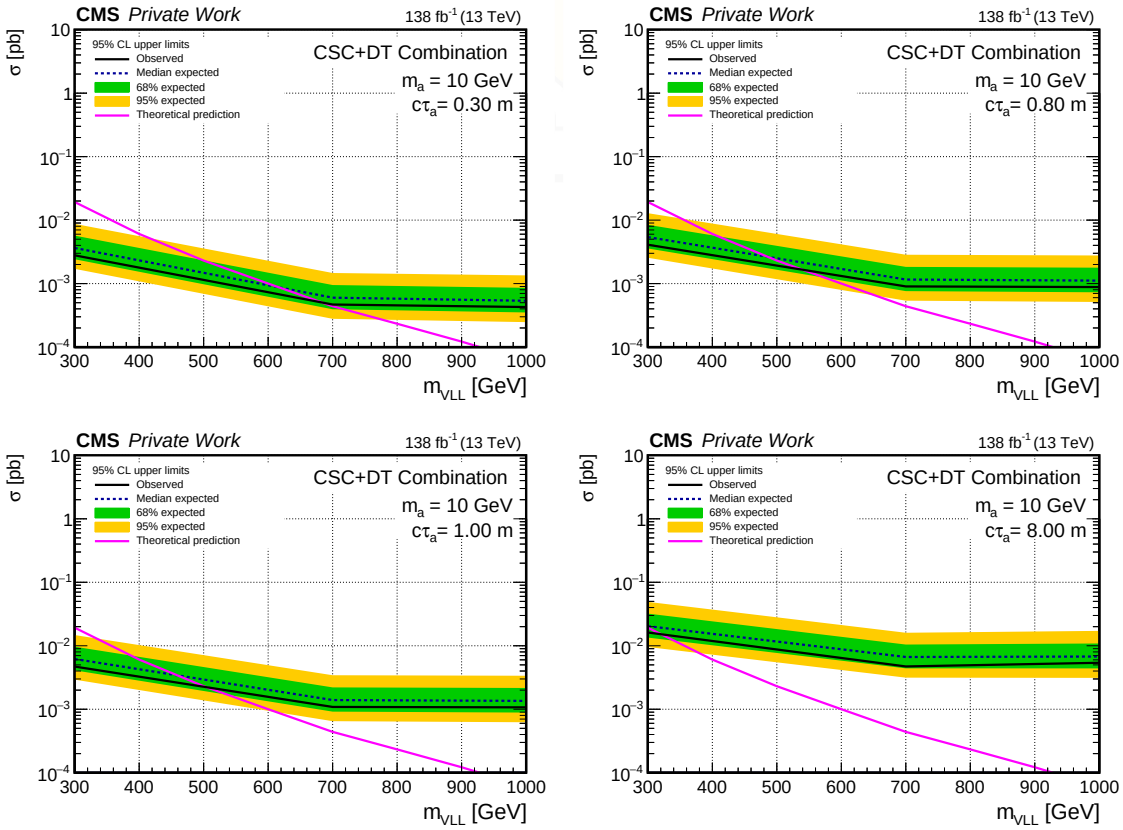

Figure B.2: 95% CL observed and expected upper limit on the production cross section as a function of the VLL mass for different LLP $c\tau_a$ values: 0.3, 0.8, 1 and 8 meters. The pseudoscalar mass is 10 GeV. The theoretical prediction is shown (pink line).

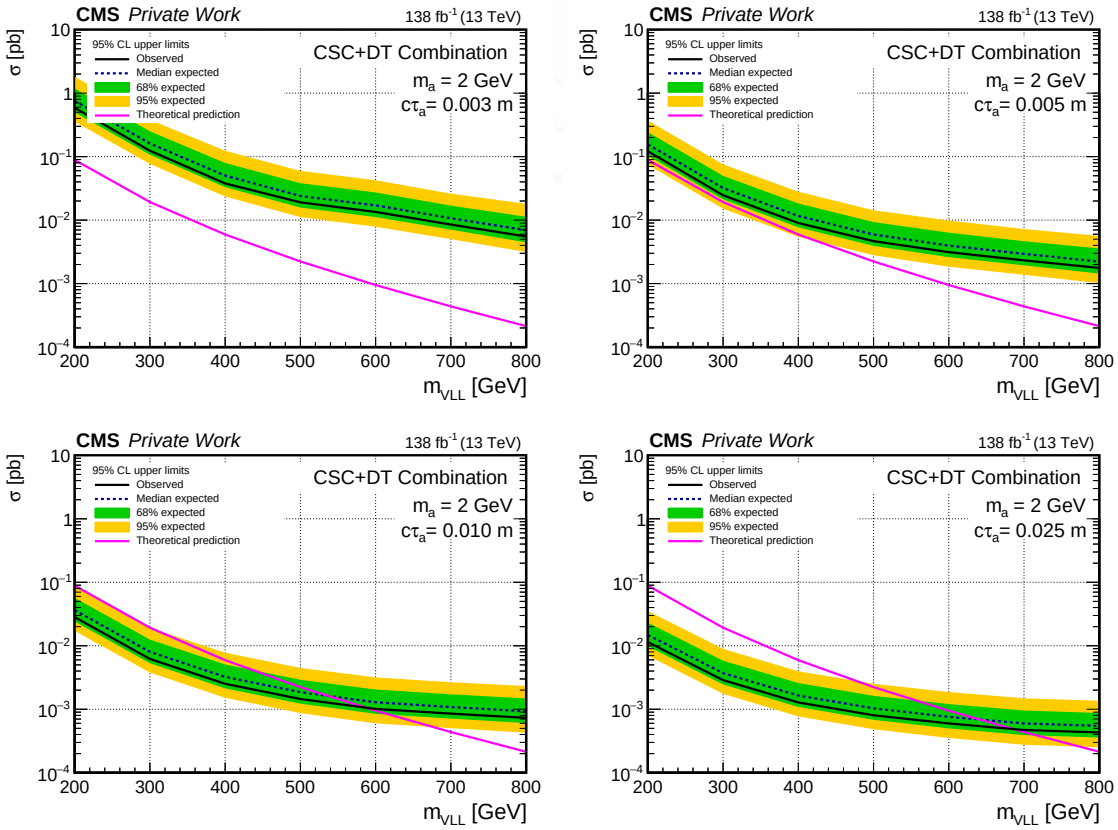

Figure B.3: 95% CL observed and expected upper limit on the production cross section as a function of the VLL mass for different LLP $c\tau_a$ values: 0.003, 0.005, 0.010 and 0.025 meters. The pseudoscalar mass is 2 GeV. The theoretical prediction is shown (pink line).

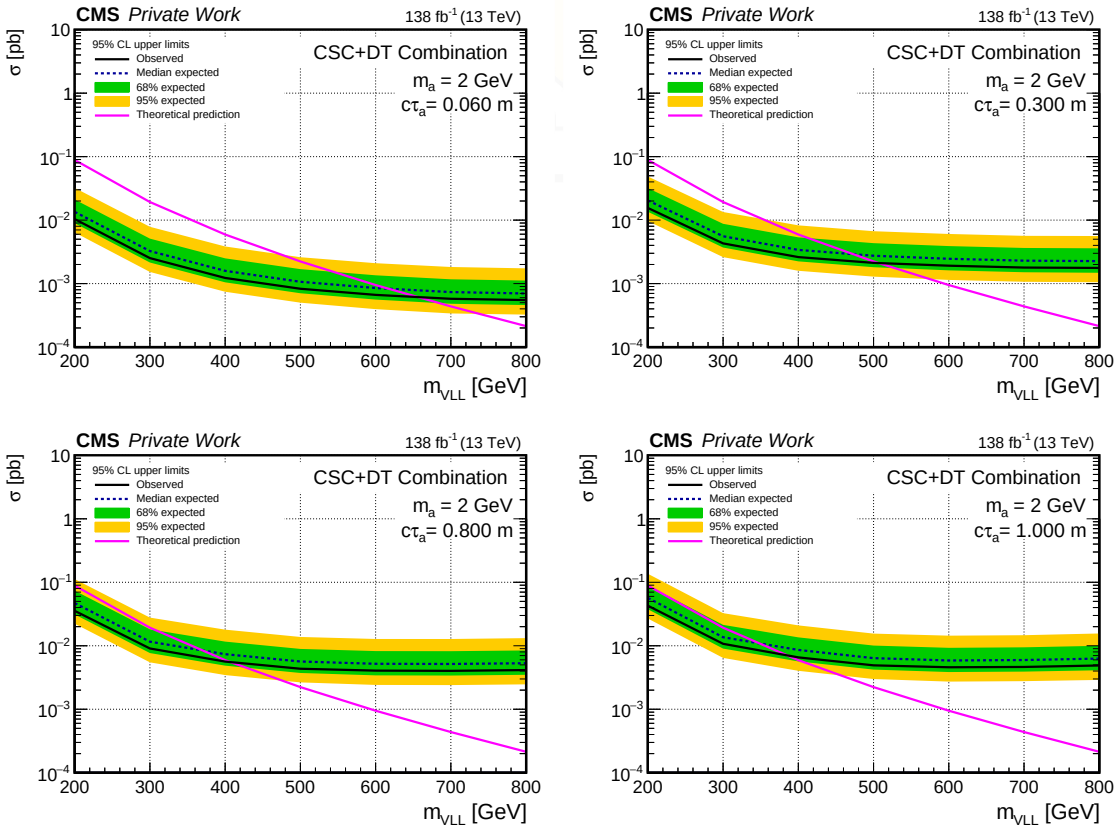

Figure B.4: 95% CL observed and expected upper limit on the production cross section as a function of the VLL mass for different LLP $c\tau_a$ values: 0.060, 0.3, 0.8 and 1 meters. The pseudoscalar mass is 2 GeV. The theoretical prediction is shown (pink line).

Bibliography

[1] A. Collaboration. "Observation of a new particle in the search for the Standard Model Higgs boson with the ATLAS detector at the LHC". In: *Phys. Lett. B* 716 (2012), pp. 1–29. DOI: 10.1016/j.physletb.2012.08.020.

[2] C. Collaboration. "Observation of a new boson at a mass of 125 GeV with the CMS experiment at the LHC". In: *Phys. Lett. B* 716 (2012), pp. 30–61. DOI: 10.1016/j.physletb.2012.08.021.

[3] R. Workman et al. "Review of Particle Physics". In: *Prog. Theor. Exp. Phys.* 2022 (2022), p. 083C01. DOI: 10.1093/ptep/ptac097.

[4] S. Weinberg. "A Model of Leptons". In: *Phys. Rev. Lett.* 19 (1967), pp. 1264–1266. DOI: 10.1103/PhysRevLett.19.1264.

[5] N. Aghanim et al. "Planck 2018 results. VI. Cosmological parameters". In: *Astron. Astrophys.* 641 (2020), A6. DOI: 10.1051/0004-6361/201833910.

[6] C. Collaboration. *Search for vector-like leptons with long-lived particle decays in the CMS muon system in proton-proton collisions at $\sqrt{s}$ = 13 TeV*. Tech. rep. CMS-PAS-EXO-23-015. CERN, 2025. URL: https://cds.cern.ch/record/2880100.

[7] C. Collaboration. "Search for long-lived particles decaying in the CMS endcap muon detectors in proton-proton collisions at $\sqrt{s}$ =13 TeV". In: *Phys. Rev. Lett.* 127.26 (2021), p. 261804. DOI: 10.1103/PhysRevLett.127.261804.

[8] C. Collaboration. "Search for long-lived particles decaying in the CMS muon detectors in proton-proton collisions at $\sqrt{s}$ = 13 TeV". In: *arXiv preprint* (2024).

[9] Wikipedia contributors. *Standard Model — Wikipedia, The Free Encyclopedia*. https://en.wikipedia.org/wiki/Standard_Model. Accessed: 2025-06-06. 2024.

[10] G. Arnison et al. "Experimental Observation of Isolated Large Transverse Energy Electrons with Associated Missing Energy at $\sqrt{s}$ = 540 GeV". In: *Phys. Lett. B* 122 (1983), pp. 103–116. DOI: 10.1016/0370-2693(83)91177-2.

[11] G. Arnison et al. "Experimental Observation of Lepton Pairs of Invariant Mass Around 95 GeV/c^2 at the CERN SPS Collider". In: *Phys. Lett. B* 126 (1983), pp. 398–410. DOI: 10.1016/0370-2693(83)90188-0.

[12] C. Collaboration. "Observation of top quark production in $\bar{p}p$ collisions with the Collider Detector at Fermilab". In: *Phys. Rev. Lett.* 74 (1995), pp. 2626–2631. DOI: 10.1103/PhysRevLett.74.2626.

[13] D. Collaboration. "Observation of the top quark". In: *Phys. Rev. Lett.* 74 (1995), pp. 2632–2637. DOI: 10.1103/PhysRevLett.74.2632.

[14] K. Kodama et al. "Observation of tau neutrino interactions". In: *Phys. Lett. B* 504 (2001), pp. 218–224. DOI: 10.1016/S0370-2693(01)00337-2.

[15] F. Englert et al. "Broken Symmetry and the Mass of Gauge Vector Mesons". In: *Phys. Rev. Lett.* 13 (1964), pp. 321–323. DOI: 10.1103/PhysRevLett.13.321.

[16] P. W. Higgs. "Broken Symmetries and the Masses of Gauge Bosons". In: *Phys. Rev. Lett.* 13 (1964), pp. 508–509. DOI: 10.1103/PhysRevLett.13.508.

[17] G. S. Guralnik et al. "Global Conservation Laws and Massless Particles". In: *Phys. Rev. Lett.* 13 (1964), pp. 585–587. DOI: 10.1103/PhysRevLett.13.585.

[18] J. Riebesell. *Higgs potential*. https://tikz.net/higgs-potential/. Accessed: 2024-02-04.

[19] Y. F. et al. (Super-Kamiokande Collaboration). “Evidence for Oscillation of Atmospheric Neutrinos”. In: *Phys. Rev. Lett.* 81 (1998), pp. 1562–1567. DOI: 10.1103/PhysRevLett.81.1562.

[20] V. C. Rubin et al. “Rotation of the Andromeda Nebula from a Spectroscopic Survey of Emission Regions”. In: *Astrophys. J.* 159 (1970), p. 379. DOI: 10.1086/150317.

[21] D. Clowe et al. “A Direct Empirical Proof of the Existence of Dark Matter”. In: *Astrophys. J. Lett.* 648 (2006), pp. L109–L113. DOI: 10.1086/508162.

[22] L. Canetti et al. “Matter and Antimatter in the Universe”. In: *New J. Phys.* 14 (2012), p. 095012. DOI: 10.1088/1367-2630/14/9/095012.

[23] S. Weinberg. “Baryon and Lepton Nonconserving Processes”. In: *Phys. Rev. Lett.* 43 (1979), pp. 1566–1570. DOI: 10.1103/PhysRevLett.43.1566.

[24] G. ’t Hooft. “Naturalness, Chiral Symmetry, and Spontaneous Chiral Symmetry Breaking”. In: *NATO Sci. Ser. B* 59 (1980), pp. 135–157.

[25] R. D. Peccei et al. “CP Conservation in the Presence of Instantons”. In: *Phys. Rev. Lett.* 38 (1977), pp. 1440–1443. DOI: 10.1103/PhysRevLett.38.1440.

[26] The CMS Collaboration. “Review of searches for vector-like quarks, vector-like leptons, and heavy neutral leptons in proton-proton collisions at $\sqrt{s} = 13$ TeV at the CMS experiment”. In: *Phys. Rept.* 1115 (2025). arXiv:2402.09342, pp. 570–677. DOI: 10.1016/j.physrep.2024.09.012.

[27] M. J. Strassler et al. “Echoes of a Hidden Valley at Hadron Colliders”. In: *Phys. Lett. B* 651 (2007), pp. 374–379. DOI: 10.1016/j.physletb.2007.06.055.

[28] H. K. Dreiner. “An Introduction to explicit R-parity violation”. In: (1998). Ed. by G. L. Kane, pp. 462–479.

[29] R. Barbier et al. “R-parity violating supersymmetry”. In: *Phys. Rept.* 420 (2005), pp. 1–202. DOI: 10.1016/j.physrep.2005.08.006.

[30] Z. Chacko et al. “The Twin Higgs: Natural electroweak breaking from mirror symmetry”. In: *Phys. Rev. Lett.* 96 (2006), p. 231802. DOI: 10.1103/PhysRevLett.96.231802.

[31] N. Craig et al. “Folded Supersymmetry”. In: *JHEP* 03 (2016), p. 106. DOI: 10.1007/JHEP03(2016)106.

[32] D. Curtin et al. “Exotic Decays of the 125 GeV Higgs Boson”. In: *Phys. Rev. D* 90.7 (2014), p. 075004. DOI: 10.1103/PhysRevD.90.075004.

[33] C. Collaboration. “Review of searches for vector-like quarks, vector-like leptons, and heavy neutral leptons in proton–proton collisions at $\sqrt{s} = 13$ TeV”. In: (2024).

[34] G. Aad et al. “Search for vector-like quarks in events with one lepton, jets, and missing transverse momentum in *pp* collisions at $\sqrt{s} = 13$ TeV with the ATLAS detector”. In: *Phys. Rev. D* 106.5 (2022), p. 052009. DOI: 10.1103/PhysRevD.106.052009.

[35] C. F. S. Cid. “Probing dark matter freeze-in with long-lived particle signatures: MATHUSLA, HL-LHC and FCC-hh”. In: *J. Phys. Conf. Ser.* 1586 (2020), p. 012028. DOI: 10.1088/1742-6596/1586/1/012028.

[36] I. Neutelings. *TikZ example: Signatures of long-lived particles*. https://tikz.net/bsm_longlived/. Accessed: 2025-06-08. 2023.

[37] L. Evans et al. “LHC Machine”. In: *JINST* 3 (2008), S08001. DOI: 10.1088/1748-0221/3/08/S08001.

[38] CMS Collaboration. “Precision luminosity measurement in proton-proton collisions at $\sqrt{s} = 13$ TeV in 2015 and 2016 at CMS”. In: *Eur. Phys. J. C* 81.9 (2021), p. 800. DOI: 10.1140/epjc/s10052-021-09538-2.

[39] E. Lopienska. *The CERN accelerator complex, layout in 2022. Complexe des accélérateurs du CERN en janvier 2022*. https://cds.cern.ch/record/2800984. General Photo, CERN Document Server. Accessed: 2024-05-18. 2022.

[40] C. Collaboration. *CMS Detector Cutaway View*. Retrieved from CDS. 2022. URL: https://cds.cern.ch/record/2665537.

[41] C. Collaboration. *CMS coordinate system diagram*. https://cds.cern.ch/record/1120627. CMS Public Document, CMS-INTERNAL-2008-004. 2008.

[42] V. I. K. et al. “Measurement of the CMS magnetic field”. In: *IEEE Trans. Appl. Supercond.* 18.2 (2008), pp. 395–398. DOI: 10.1109/TASC.2008.921242.

[43] C. Collaboration. *Sketches of the CMS Tracker Detector*. 2022. URL: https://twiki.cern.ch/twiki/bin/view/CMSPublic/DPGResultsTRK.

[44] C. Collaboration. "Description and performance of track and primary-vertex reconstruction with the CMS tracker". In: *JINST* 9 (2014), P10009. DOI: 10.1088/1748-0221/9/10/P10009.

[45] C. Collaboration. "The CMS electromagnetic calorimeter project: Technical Design Report". In: *CERN-LHCC-97-033* (1997). URL: https://cds.cern.ch/record/349375.

[46] C. Collaboration. "An overview of more than ten years of operation of the CMS ECAL". In: *International Journal of Modern Physics A* (2025). Figure 9. URL: https://www.researchgate.net/figure/Relative-electron-ECAL-energy-resolution-plotted-for-CMS-data-recorded-during-LHC-Run-2_fig9_385679248.

[47] C. Collaboration. "The CMS hadron calorimeter project: Technical Design Report". In: *CERN-LHCC-96-038* (1997). URL: https://cds.cern.ch/record/343829.

[48] C. Collaboration. "Calibration of the CMS hadron calorimeters using proton-proton collision data at $\sqrt{s}$ = 13 TeV". In: *JINST* 15 (2020). Figure 1, P05002. URL: https://www.researchgate.net/figure/A-schematic-view-of-one-quarter-of-the-CMS-HCAL-during-2016-LHC-operation-showing-the_fig1_336208095.

[49] C. Collaboration. "The performance of the CMS muon detector in proton-proton collisions at $\sqrt{s} = 7$ TeV at the LHC". In: *JINST* 8 (2013), P11002. DOI: 10.1088/1748-0221/8/11/P11002. URL: https://www.semanticscholar.org/paper/The-performance-of-the-CMS-muon-detector-in-at-%3D-7-Collaboration/e2d414103fa586c17cdd83eaa7175e00897c0700.

[50] C. Collaboration. "Performance of the CMS Level-1 trigger in proton-proton collisions at $\sqrt{s} = 13$ TeV". In: *JINST* 15 (2020), P10017. DOI: 10.1088/1748-0221/15/10/P10017.

[51] G. B. et al. "The data-acquisition system of the CMS experiment at the LHC". In: *J. Phys. Conf. Ser.* 331 (2011), p. 022021. DOI: 10.1088/1742-6596/331/2/022021.

[52] C. Collaboration. "Search for long-lived particles decaying in the CMS muon detectors in proton-proton collisions at $\sqrt{s} = 13$ TeV". In: *Phys. Rev. D* 110 (2024), p. 032007. DOI: 10.1103/PhysRevD.110.032007.

[53] C. Collaboration. "Particle-flow reconstruction and global event description with the CMS detector". In: *JINST* 12 (2017), P10003. DOI: 10.1088/1748-0221/12/10/P10003.

[54] CMS Collaboration. *NANOAOD: a new data format for the analysis of the large datasets of Run 2*. Tech. rep. CERN, 2020. URL: https://cds.cern.ch/record/2711311.

[55] M. Cacciari et al. "The anti-k_T jet clustering algorithm". In: *JHEP* 04 (2008), p. 063. DOI: 10.1088/1126-6708/2008/04/063.

[56] C. Collaboration. "Identification of hadronic tau lepton decays using a deep neural network". In: *JINST* 17 (2022), P07023. DOI: 10.1088/1748-0221/17/07/P07023.

[57] CMS Collaboration. "Search for vector-like leptons with long-lived particle decays in the CMS muon system in proton-proton collisions at $\sqrt{s} = 13$ TeV". In: *arXiv preprint arXiv:2503.16699* (2025). URL: https://arxiv.org/abs/2503.16699.

[58] E. Bernreuther et al. "Vectorlike leptons and long-lived bosons at the LHC". In: *arXiv preprint arXiv:2304.08509* (2023). URL: https://arxiv.org/abs/2304.08509.

[59] A. Alloul et al. "FeynRules 2.0 - A complete toolbox for tree-level phenomenology". In: *Comput. Phys. Commun.* 185 (2014), pp. 2250–2300. DOI: 10.1016/j.cpc.2014.04.012.

[60] J. Alwall et al. "The automated computation of tree-level and next-to-leading order differential cross sections, and their matching to parton shower simulations". In: *JHEP* 07 (2014), p. 079. DOI: 10.1007/JHEP07(2014)079.

[61] T. Sjöstrand et al. "An Introduction to PYTHIA 8.2". In: *Comput. Phys. Commun.* 191 (2015), pp. 159–177. DOI: 10.1016/j.cpc.2015.01.024.

[62] "Event generator tunes obtained from underlying event and multiparton scattering measurements". In: *Eur. Phys. J. C* 76.3 (2016), p. 155. DOI: 10.1140/epjc/s10052-016-3988-x.

[63] S. Agostinelli et al. "GEANT4–a simulation toolkit". In: *Nucl. Instrum. Meth. A* 506 (2003), pp. 250–303. DOI: 10.1016/S0168-9002(03)01368-8.

[64] "Description and performance of track and primary-vertex reconstruction with the CMS tracker". In: *JINST* 9 (2014), P10009. DOI: 10.1088/1748-0221/9/10/P10009.

[65] M. Ester et al. "A Density-Based Algorithm for Discovering Clusters in Large Spatial Databases with Noise". In: *Proc. 2nd Int. Conf. on Knowledge Discovery and Data Mining*. 1996, pp. 226–231.

[66] C. Collaboration. *Search for long-lived particles from vector-like leptons using muon detector showers*. Tech. rep. AN-23-011. Internal analysis note. CMS, 2023.

[67] C. Collaboration. *Extended studies of LLP clustering and efficiency in the muon system*. Tech. rep. AN-23-026. CERN, 2023.

[68] "Performance of CMS muon reconstruction in pp collision events at $\sqrt{s} = 13$ TeV". In: *JINST* 13 (2018), P06015. DOI: 10.1088/1748-0221/13/06/P06015.

[69] C. Collaboration. "Particle-Flow Event Reconstruction in CMS and Performance for Jets, Taus, and MET". In: (2009). CMS Physics Analysis Summary. URL: https://cds.cern.ch/record/1194487.

[70] "The anti-k(t) jet clustering algorithm". In: *JHEP* 04 (2008), p. 063. DOI: 10.1088/1126-6708/2008/04/063.

[71] C. Collaboration. "JetMET JERC recommendations for UL17 and UL18". In: (2020). CMS Detector Performance Summary. URL: https://cds.cern.ch/record/2747736.

[72] C. Collaboration. *Search for Long-Lived Particles Decaying in the Muon System with 13 TeV Data*. CMS Analysis Note CMS-AN-2023/011. CERN, 2023. URL: https://cms-docdb.cern.ch/cgi-bin/PublicDocDB/RetrieveFile?docid=17698&filename=AN-23-011_v9.pdf&version=9.

[73] C. Collaboration. "Performance of reconstruction and identification of τ leptons decaying to hadrons and ν_τ in pp collisions at $\sqrt{s} = 13$ TeV". In: *JINST* 13 (2018), P10005. DOI: 10.1088/1748-0221/13/10/P10005.

[74] CMS Collaboration. "Performance of reconstruction and identification of τ leptons decaying to hadrons and ν_τ in pp collisions at $\sqrt{s} = 13$ TeV". In: *JINST* 13.10 (2018), P10005. DOI: 10.1088/1748-0221/13/10/P10005.

[75] "Performance of missing transverse momentum reconstruction in proton-proton collisions at $\sqrt{s} = 13$ TeV using the CMS detector". In: *JINST* 14 (2019), P07004. DOI: 10.1088/1748-0221/14/07/P07004.

[76] CMS JETMET POG. *MET Recommendations for UL datasets*. https://twiki.cern.ch/twiki/bin/view/CMS/MissingETRun2CorrectionsUL. Accessed: 2025-05. 2022.

[77] CMS JETMET POG. *2017 EE noise mitigation and MET uncertainties*. https://twiki.cern.ch/twiki/bin/viewauth/CMS/MissingETOptionalFiltersRun2. Accessed: 2025-05.

[78] CMS JETMET POG. *MET Filters Recommendation for 2016-2018*. https://twiki.cern.ch/twiki/bin/viewauth/CMS/MissingETOptionalFiltersRun2. Accessed: 2025-05.

[79] CMS Collaboration. *Checklist for CMS EXO Pre-approvals*. Tech. rep. Available at: https://cms-docdb.cern.ch/cgi-bin/PublicDocDB/RetrieveFile?docid=6442&filename=EXO_PreApproval_Checklist.pdf. CERN, 2021.

[80] CMS Collaboration. *Search for LLPs using muon system-only observables*. Tech. rep. Internal Analysis Note. CMS AN-21-056, 2021.

[81] C. Collaboration. *Search for long-lived particles decaying in the muon system using CMS Run-2 data*. Tech. rep. CMS-AN-2021/124. Internal Analysis Note. CERN, 2021.

[82] CMS Collaboration. "Jet energy scale and resolution in the CMS experiment in pp collisions at 8 TeV". In: *JINST* 12.02 (2017), P02014. DOI: 10.1088/1748-0221/12/02/P02014.

[83] T. R. Junk. "Confidence level computation for combining searches with small statistics". In: *Nucl. Instrum. Meth. A* 434 (1999), pp. 435–443. DOI: 10.1016/S0168-9002(99)00498-2.

[84] A. L. Read. "Presentation of search results: The CLs technique". In: *J. Phys. G* 28 (2002), pp. 2693–2704. DOI: 10.1088/0954-3899/28/10/313.

[85] CMS Collaboration. *The CMS statistical analysis and combination tool: combine*. https://cms-analysis.github.io/HiggsAnalysis-CombinedLimit/. 2021.